Time-resolved ARPES studies of quantum materials

Fabio Boschini[*]

Institut National de la Recherche Scientifique—Énergie Matériaux Télécommunications,
Varennes, Quebec J3X 1S2, Canada
and Quantum Matter Institute, University of British Columbia,
Vancouver, British Columbia V6T 1Z4, Canada

Marta Zonno[†]

Quantum Matter Institute, University of British Columbia,
Vancouver, British Columbia V6T 1Z4, Canada
and Canadian Light Source, Saskatoon, Saskatchewan S7N 2V3, Canada

Andrea Damascelli[‡]

Quantum Matter Institute, University of British Columbia,
Vancouver, British Columbia V6T 1Z4, Canada
and Department of Physics and Astronomy, University of British Columbia,
Vancouver, British Columbia V6T 1Z1, Canada

(published 27 February 2024)

Angle-resolved photoemission spectroscopy (ARPES), with its exceptional sensitivity to both the binding energy and the momentum of valence electrons in solids, provides unparalleled insight into the electronic structure of quantum materials. Over the past two decades, the advent of femtosecond lasers, which can deliver ultrashort and coherent light pulses, has ushered the ARPES technique into the time domain. Currently time-resolved ARPES (TR-ARPES) can probe ultrafast electron dynamics and the out-of-equilibrium electronic structure, providing a wealth of information that is otherwise unattainable in conventional ARPES experiments. This review begins with an introduction to the theoretical underpinnings of TR-ARPES followed by a description of recent advances in state-of-the-art ultrafast sources and optical excitation schemes. It then reviews paradigmatic phenomena investigated by TR-ARPES thus far, such as out-of-equilibrium electronic states and their spin dynamics, Floquet-Volkov states, photoinduced phase transitions, electron-phonon coupling, and surface photovoltage effects. Each section highlights TR-ARPES data from diverse classes of quantum materials, including semiconductors, charge-ordered systems, topological materials, excitonic insulators, Van der Waals materials, and unconventional superconductors. These examples demonstrate how TR-ARPES has played a critical role in unraveling the complex dynamical properties of quantum materials. The conclusion outlines possible future directions and opportunities.

CONTENTS

[*]fabio.boschini@inrs.ca
[†]marta.zonno@lightsource.ca
[‡]damascelli@physics.ubc.ca

I. INTRODUCTION

The physics of quantum materials [solids whose macroscopic properties directly manifest quantum mechanical effects (Keimer and Moore, 2017)] lies at the heart of current condensed matter research and holds the potential to revolutionize many aspects of everyday life, encompassing energy, transportation, medical, and advanced technology applications. In many quantum materials, interactions among electrons themselves or with other degrees of freedom (for example, orbital, spin, charge, and lattice) give rise to various collective excitations. These interactions lead to a number of exotic phenomena, such as high-temperature superconductivity or symmetry-protected topological states. Understanding how electron interactions result in the emergence of novel quantum phases of matter is a central question in the field. Among the experimental techniques sensitive to fermionic quasiparticles, angle-resolved photoemission spectroscopy (ARPES) stands out due to its powerful capability to resolve the one-particle spectral function, which to a first approximation maps the electronic band structure with momentum resolution over the entire 3D Brillouin zone (BZ). Relying on the photoelectric effect, ARPES is a mature photon-in electron-out technique, employing both tabletop light sources and synchrotron facilities, that has been successfully applied to the study of a wide variety of quantum materials over the past few decades and has been extensively reviewed; see Damascelli, Hussain, and Shen (2003), Damascelli (2004), Lu *et al.* (2012), Gedik and Vishik (2017), Lv, Qian, and Ding (2019), Sobota, He, and Shen (2021), and Zhang, Pincelli *et al.* (2022). In recent years, ARPES has been adapted in different directions to tackle the specific needs of various fast-growing domains within quantum materials research, including achieving increasingly better spatial resolution (micro- or nano-ARPES), imaging of spin degree of freedom (spin-ARPES), and characterizing the out-of-equilibrium regime [time-resolved ARPES (TR-ARPES)].

In particular, by extending ARPES into the time domain, time- and angle-resolved photoemission spectroscopy not only provides access to materials' dynamical properties but also facilitates identification of energetically entangled interactions directly in momentum space. A series of technological advancements (optimization of laser systems based on harmonic generation in nonlinear crystals, high-harmonic generation, and improvements in 2D and 3D electron detectors) have enabled TR-ARPES to rapidly mature into a powerful technique. The concurrent discovery of new classes of materials that have particularly benefited from the study of

TR-ARPES (such as topological insulators and two-dimensional transition-metal dichalcogenides) have also played an important role in affirming TR-ARPES as a key experimental technique for unraveling the complex dynamical properties of quantum materials, ranging from high-temperature superconductors to excitonic insulators; see Fig. 1.

TR-ARPES is now maturing in a manner similar to the way that ARPES has flourished over the past three decades. By building upon and expanding on previous reviews on the topic (Smallwood *et al.*, 2016; Sobota, He, and Shen, 2021; Huang, Duan, and Zhang, 2022), this review explains the foundations for the forthcoming development of the TR-ARPES technique by offering a panoramic view of how TR-ARPES has played a crucial role in advancing our knowledge of quantum materials via a detailed discussion of several paradigmatic examples. To this end, the different sections are organized by scientific questions and needs rather than by material, so discussion of TR-ARPES research into specific materials is often spread across different sections. Section II introduces the TR-ARPES technique, summarizes the physics principles on which it is based, describes the information encoded in the transient photoemission signal, covers the main technical aspects of state-of-the-art TR-ARPES systems around the world, and discusses the physical properties, phenomena, and scientific questions that TR-ARPES measures and addresses. Section III discusses the mapping of unoccupied and/or transient states in semiconductors and topological insulators. Section IV reviews photoinduced phase transitions in charge-ordered systems, Mott insulators, excitonic insulators, and high-temperature superconductors. Section V discusses how TR-ARPES can qualitatively or quantitatively evaluate the electron-phonon interaction. Section VI highlights how TR-ARPES can directly assess the emergence of the surface photovoltage phenomenon in semiconductors and topological insulators. Section VII illustrates a few paradigmatic examples of how spin-resolved and/or dichroic TR-ARPES can explore light-induced evolution of the spin degree of freedom in ferromagnets and topologically protected materials. Finally, Sec. VIII offers some concluding remarks and outlines future opportunities to apply TR-ARPES to further expand our knowledge of quantum materials.

II. TIME- AND ANGLE-RESOLVED PHOTOEMISSION

TR-ARPES offers unique access to the electronic dynamics and interactions on sub-picosecond timescales with both time and momentum resolution (Smallwood, Kaindl, and Lanzara, 2016; Sobota, He, and Shen, 2021; Huang, Duan, and Zhang, 2022). Like other time-resolved techniques, TR-ARPES takes advantage of the so-called pump-probe approach (Giannetti *et al.*, 2016). As illustrated in Fig. 2(a), two ultrafast laser pulses are directed onto the sample, separated in time by a tunable delay: the intense pump pulse (commonly in the visible-to-infrared spectral range) excites the system into an out-of-equilibrium condition, whereas the ultraviolet [(UV), ~6 eV] or extreme ultraviolet [(XUV), >10 eV] probe pulse elicits the material to emit photoelectrons. The detector captures these photoelectrons with angular resolution, allowing us to visualize the transient evolution or modification of the electronic band structure and its occupation. By varying the pump-probe delay, TR-ARPES can effectively record the
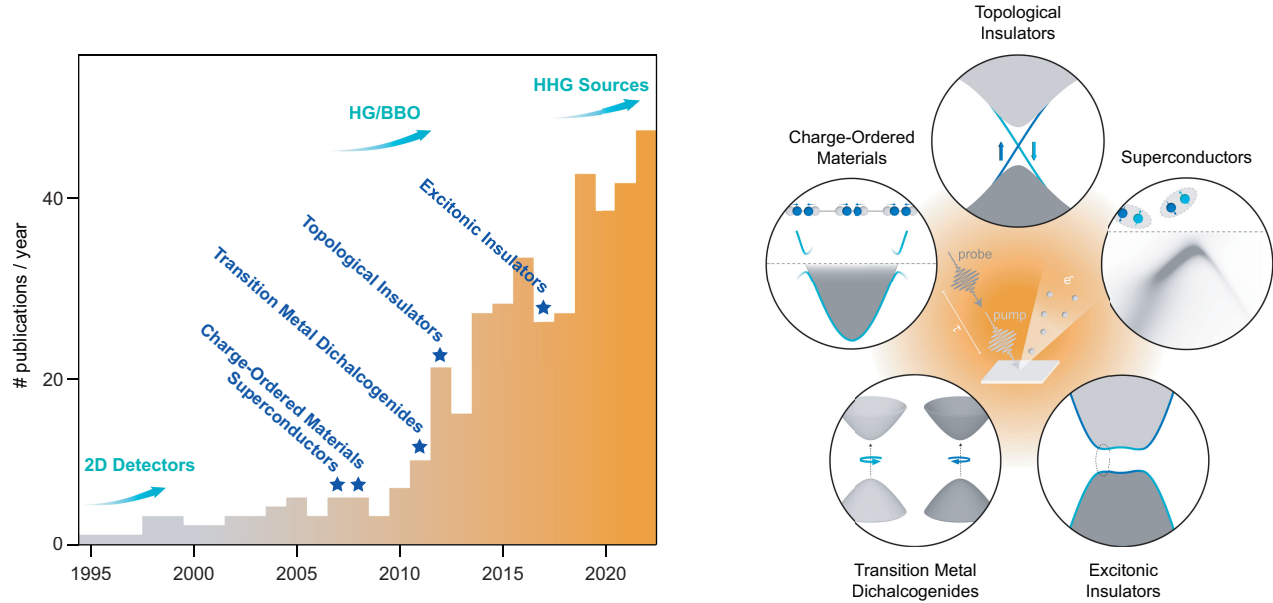
FIG. 1.   The rapid adoption of time- and angle-resolved photoemission spectroscopy. Left panel: increase of the approximate number of annual TR-ARPES publications over the past three decades. Exponential technological progress (milestone advancements in cyan arrows) and interest in new materials (blue stars marking the initial TR-ARPES publications for various classes of materials) have fueled the growth of the TR-ARPES technique over the past two decades. Right illustration: key classes of quantum materials extensively studied via TR-ARPES.

light-induced ultrafast electron dynamics of the system under study.

A simplified and idealized introduction to the principles of the TR-ARPES technique is given in Fig. 2(b), where an n-doped (i.e., electron-doped) Dirac-like dispersion centered at $\mathbf{k} = 0$ momentum provides a simple illustrative example that resembles the dispersion of the surface state of a 3D topological insulator. The top row displays the TR-ARPES energy-momentum maps for four different characteristic pump-probe delays (τ). Negative time delays ($\tau < 0$, far left panel) correspond to the scenario in which the pump pulse reaches the sample after the probe pulse, so the excitation effect does not appear in the photoemission signal [unless events lasting longer than the separation of two consecutive pump pulses, for example, local heating of the sample, or related to the generation of electric fields at the sample's surface, such as surface photovoltage (discussed in Sec. VI), are present]. When the pump and probe pulses overlap ($\tau \sim 0$, center left panel), the TR-ARPES map shows a new electronic distribution determined by the availability of vertical optical transitions driven by the pump excitation, i.e., the optical joint density of states (assuming that the pump pulse does not modify the underlying electronic band structure). Next, on timescales comparable to the electron-electron scattering time ($\tau \sim \tau_{ee} \sim 10$–$100$ fs center right panel), pump-induced hot electrons tend to thermalize into a quasiequilibrium Fermi-Dirac distribution characterized by an effective electronic temperature. Finally, for longer positive delays ($\tau \gg 0$, ~ 100 fs–10 ps, far right panel), the system returns back to its equilibrium conditions by transferring energy from the electronic bath into lattice vibrations and/or other collective modes.

The bottom row of Fig. 2(b) presents differential TR-ARPES maps, computed as $I(\mathbf{k}, \omega)_\tau - I(\mathbf{k}, \omega)_{\tau < 0}$ [where

$I(\mathbf{k}, \omega)_\tau$ represents the photoemission intensity at momentum $\mathbf{k}$, energy ω, and pump-probe delay τ], for the same positive time delays as in the top row. The color red (blue) represents an increase (decrease) of photoemission intensity with respect to the equilibrium counterpart, and thus is commonly referred to as population (depletion). In the early days of TR-ARPES, differential maps were extensively employed to highlight the pump-induced transfer of spectral weight within the band structure. However, this straightforward interpretation may be challenged by several concurrent transient contributions to the photoemission intensity, as later discussed.

Before moving into a more detailed description of the technique and the science attainable with it, we emphasize that this review focuses mainly on TR-ARPES, defined as a technique in which the photoemission process is elicited by the probe pulse, and it is not assisted by the pump pulse. In most cases, the pump pulse drives collective excitations and/or promotes electrons into unoccupied states. In the latter case, once the photoexcited electron thermalizes and undergoes decoherence scattering processes, its subsequent photoemission by the probe pulse can be treated as a *single-photon* process. In this regard, note that a related approach such as two-photon photoemission spectroscopy (2PPE), in which two photons are needed to overcome the material's work function, represents a powerful alternative for exploring the electron dynamics of metals and semiconductors (Damascelli *et al.*, 1996; Bartoli *et al.*, 1997; Hofer *et al.*, 1997; Petek and Ogawa, 1997; Ferrini *et al.*, 1999; Petek *et al.*, 2000; Cui *et al.*, 2014), as well as for mapping unoccupied states (Hao *et al.*, 2010; Sobota *et al.*, 2013; S.-L. Yang *et al.*, 2017). In some cases, TR-ARPES and 2PPE may be indistinguishable. However, this review does not discuss two-photon processes where the first photon excites an electron into a virtual state (i.e., with zero lifetime) or the phase of the intermediate state
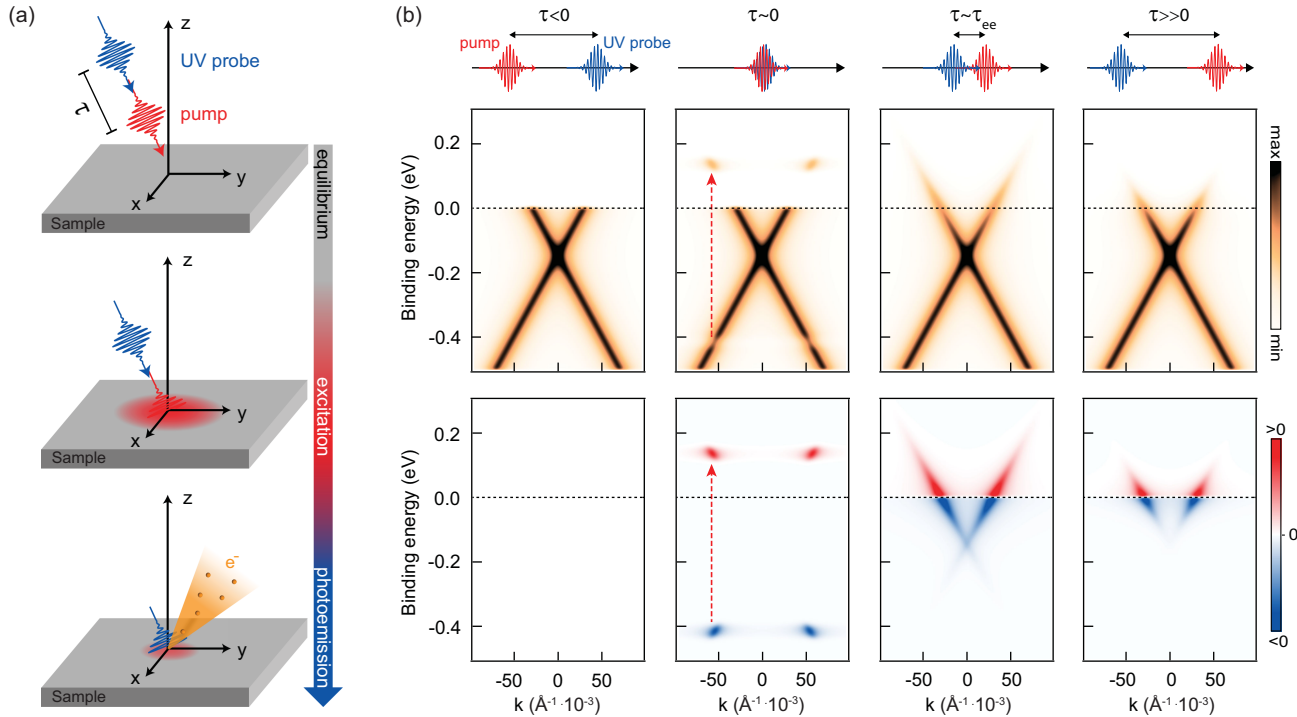
FIG. 2. Working principles of TR-ARPES. (a) Illustration of the pump-probe approach in TR-ARPES using two ultrafast laser pulses separated by time interval $\tau > 0$. The pump pulse drives the system out of equilibrium, and the probe pulse triggers the photoemission process. (b) Simplified sketch of the pump-induced evolution of the TR-ARPES signal for a Dirac cone dispersion. Top row: TR-ARPES maps for different pump-probe delays τ (τ_{ee} defines the electron-electron thermalization time). The red dashed arrow indicates the pump photon energy and related vertical optical transition from occupied into unoccupied states. Bottom row: differential TR-ARPES maps highlight the pump-induced redistributions of spectral weight.

plays an important role in the subsequent photoemission process elicited by the second photon.

A. General description

Since TR-ARPES extends conventional ARPES into the time domain, a description of the transient photoemission signal requires an introductory overview of its *equilibrium* counterpart. ARPES is a photon-in electron-out spectroscopic technique that grants direct insight into the electronic properties of matter and has already been extensively discussed in detail in several reviews (Damascelli, Hussain, and Shen, 2003; Damascelli, 2004; Lu *et al.*, 2012; Gedik and Vishik, 2017; Lv, Qian, and Ding, 2019; Sobota, He, and Shen, 2021; Zhang, Pincelli *et al.*, 2022). As depicted in Fig. 3, incoming light with photon energy $h\nu$ greater than the material's work function (ϕ, typically around 4 to 5 eV) may eject electrons from the sample's surface via the photoelectric effect. A fraction of such photoelectrons are collected and discriminated by a photoemission spectrometer to map the material's electronic structure. By taking advantage of the momentum and energy conservation laws, one can relate the kinetic energy E_k and angles of emission (θ, φ) of photoelectrons to the binding energy E_B and crystal momentum $\hbar \mathbf{k}$ of electrons inside the solid. In particular, the retrieved component of the crystal momentum parallel to the material's surface is proportional to the square root of the photoemitted electron's kinetic energy $\hbar \mathbf{k}_{\parallel} = \sqrt{2mE_k} \sin\theta$. This relation naturally implies that a

larger photon energy (and consequently a larger kinetic energy of the photoelectrons $E_k = h\nu - \phi - |E_B|$) grants access to a larger portion of momentum space within or beyond the first BZ. The perpendicular component of the photoelectron wave vector $\mathbf{k}_\perp$ is not conserved during the photoemission process, due to the breaking of translational symmetry at the sample's surface, but it can be experimentally estimated via photon-energy-dependent ARPES measurements.

While ARPES is commonly associated with the investigation of static (or equilibrium) electronic properties of matter and TR-ARPES is associated with the exploration of ultrafast (within the femtosecond to picosecond timescales) electron dynamics, this simplified dichotomy is not entirely correct: equilibrium ARPES itself offers valuable information on intrinsic electrodynamics in materials since removing an electron (i.e., generation of a photohole) leaves the system in an excited state. The propagation of an electron (or photohole) with momentum $\mathbf{k}$ and energy ω through an interacting system is captured by the Green's-function formalism, which characterizes the probability that a system will evolve into a different state upon addition or removal of an electron. Following the existing ARPES reviews, it can be shown that the ARPES signal is intimately related to the system's Green's function $G(\mathbf{k}, \omega)$, and thus to fundamental dynamical interactions. Under the sudden approximation and for a single-band system (and neglecting energy and momentum resolutions, as well as extrinsic background contributions), the equilibrium ARPES intensity can be calculated via Fermi's golden rule as

$$I(\mathbf{k}, \omega) = A(\mathbf{k}, \omega)|M(\mathbf{k}, \omega)|^2 f(\omega), \qquad (1)$$

where $A(\mathbf{k}, \omega) = -(1/\pi)\mathrm{Im}\,G(\mathbf{k}, \omega)$ is the one-particle removal spectral function, which encompasses both the single-particle band structure $\epsilon_{\mathbf{k}}$ and all many-body correlation effects embedded in the electron self-energy $\Sigma(\mathbf{k}, \omega)$ (Mahan, 2000). Note that $I(\mathbf{k}, \omega)$ also depends on two other terms, namely, the photoemission matrix element $M(\mathbf{k}, \omega)$, which connects the initial and final states of the photoemitted electron, and the Fermi-Dirac distribution function $f(\omega)$.

In the hypothetical scenario of a noninteracting system, upon the removal of an electron with energy $\epsilon_{\mathbf{k}}$, the system left behind would not undergo any relaxation process, and the spectral function would consist of a single line centered at the band energy $\epsilon_{\mathbf{k}}$, i.e., $A(\mathbf{k}, \omega) = \delta(\omega - \epsilon_{\mathbf{k}})$, In other words, the particle at $\epsilon_{\mathbf{k}}$ would have an infinite lifetime. Considering instead an interacting system, all the corrections to the non-interacting Green's function are taken into account by intro-ducing the electron self-energy $\Sigma(\mathbf{k}, \omega) = \Sigma'(\mathbf{k}, \omega) + i\Sigma''(\mathbf{k}, \omega)$. The spectral function is then written as (Mahan, 2000)

$$A(\mathbf{k}, \omega) = -\frac{1}{\pi}\frac{\Sigma''(\mathbf{k}, \omega)}{[\omega - \epsilon_{\mathbf{k}} - \Sigma'(\mathbf{k}, \omega)]^2 + [\Sigma''(\mathbf{k}, \omega)]^2}. \quad (2)$$

In Eq. (2) $\Sigma'(\mathbf{k}, \omega)$ and $\Sigma''(\mathbf{k}, \omega)$ encompass all energy renormalization and lifetime changes with respect to the non-interacting case, respectively. Intuitively, Σ' leads to a shift of the bare dispersion $\epsilon_{\mathbf{k}}$ to a new position $\tilde{\epsilon}_{\mathbf{k}} = \epsilon_{\mathbf{k}} + \Sigma'(\mathbf{k}, \omega)$, while Σ'' broadens the delta function from the noninteracting case. The single-particle lifetime $\tau_s(\mathbf{k})$, which describes all relaxa-tion properties of an excited single particle with energy $\epsilon_{\mathbf{k}}$, is inversely proportional to the imaginary part of the electron self-energy $\tau_s(\mathbf{k}) = \hbar/[2\Sigma''(\mathbf{k}, \omega)]$ and can be estimated using a detailed evaluation of the ARPES line shape. To this end, two main strategies are often combined, focusing on the energy and momentum dependence of the photoemission signal. The first approach is to analyze the energy dependence of the photo-emission intensity at a fixed momentum $\mathbf{k}^*$ in the so-called energy distribution curve (EDC). The second approach instead focuses on the momentum dependence at a fixed binding energy ω^* via the so-called momentum distribution curve (MDC). Generally, by combining the analyses of EDCs and MDCs in global fitting and/or self-consistent procedures, one can more rigorously model and interpret ARPES data; see Li *et al.* (2018) and Kurleto and Fink (2021).

Given that equilibrium ARPES already provides insights into fundamental single-particle electrodynamics, one may wonder what additional dynamical information TR ARPES provides. In contrast with its static counterpart, TR-ARPES observes changes of the sample's electronic distribution and structure upon pump-pulse excitation. Such optical excitations typically (i) modify the electronic distribution (beyond the equilibrium Fermi-Dirac statistics), (ii) generate specific collective excitations (such as phonons), and, consequently, (iii) lead to the emergence of new nonequilibrium and/or metastable phases of matter with no equilibrium counterpart. Thus, TR-ARPES does not access fundamental single-particle dynamics but rather maps how out-of-equilibrium electrons interact among themselves and with underlying collective
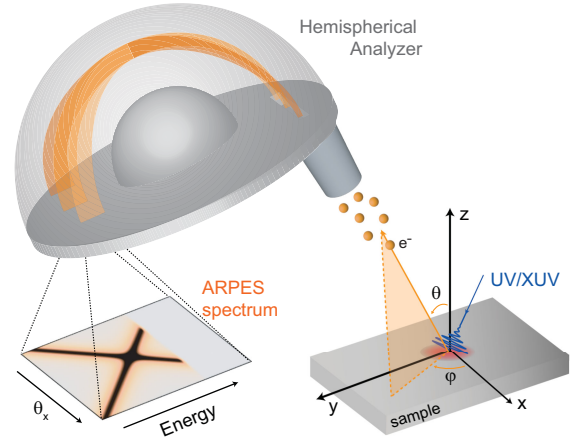

FIG. 3. Schematic configuration of an ARPES experiment. Light in the UV to XUV spectral range prompts the photoemis-sion of electrons from the sample. Photoelectrons are then collected by an electron analyzer (a hemispherical analyzer in the sketch), which discriminates them using both the kinetic energy and the angle of emission, thus generating the 2D ARPES spectrum.

excitations; TR-ARPES also maps how the electronic proper-ties of matter are affected by selective excitation of specific collective modes on their intrinsic timescales.

To further reinforce the critical role of TR-ARPES for advanced investigations of quantum materials, we emphasize that the design and engineering of new materials for applied purposes strongly relies on their dynamical (i.e., nonequili-brium) response rather than on their equilibrium properties. Indeed, every time that we apply a voltage (for example, in a microchip) or shine light (for instance, in a photovoltaic cell) to generate current, a nonequilibrium electronic distribution emerges, and its dynamical behavior determines the material's macroscopic working parameters, such as resistivity and energy-harvesting efficiency. Therefore, TR-ARPES is an effective technique not only for fundamental studies but also for characterizing out-of-equilibrium properties of quantum materials for future applications.

Section II.B provides a general description of the TR-ARPES intensity, both in a quasiequilibrium scenario and in a more strictly out-of-equilibrium framework, providing an overview of the wealth of information that can be extracted by analyzing the transient photoemission intensity, from a qualitative to a quantitative level. Afterward, a review of state-of-the-art TR-ARPES systems details how UV and XUV probe pulses are generated and coupled to ARPES systems, as well as which optical excitation schemes are commonly employed (Sec. II.C).

B. TR-ARPES intensity

1. Quasiequilibrium approximation

The description of a system's transient evolution upon perturbation by light is far from straightforward, especially when one considers the effects of the pump pulse's electric field, the potential appearance of new transient states of matter (see Sec. III.D), and other highly nonthermal processes
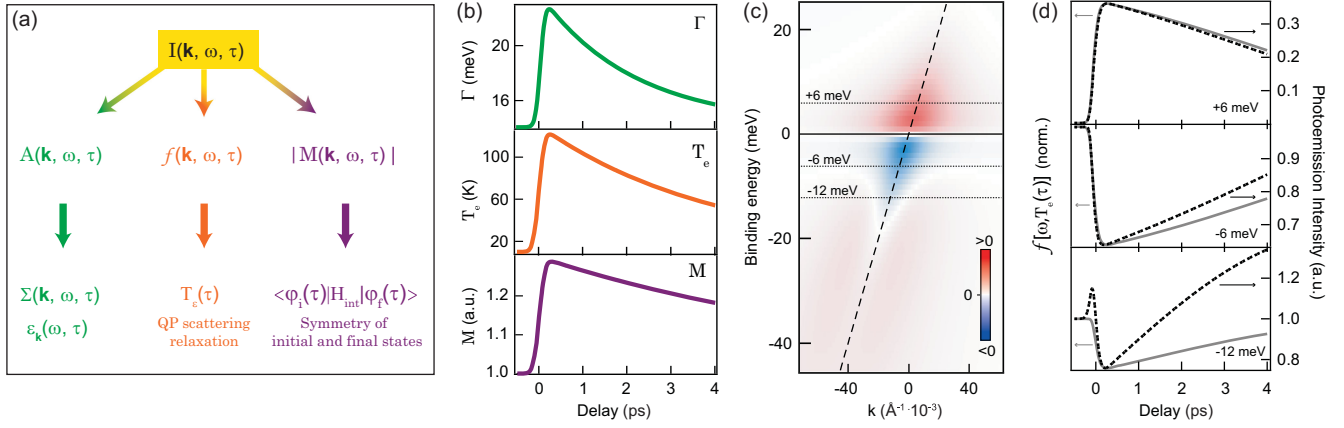
FIG. 4. Different components that constitute the transient photoemission intensity, with an illustration of how their intertwined contributions may be reflected in TR-ARPES data. (a) Diagram of the different contributions, and the corresponding encoded information, that characterize the transient photoemission intensity $I(\mathbf{k}, \omega, \tau)$. (b) Hypothetical temporal evolution of the spectral broadening Γ, electronic temperature T_e, and matrix element $|M|$. Γ is assumed to have a Fermi-liquid form $\Gamma(\tau) = \Gamma_{\mathrm{imp}} + \beta[\omega^2 + \pi^2 k_B^2 T_e^2(\tau)]$, where $\Gamma_{\mathrm{imp}} = 14$ meV and $\beta = 8$. The temporal evolution of Γ is displayed for $\omega = 0$. (c) Simulated differential ARPES spectrum at $\tau = 3$ ps of a linear dispersion (dashed black line) assuming the transient parameters displayed in (b) and accounting for the ω dependence of Γ. (d) Comparison between the transient evolution of the photoemission intensity at three different binding energies from (c) (black dashed lines, right axis) and the evolution of the electronic distributions given solely by $T_e(\tau)$ in (b) (gray solid lines, left axis) highlighting the discrepancy in their dynamics.

(Sentef *et al.*, 2013; Kemper *et al.*, 2017; Randi, Fausti, and Eckstein, 2017; Kemper, Abdurazakov, and Freericks, 2018). However, in most cases, after the initial light-induced excitation of the electronic bath, one can approximately assume that electrons thermalize into a quasiequilibrium state within a time span of a few tens to hundreds of femtoseconds (see Sec. V.A), and it has been shown that the adiabatic band picture (i.e., the unperturbed band structure) survives well even at zero pump-probe delay and high pump field intensities (Neufeld *et al.*, 2022). In such a scenario, the TR-ARPES signal for a single-band system can be approximated by extending the equilibrium formalism of Eq. (1) into the time domain τ [also known as the generalized Kadanoff-Baym approximation (Freericks and Kemper, 2021)],

$$I(\mathbf{k}, \omega, \tau) \simeq A(\mathbf{k}, \omega, \tau)|M(\mathbf{k}, \omega, \tau)|^2 f(\mathbf{k}, \omega, \tau). \quad (3)$$

A simple visual inspection of Eq. (3) reveals that the transient evolution of the photoemission intensity may arise from the complex interplay of several contributions, as depicted schematically in Fig. 4. The parallel evolution of all of the terms, namely, the electronic distribution $f(\mathbf{k}, \omega, \tau)$, the photoemission matrix elements $|M(\mathbf{k}, \omega, \tau)|^2$, and the spectral function $A(\mathbf{k}, \omega, \tau)$, can make the interpretation of $I(\mathbf{k}, \omega, \tau)$ challenging. Figure 4 highlights how changes in A (encoded in the change of spectral broadening Σ''), f (captured by the transient electronic temperature T_e), and $|M|$ can lead to a transient evolution of $I(\mathbf{k}, \omega, \tau)$ that cannot easily be explained in terms of a single contribution. Figure 4(d) compares the transient photoemission intensity at three different binding energies (black dashed curves) with the evolution of the electronic distribution based solely on the changes in T_e (solid gray curve). The evolution of the TR-ARPES signal does not necessarily mimic the transient electronic distribution [see the bottom of Fig. 4(d)] or the single-particle lifetime τ_s

[described by Γ in Fig. 4(b)]. Instead, it results from the complex interplay of the different contributions depicted in Fig. 4(a). The following discussion explains the transient evolution of all of the terms in Eq. (3) and how to interpret their intertwined contributions.

In the conventional ARPES scenario, the Fermi-Dirac distribution $f(\omega) = (1 + e^{\omega/k_B T_e})^{-1}$ does not have any momentum dependence and accounts for the fact that photoemission probes solely the occupied states. In contrast, in a TR-ARPES experiment the pump excitation promotes valence electrons into unoccupied states in specific regions of the 3D BZ, potentially leading to an electronic distribution that is highly anisotropic in momentum space, at least for short time delays $\tau \sim 0$. At later times, following thermalization processes (such as electron-electron, electron-impurity, and electron-boson scattering), hot electrons redistribute over the entire 3D momentum space, and $f(\mathbf{k}, \omega, \tau \gg 0)$ may be approximated using a $\mathbf{k}$-independent Fermi-Dirac distribution with a time-dependent effective electronic temperature $T_e(\tau)$. The light-induced emergence of a nonthermal electronic distribution at short pump-probe delays, together with the momentum resolution of TR-ARPES, provides a valuable approach to map the band dispersion of unoccupied states of quantum materials (for example, the topological surface state of 3D topological insulators) and a method to extract electronic band gaps and test *ab initio* evaluations of the band structure (for instance, the electronic band gap of transition-metal dichalcogenides), as discussed in Sec. III. Moreover, Sec. V showcases how, by tracking how carriers photoinjected into the unoccupied states thermalize and return to equilibrium conditions, TR-ARPES offers qualitative and quantitative information on multiparticle scattering processes (for example, electron dynamics in graphene), ultrafast changes of the screening and electronic dispersion (for instance, via the detection of coherent phonons), and
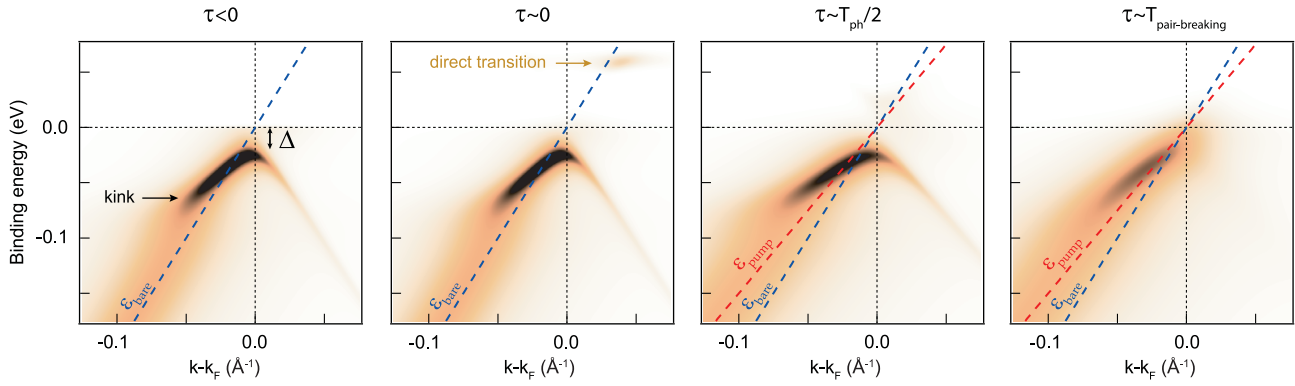
FIG. 5. Toy model depicting some of the challenges associated with the interpretation of the transient photoemission intensity for the case of a superconductor with gap Δ with a strong electron-phonon coupling that renormalizes the electronic dispersion (also known as the kink). Multiple effects may occur, such as direct optical transitions, transient modifications of the bare dispersion from the unperturbed ε_{bare} to ε_{pump} after excitation (dashed blue and red lines, respectively), enhancement of the electronic temperature, filling of the superconducting gap, and softening of the electron-phonon band-structure renormalization. These effects are often intertwined, which complicates the interpretation of the TR-ARPES signal.

fundamental electron-boson coupling constants (for example, by detecting quantized electron decay processes).

Next, under the sudden approximation, the one-electron dipole matrix element takes a simple form $M \propto \langle \phi_i^{\mathbf{k}} | H_{int} | \phi_f^{\mathbf{k}} \rangle$ and connects the initial (i) and final (f) states of the photoemitted electron via the light-matter interaction Hamiltonian $H_{int} \propto \mathbf{A} \cdot \mathbf{p}$ (where $\mathbf{p}$ is the electron momentum operator and $\mathbf{A}$ is the electromagnetic vector potential). $|M|^2$ encodes the dependence of the photoemission intensity on the polarization and photon energy of the probe beam, as well as the experimental geometry (for example, the angle of incidence, sample orientation, and orientation of the entrance slit for hemispherical electron analyzers). In this regard, detailed polarization and photon-energy-dependent ARPES measurements have been proven able to provide direct information on the orbital character of the initial photoemission state and its spatial extent (Gierz *et al.*, 2011; Cao *et al.*, 2013; Zhu *et al.*, 2013; Moser, 2017; Day *et al.*, 2019; Schüler *et al.*, 2022). In TR-ARPES investigations, the transient evolution of the photoemission matrix element has commonly been neglected. However, possible transient modifications of $M(\mathbf{k}, \omega, \tau)$ have recently been theoretically acknowledged (Freericks and Krishnamurthy, 2016) and experimentally demonstrated (Boschini *et al.*, 2020a). In particular, in multiorbital systems where the initial state wave function may result from a complex interplay of different or layer-dependent orbital characters, $M(\mathbf{k}, \omega, \tau)$ can have a non-negligible impact on the transient evolution of $I(\mathbf{k}, \omega, \tau)$. As a paradigmatic example, a light-induced modulation of the atomic distances via emission of coherent and/or incoherent phonons can dynamically change the orbital mixing of the probed states, and hence $|M|^2$. Therefore, unless single-band systems with a well-defined orbital character are studied, the possibility that the transient evolution of $I(\mathbf{k}, \omega, \tau)$ may be linked to the evolution of $M(\mathbf{k}, \omega, \tau)$ should always be considered. Indeed, Boschini *et al.* (2020a) recently showed that a probe-polarization-dependent study of the TR-ARPES signal can offer direct evidence of the transient changes of matrix elements. We foresee several future TR-ARPES investigations

being able to precisely track light-induced modifications of the symmetry of the initial photoemission state wave function by performing detailed polarization or dichroism measurements (Schüler and Beaulieu, 2022; Schüler *et al.*, 2022).

Last, the third term of Eq. (3) is the spectral function $A(\mathbf{k}, \omega, \tau)$, which accounts for all transient changes of the band structure and density of states (DOS), as well as many-body interactions. Note that an optical pump may modify the bare electron dispersion in the adiabatic limit by driving coherent or incoherent phonons (see Sec. V.B, which addresses periodic modulations of the electronic dispersion in topological insulators and Fe-based superconductors), or transiently changing many-body interactions, i.e., $\Sigma(\tau)$, with the filling of the superconducting gap of cuprates as an emblematic example. Transient evolution of the self-energy can be the by-product of various effects ranging from transient modification of the screening and scattering phase space to light-induced phase transitions (Secs. III–V). All of the different contributions to $A(\mathbf{k}, \omega, \tau)$ are often deeply intertwined and difficult to disentangle.

As a representative thought experiment that emphasizes the plethora of possible distinct contributions to $A(\mathbf{k}, \omega, \tau)$, consider a superconductor with an s-wave gap Δ, critical temperature T_c, and linear dispersion in the normal state, as depicted in Fig. 5. Assuming that the electronic bath is strongly coupled to an Einstein phonon with energy $\Omega_0 \sim 2\Delta$ (similar to the phenomenology in the cuprates), a renormalization of the band structure occurs, also known as a *kink* (Lanzara *et al.*, 2001), as shown by the unperturbed electronic band dispersion at low temperatures ($T < T_c$) for $\tau < 0$ (far left panel of Fig. 5). The optical excitation populates unoccupied states at $\tau \sim 0$, thus creating a nonequilibrium electronic distribution. As a consequence of the transient redistribution of the electronic density, excitation of phonon modes may occur: coherent phonons triggered via displacive mechanisms, as well as incoherent phonons emitted through the thermalization process of the photoinduced nonthermal electronic distribution or via anharmonic decay of coherent phonons. Such an increase of the phonon temperature (on
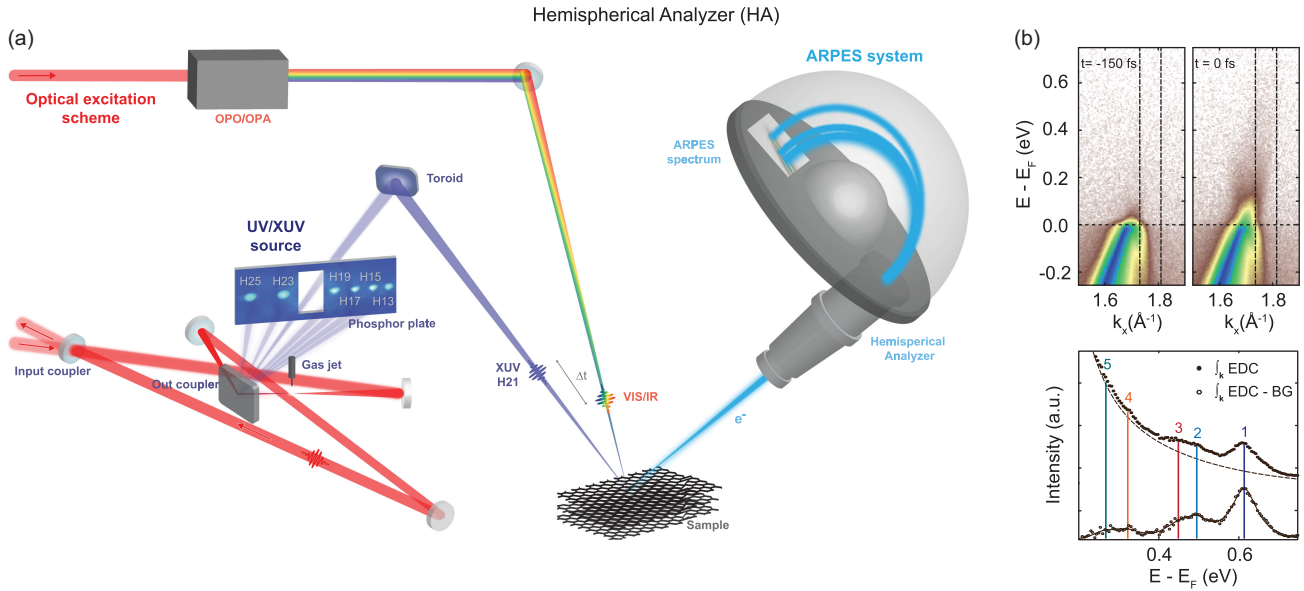
FIG. 6. Illustration of a TR-ARPES system based on a hemispherical analyzer (HA) along with a sample dataset that showcases its capabilities. (a) Illustration of the three main components of a state-of-the-art TR-ARPES system: the optical schemes for the pump excitations, the generation of the ultraviolet and/or extreme ultraviolet probe pulses, and the coupling to the ARPES system. (b) TR-ARPES data of graphite acquired with 25 eV probe and 1.2 eV pump. The high energy and momentum resolution, as well as the dynamic range, achievable with a hemispherical analyzer allowed the detection of multiple peaks corresponding to both direct transitions and photon-induced replicas. In fact, although (top panel) these peaks are not obvious in the ARPES intensity maps, (bottom panel) they stand out from the quasithermalized electron background when the EDC is integrated in momentum, at energies up to 0.6 eV above E_F. Adapted from Na, 2022.

timescales comparable to $1/2$ of the phonons' period) can transiently change the electronic dispersion (discussed in Sec. V), as indicated by the red line in the right panels of Fig. 5. Afterward, the superconducting gap might fill up on a timescale determined by pair-breaking events (i.e., inelastic electron scattering breaking Cooper pairs). In addition, the transient change of the DOS at the Fermi level due to this filling of the superconducting gap enhances the available electronic scattering phase space, consequently changing the kink renormalization strength; see Sec. V.C and Eq. (10).

Overall, the examples of Figs. 4 and 5 highlight in a simplified fashion some of the challenges associated with the interpretation of TR-ARPES data for a complex system with intertwined orders, emphasizing once more that TR-ARPES implies not only probe population dynamics but also transient many-body interactions encoded in the one-particle spectral function. Within the quasiequilibrium approximation, the spectral function and the related self-energy can still be explored via equilibrium analysis methods (for example, extracting Σ via analysis of the ARPES line shape). Moreover, after the initial thermalization time (which depends on the specific sample and excitation parameters), a transient electronic temperature $T_e(\tau)$ can be defined. As discussed in Sec. V.A, $T_e(\tau)$ can differ from the temperature of the lattice, and in general of other bosonic modes (such as phonons and magnons), over the delay range determined by intrinsic electron-boson scattering processes. Within this time interval, TR-ARPES can be used in concert with equilibrium ARPES to determine whether lifetime broadening and band-structure renormalization effects arise from pure electron-electron effects or interactions involving bosons. For example, Zonno

et al. (2021) recently compared the equilibrium and transient temperature dependencies of the quasiparticle peak of Bi-based cuprates, demonstrating that Fermi-liquid theory (i.e., solely electron-electron interactions) properly accounts for the low-energy part of the self-energy in the gapless nodal direction.

In conclusion, the TR-ARPES technique innately correlates transient redistributions of the carrier density with changes to the many-body interactions, electronic and bosonic DOSs, and the symmetry of the initial and final photoemission states. To the extent that transient contributions to Eq. (3) can be disentangled, TR-ARPES can directly and unambiguously identify and demystify light-induced phenomena in condensed matter.

2. Out-of-equilibrium description

The quasiequilibrium approximation of the TR-ARPES signal discussed in Sec. II.B.1 is a valid approach for describing the transient evolution of systems when the pump and probe do not overlap. The evaluation of the TR-ARPES signal becomes increasingly challenging when one wants to account fully for light-induced dynamical effects and finite time width of the probe pulse (Freericks, Krishnamurthy, and Pruschke, 2009; Schüler and Sentef, 2021). In particular, assuming a single-band system and constant matrix elements, the TR-ARPES intensity is computed from the probe-pulse weighted relative-time Fourier transform of the lesser Green's function $G^{<}_{\mathbf{k}(t,t')}$ as

$$I(\mathbf{k}, \omega, \tau) = \mathrm{Im} \int dt dt' \, p(t, t', \tau) e^{i\omega(t-t')} G^{<}_{\mathbf{k}}(t, t'), \quad (4)$$

where p corresponds to a two-dimensional Gaussian probe centered at $(t, t') = (\tau, \tau)$.

This review does not encompass theoretical challenges related to the interpretation of the TR-ARPES signal; we refer the interested reader to the relevant literature for further discussion (Freericks, Krishnamurthy, and Pruschke, 2009; Freericks *et al.*, 2009; Tao and Zhu, 2010; Sentef *et al.*, 2013; Kemper *et al.*, 2014, 2017; Braun *et al.*, 2015; Xu, Morimoto *et al.*, 2019; Perfetto, Bianchi, and Stefanucci, 2020; Schwarz, Fauseweh, and Manske, 2020; Eckstein, 2021; De Giovannini *et al.*, 2022; Marini, Perfetto, and Stefanucci, 2022). However, it is important to recognize that the similarities between equilibrium ARPES and TR-ARPES discussed in Sec. II.B.1 may be deceptive for time delays comparable to the system's characteristic dephasing times, or when new electonic states with no equilibrium counterpart (such as Floquet-Bloch states) emerge. Although the TR-ARPES signal is commonly evaluated by assuming that the various many-body contributions are linearly proportional to the overall population decay rate, that decay rate does not originate simply from the self-energy, and it is often not possible to separate scattering rates in the TR-ARPES signal (Kemper, Abdurazakov, and Freericks, 2018). Following the experimental evidence of Yang *et al.* (2015), Kemper, Abdurazakov, and Freericks (2018) showed that population dynamics are controlled by the difference between the distributions for the Green's function and the self-energy.[1] Most of the studies reviewed here rely on the assumption that it is possible to separate different relaxation processes in the time domain or that the self-energy alone governs the population decay rate. Although these are not universally true, as discussed in Sec. V, we emphasize that (i) when many-body interactions are dominated by a single-scattering process, the relaxation rate is proportional to the self-energy and (ii) when scattering processes take place on sufficiently different time-scales, it is generally possible to separate relaxation rates (Kemper, Abdurazakov, and Freericks, 2018).

C. State-of-the-art TR-ARPES

Generally speaking, to perform a TR-ARPES experiment one has to generate pump and ultraviolet pulses and couple them in the ARPES chamber, as schematically depicted in Fig. 6(a). For this reason, the design and development of the TR-ARPES technique has relied on close cooperation between the photoemission and ultrafast laser communities. This section reviews methods and approaches for generating pump and ultraviolet pulses for TR-ARPES, as well as commonly used ARPES systems, detectors, and coupling methods.

1. UV and XUV sources

Generation of UV and XUV probe pulses to photoemit electrons has historically relied on three approaches:

---

[1]The distribution functions for the Green's function G and self-energy Σ are, respectively, $f^G(\tau, \omega) = iG_{\mathbf{k}}^<(\tau, \omega)/2\mathrm{Im}G_{\mathbf{k}}^R(\tau, \omega)$ and $f^\Sigma(\tau, \omega) = i\Sigma_{\mathbf{k}}^<(\tau, \omega)/2\mathrm{Im}\Sigma_{\mathbf{k}}^R(\tau, \omega)$. In equilibrium, f^G and f^Σ converge to the Fermi-Dirac distribution. However, it can be shown that the population decay $df_{\mathbf{k}}(\tau)/d\tau \propto f^G(\tau, \varepsilon_{\mathbf{k}}) - f^\Sigma(\tau, \varepsilon_{\mathbf{k}})$.
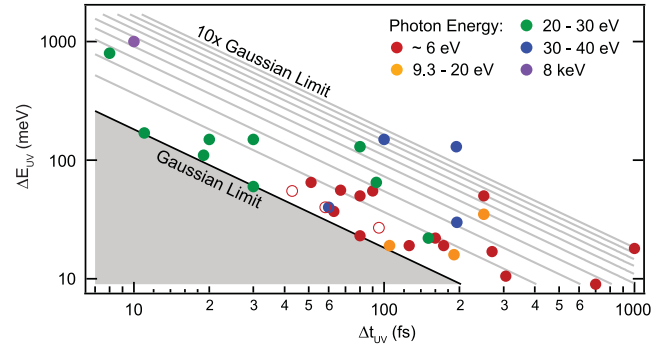
FIG. 7.   Pulse duration and bandwidth of UV and XUV probes from different TR-ARPES studies. The black line indicates the Gaussian Fourier limit, while gray lines represent integer multiples of this fundamental limit up to $n = 10$. Adapted from Gauthier *et al.*, 2020.

(i) frequency conversion with nonlinear crystals, (ii) highly cascaded harmonic generation in the gas phase, and (iii) high-order harmonic generation (HHG). Although HHG has been applied to photoemission spectroscopy since the 1990s (Haight and Peale, 1994), the advent of reliable and commercially available ultrafast laser sources used to generate UV light via nonlinear crystals (Gauthier *et al.*, 2020) has significantly accelerated the development of TR-ARPES. In the latter case, ~6 eV UV probe pulses are obtained by quadrupling the fundamental output of Ti:sapphire lasers (~1.5 eV photon energy) (Carpene *et al.*, 2009; Faure *et al.*, 2012; Smallwood, Jozwiak *et al.*, 2012) or via sum-frequency generation in a Yb-based laser (~1.2 eV fundamental photon energy) (Boschini *et al.*, 2014) via a cascade of nonlinear crystals, specifically, β-BaB$_2$O$_4$ (BBO). The technical simplicity of low-photon-energy optical setups has greatly favored early investigations of ultrafast electron dynamics near the Brillouin zone center of quantum materials, such as topological insulators. In addition, 6 eV TR-ARPES systems have historically granted easy access to high-repetition-rate operation (100 kHz–100 MHz), considerably improving the signal-to-noise ratio of TR-ARPES spectra, and have provided broad tunability of the UV bandwidth enabling high temporal ($<$60 fs) or energy ($<$10 meV) resolutions, depending on the particular experimental needs (Gauthier *et al.*, 2020). The ability to continuously tune the UV photon energy in the ~5.3–7 eV range by combining different nonlinear crystals was recently demonstrated by Yang, Tang *et al.* (2019) and Bao, Zhong *et al.* (2022).

XUV-based TR-ARPES systems grant access to ultrafast electron dynamics over the entire momentum space of quantum materials (Mathias *et al.*, 2007; Dakovski *et al.*, 2010; Heyl *et al.*, 2012; Frietsch *et al.*, 2013; Eich *et al.*, 2014; Plötzing *et al.*, 2016; Rohde *et al.*, 2016; Buss *et al.*, 2019; Heber *et al.*, 2022). However, the challenges related to the generation of stable and bright XUV sources operating at a high repetition rate, as well as to coupling XUV light in ARPES systems, have considerably slowed down the operation of the XUV-based TR-ARPES system. The advent of high-repetition-rate ($>$100 kHz) and narrow-bandwidth XUV-based TR-ARPES systems (Chiang *et al.*, 2012; Mills *et al.*,
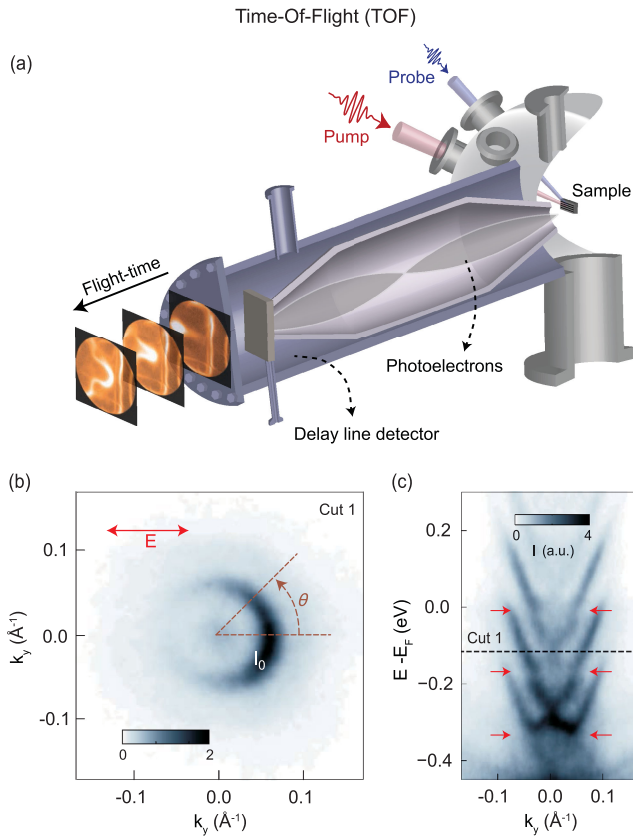
FIG. 8. Operating principles of a time-of-flight (TOF) spectrometer. (a) Sketch of a TOF detector. Adapted from Zong, 2021. (b) One-shot constant energy cut at −0.12 eV. (c) ARPES spectrum along the k_y direction acquired via TOF on Bi_2Se_3 upon mid-IR light excitation. These maps show the appearance of Floquet-Volkov states when the impinging electric field is oriented along the k_x direction (discussed in Sec. III.D) and exemplify the ability of TOF detectors to measure the photoemission intensity simultaneously over 2D momentum space, for example, $I(E, k_x, k_y)$. (b),(c) Adapted from Mahmood et al., 2016.

2019; Puppin et al., 2019; Sie, Rohwer et al., 2019; Lee et al., 2020; Peli et al., 2020; Guo et al., 2022) has significantly improved the signal-to-noise ratio and enabled access to the transient evolution of low-energy spectral features previously hidden in low-repetition-rate large-bandwidth XUV-based TR-ARPES systems. Moreover, the use of high-repetition-rate systems helps reduce the space-charge effects, improving the energy resolution and determination of the position of the Fermi level (Passlack et al., 2006; Hellmann et al., 2009; Corder et al., 2018). For a more comprehensive review of the light sources employed in TR-ARPES systems, see Na, Mills, and Jones (2023).

Finally, the development of high-repetition-rate free-electron laser facilities in principle paves the way to fully tunable TR-ARPES experiments in a broad spectral range from XUV to soft x ray (Oloff et al., 2016; Rossbach, Schneider, and Wurth, 2019; Kutnyakhov et al., 2020; Shokeen et al., 2023). These new facilities will enable exploration of ultrafast electron dynamics in highly dispersive 3D systems, as well as permitting element-specific studies via resonant TR-ARPES.

Early TR-ARPES works have historically focused on temporal resolution at the expense of energy resolution, partially impairing their ability to resolve energy gaps and renormalization effects. Independently of how UV or XUV light is generated, over the past two decades we have witnessed different compromises between the time and energy resolutions (whose Fourier limit for Gaussian pulses can be expressed as $\Delta E \Delta \tau \geq 4\hbar \ln 2 \sim 1.825 \text{ eV fs}$; see Fig. 7), which have enabled diverse TR-ARPES investigations ranging from tracking ultrafast electron dynamics with sub-15-fs temporal resolution (Rohde et al., 2016, 2018) to the detection of sub-20-meV superconducting gaps (Smallwood, Hinton et al., 2012; Parham et al., 2017; Boschini et al., 2018).

2. Optical excitation scheme

TR-ARPES has primarily relied on the fundamental output of Ti:sapphire– and Yb-based laser sources (1.55 and 1.2 eV, respectively) or their second harmonics (3.1 and 2.4 eV, respectively) for the pump excitation. This historical focus led to the initial groundbreaking demonstrations of the capabilities of the TR-ARPES technique in a variety of different systems, as discussed throughout this review. Although there are several specific cases where near-infrared or visible light is needed (such as the excitation of bright excitons or the photodoping of charge-transfer insulators), the continuing almost exclusive reliance on near-infrared pump excitations does not take advantage of the full spectrum of opportunities to employ optical excitation to manipulate electron properties and prompt the emergence of metastable phases of matter. Indeed, near-IR and visible light usually redistributes electrons and holes over the entire momentum space (potentially leading to quasithermal states with effective electronic temperatures as high as thousands of kelvins) and does not allow selective coupling to specific low-energy excitation without affecting the electronic bath.

Recent all-optical investigations demonstrated that intense long-wavelength light excitation can selectively drive the emergence of new quantum phenomena in quantum materials with minimal coupling to the electronic bath (Fausti et al., 2011; Mitrano et al., 2016; Liu et al., 2020; McIver et al., 2020; Disa, Nova, and Cavalleri, 2021). To date the development of TR-ARPES systems with long-wavelength excitation capabilities remains at an early stage, but pioneering studies have demonstrated the feasibility of these experiments by showing groundbreaking results with midinfrared pump pulses on topological insulators, graphene, black phosphorus, and charge-ordered systems (Wang et al., 2013; Gierz et al., 2015b; Kuroda et al., 2016; Monney et al., 2016; Chávez-Cervantes et al., 2019; Ito et al., 2023; Zhou et al., 2023), as well as terahertz excitation of topological insulators (Reimann et al., 2018).

Finally, note that a ubiquitous effect of any pump excitation is to increase the sample's average temperature. Such thermal effects can be mitigated by decreasing the repetition rate for fixed absorbed fluence or by pumping in a spectral range for which the material is (quasi)transparent. Nevertheless, maintaining the sample temperature in the sub-10-K range for negative pump-probe delays is nearly always challenging.

3. ARPES systems and coupling to light sources

TR-ARPES systems rely on state-of-the-art ARPES technology; see the equilibrium ARPES reviews in the literature for comprehensive descriptions (Gedik and Vishik, 2017; Lv, Qian, and Ding, 2019; Sobota, He, and Shen, 2021; Zhang, Pincelli *et al.*, 2022). The sample is commonly prepared by cleaving in ultrahigh-vacuum (commonly $p < 5 \times 10^{-10}$ mbar) conditions, and positioned in front of the electron detector via five- or six-axis manipulators. To investigate ultrafast electron dynamics in low-temperature phases, sub-10-K cryogenic cooling is commonly available, although the omnipresent pump-induced thermal effects (even in perturbative pump regimes) often limit the achievable base temperature. Currently one of three main electron detectors is used: time-of-flight (TOF) spectrometers, momentum microscopes (MMs), or hemispherical analyzers (HAs) (Sobota, He, and Shen, 2021; Zhang, Pincelli *et al.*, 2022). Figures 6, 8, and 9, respectively, illustrate the advantages of these three different electron detectors. In particular, TOF spectrometers allow for the detection of isoenergy contours simultaneously over 2D momentum space; MMs can operate in both spatial and momentum modes, enabling the detection of photoelectrons emitted from specific micrometer regions (such as exfoliated samples); and HAs, although they require the sample to be mechanically moved or the captured electrons to be deflected via voltages to map the entire 2D momentum space, generally provide higher energy and momentum resolutions, as well as a larger dynamic range in photoemission intensity. We mention that an affordable new detector named FeSuMa (from Fermi Surface Mapper) was recently developed (Borisenko *et al.*, 2023) and used in TR-ARPES investigations (Majchrzak, Zhang *et al.*, 2023).

TR-ARPES systems operating solely with UV probe light (for example, 6 eV) do not require differential pumping stages to deliver UV into the chamber: UV light can be generated in air and delivered to the sample through windows transparent in the UV spectral range (for example, MgF_2 or CaF_2). However, the trajectories of photoelectrons generated by 6 eV probe light, which have low kinetic energy, may be affected by stray fields inside the ARPES chamber, such as the electric fields caused by the difference in work function between the sample and its sample holder, and correction techniques may be required (Fero *et al.*, 2014; Gauthier *et al.*, 2021). However, XUV pulse generation and propagation need to take place in vacuum, and different strategies have been implemented to connect HHG generation chambers (operating commonly in the 10^{-2}–10^{-4} mbar range) to ARPES endstations, such as metallic windows or differential pumping lines with multiple pumping stages and/or capillaries. Moreover, XUV beamlines comprise not only HHG chambers but also monochromator systems to select specific harmonics. Various methods with different levels of complexity are employed to sort harmonics, ranging from simple metallic filters to multilayer mirrors, Brewster plates, and gratings (Mathias *et al.*, 2007; Dakovski *et al.*, 2010; Poletto and Frassetto, 2010; Frietsch *et al.*, 2013; Tusche, Krasyuk, and Kirschner, 2015; Buss *et al.*, 2019; Mills *et al.*, 2019; Puppin *et al.*, 2019; Lee *et al.*, 2020; Heber *et al.*, 2022). Finally, the recent development of XUV light sources with full polarization control
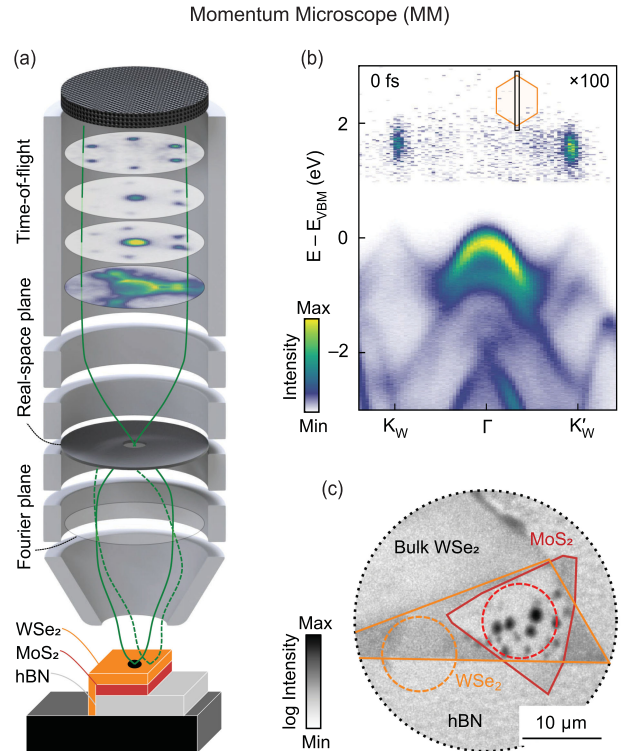

FIG. 9. Experimental configuration of a momentum microscope (MM) setup, which can locate the heterostructure in the real-space acquisition mode with micrometer resolution. (a) Illustration of a MM detector studying a $WSe_2/MoS_2/hBN$ sample. (b) The acquired ARPES map at 0 fs shows the valence bands of WSe_2, MoS_2, and hBN, as well as the bright A excitons of WSe_2. (c) Regions of interest in the study indicated by the red and orange 10-μm-diameter circles. Adapted from Schmitt *et al.*, 2022.

(linear and circular) (Comby *et al.*, 2022) in combination with the rise of high efficiency spin detectors (Gotlieb *et al.*, 2013) has now positioned the community to add spin or dichroic degrees of freedom to the TR-ARPES technique, promoting novel studies of spin and orbital dynamics of quantum materials over the entire momentum space; see Sec. VII.

III. MAPPING UNOCCUPIED AND TRANSIENT STATES

TR-ARPES is frequently employed to map nonthermal electronic distributions in unoccupied states and to explore light-driven modifications of the electronic band dispersion. The mapping of unoccupied states is probably the most straightforward use of TR-ARPES: by taking advantage of pump pulses (commonly in the near-infrared or visible range) to redistribute the electronic population above the Fermi level and across momentum space, TR-ARPES grants access to the dispersion of unoccupied electronic states unattainable in conventional ARPES experiments. Note that although inverse photoemission spectroscopy would be an alternative technique to map the dispersion of unoccupied states, its poor energy resolution and low cross section make it unsuitable for exploring low-energy (<1 eV) unoccupied states. Moreover, TR-ARPES enables momentum-resolved investigations of
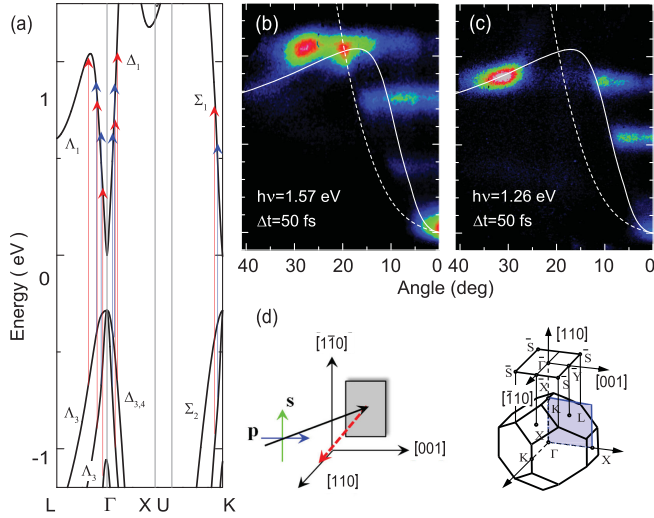
FIG. 10. TR-ARPES mapping of the unoccupied states of InSb semiconductor shows how different pump energies access distinct optical transitions. (a) Band structure of InSb with available interband optical transitions with 1.57 eV (red arrows) and 1.26 eV (blue arrows) photons. TR-ARPES spectra of InSb(110) acquired 50 fs after p-polarized (b) 1.57 eV and (c) 1.26 eV pump excitation. The solid and dashed lines represent the CB dispersion along the high-symmetry directions Γ-L and Γ-X, respectively. (d) Illustration of the surface and bulk BZ for InSb(110). Adapted from Tanimura, Kanasaki, and Tanimura, 2015.

how intense light excitation may induce both sizable renormalizations of the electronic dispersion and the appearance of electronic states with no equilibrium counterpart.

Sections III.A and III.B present a few emblematic examples of how TR-ARPES maps the unoccupied conduction band of III-V and III-VI semiconductors and $2H$ transition-metal dichalcogenides, as well as the topological surface state in 3D topological insulators. Next, Sec. III.C reviews the recent observation of bright and dark excitons in momentum space. Finally, Sec. III.D discusses the emergence of Floquet-Bloch states.

A. Conduction band of semiconductors

1. III-V group and III-VI semiconductors

GaAs and InSb are prototypical III-V group semiconductors extensively used in optoelectronic devices and sensors. Therefore, precise mappings of their unoccupied conduction band (CB), available optical transitions, and ultrafast scattering processes over the entire Brillouin zone are of crucial importance. Taking advantage of different pump photon energies in the visible range of the spectrum, multiple groups have precisely mapped optical transitions into the unoccupied CB and subsequent intravalley and intervalley scattering processes in both GaAs and InSb via TR-ARPES (Kanasaki, Tanimura, and Tanimura, 2014; Tanimura, Kanasaki, and Tanimura, 2015; Tanimura et al., 2016; Sjakste, Vast et al., 2018; Tanimura, Tanimura, and Kanasaki, 2021). TR-ARPES data acquired on InSb by Tanimura, Kanasaki, and Tanimura (2015) provide a key illustrative example. Figure 10 shows the mapping of the

unoccupied states at 50 fs pump-probe delay for two different excitation schemes: p-polarized 1.57 and 1.26 eV pumps. The solid and dashed lines in Figs. 10(b) and 10(c) highlight the dispersion of the CB along two crystallographic directions, namely, Γ-L and Γ-X. The differing distributions of the intensity hot spots observed in Fig. 10 showcase the capability of accessing distinct optical transitions from the heavy-hole, light-hole, and split-off valence bands, depending on the pump photon energy utilized. By tracking the temporal evolution of these photoinjected electrons over the entire Brillouin zone, it is possible to study intravalley and intervalley relaxation processes. In the case of InSb, TR-ARPES data show that electrons injected in the Γ valley with an energy exceeding the minimum of the L valley undergo intervalley scattering on a sub-50-fs scale and relax from L back to Γ within $\sim$0.8 ps. Instead, if the energy of photoexcited electrons does not exceed the minimum of the L valley, their decay within the Γ valley is governed by impact ionization processes (Tanimura, Kanasaki, and Tanimura, 2015).

As another example, InSe is a III-VI group semiconductor layered chalcogenide, with a direct bulk band gap of $\sim$1.25 eV. As in the previous discussion of InSb, TR-ARPES at different excitation energies allowed Chen et al. (2018) to accurately map its unoccupied states and track how nonthermal carriers accumulate at the bottom of the CB at Γ or scatter into a valley at the M point. More recently they reported the ultrafast response of a quasi-2D electron gas induced on the surface of InSe via Cs doping (Chen et al., 2020). This study represented the first ultrafast mapping of the light-induced population of a quasi-2D electron gas, and by accessing the dynamics of the photoemission intensity and photoinjected excess energy on a picosecond timescale, it also offers a qualitative estimate of the electron-phonon scattering processes as a function of the Cs doping; see also Sec. V.A. In particular, they discussed the observed $\sim$0.5 ps relaxation time in terms of the coupling of optically excited quasi-2D electrons with optical phonons via the Frohlich mechanism (Chen et al., 2020).

2. Transition-metal dichalcogenides

Transition-metal dichalcogenides (TMDs), especially in the 2D limit, have attracted considerable interest for the development of novel valleytronic devices. While centrosymmetric bulk TMDs ($2H$ phase) present an indirect band gap between the top of the valence band (VB) at Γ and the bottom of the CB at the corner of the hexagonal Brillouin zone (i.e., the K point), monolayer TMDs exhibit a direct band gap at K. When one considers the monolayer limit, the lack of inversion symmetry in concert with strong spin-orbit coupling lifts the degeneracy of two adjacent K points, commonly identified as K and K'. The different valley pseudospins associated with K and K' make valley-selective electronic excitations with circularly polarized light possible (Mak et al., 2012; Zeng et al., 2012). While this effect should be forbidden in bulk materials, a hidden pseudospin texture (X. Zhang et al., 2014) may appear as a consequence of the local breaking of inversion symmetry in some sections of the unit cell, leading to dichroic effects even in $2H$ TMDs; see Sec. VII.B.
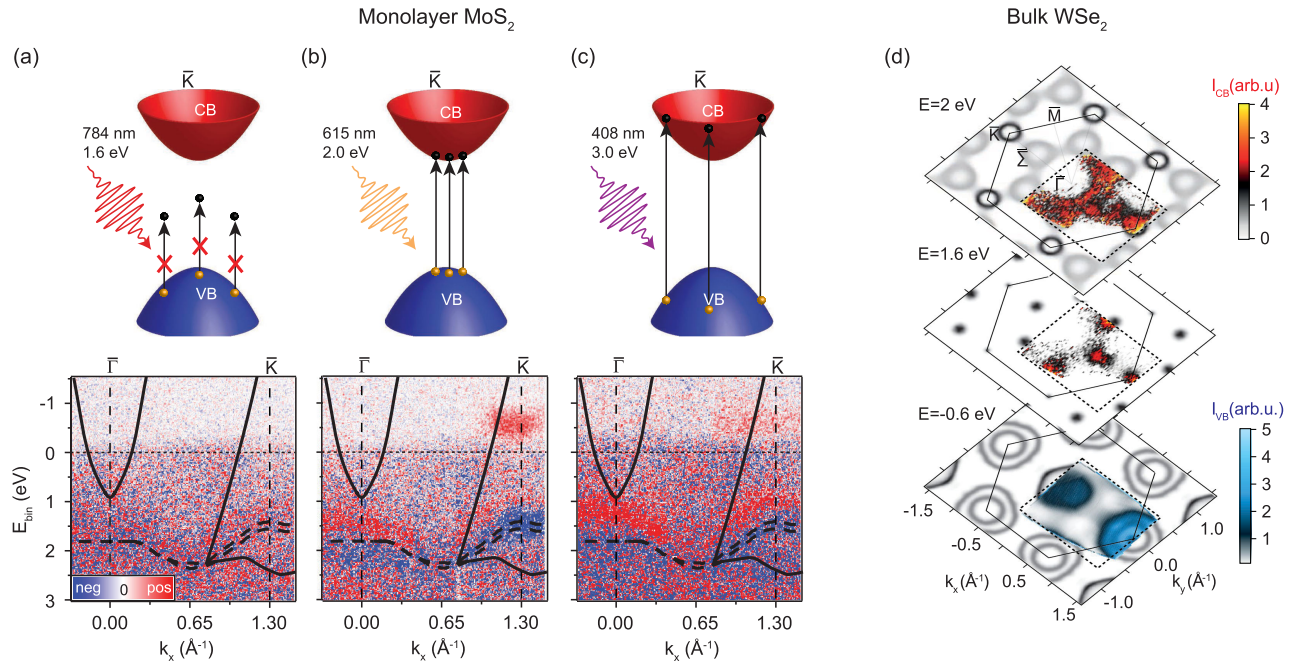
FIG. 11. Mapping of the conduction band of transition-metal dichalcogenides. (a)–(c) Sketches of the available transitions and TR-ARPES differential mapping acquired with 25 eV photons for monolayer MoS_2 around $\bar{K}$ at the peak of the optical excitation using three different pump energies: (a) below the CB onset, (b) resonant to the band gap, and (c) above the CB onset. By tuning the pump photon energy, the value of the direct band gap was estimated at 1.95 eV. The solid lines in (a)–(c) mark the boundaries between the projected bulk band continuum and gaps of Au(111), while the dashed curves represent the equilibrium fitted dispersion. (a)–(c) Adapted from Grubišić Čabo et al., 2015. (d) Photoelectron intensity distribution as a function of parallel momentum for three binding energies at a pump-probe delay of 100 fs acquired for bulk $2H$-WSe_2 with a 21.7 eV probe and a 3.1 eV pump. The higher pump energy allows the CB to be mapped within a wider energy range, which favors a more comprehensive comparison with an *ab initio* calculated band structure. The experimental data are collected in the region delimited by the dashed line; outside this region, the results of calculations are displayed, and the theoretical band dispersion along the k_z direction was integrated. Adapted from Puppin et al., 2022.

TR-ARPES investigations of various monolayer and bulk TMDs have precisely identified their electronic band gap and ultrafast relaxation processes and have also explored the light-induced valley polarization (Grubišić Čabo et al., 2015; Manzoni et al., 2015; Bertoni et al., 2016; Hein et al., 2016; Ulstrup et al., 2016, 2017; Beyer et al., 2019; Wallauer et al., 2020; Lee et al., 2021; Puppin et al., 2022). Grubišić Čabo et al. (2015) focused on light-induced occupation of the CB and subsequent recombination dynamics in monolayer MoS_2 epitaxially grown on Au(111) as a function of the pump photon energy. Figures 11(a)–11(c) display TR-ARPES differential maps computed at the peak of the optical excitation for three distinct excitation energies with respect to the band gap. By fitting the dispersion of the occupied VB and of the light-populated CB, Grubišić Čabo et al. (2015) extracted a 1.95 eV direct band gap, which differs by several hundreds of meV from estimates via equilibrium ARPES upon alkali doping, thus emphasizing how external perturbations may severely impact the electronic properties of monolayer TMDs (Grubišić Čabo et al., 2015). A large transient redistribution of the carriers, as pump excitation may induce, can lead to changes in the screening potential that may significantly renormalize the electronic gap (Andreatta et al., 2019; Liu et al., 2019; Puppin et al., 2022). For instance, Ulstrup et al. (2016) reported a renormalization of the electronic gap as large as ~400 meV in monolayer MoS_2 grown on graphene due to a combination of pump-induced

carrier redistribution and the weak screening in the monolayer MoS_2/graphene heterostructure. Figure 11(d) shows a recent mapping of the occupied VB and unoccupied CB of $2H$-WSe_2 illustrating how TR-ARPES data can be directly compared to the electronic dispersion predicted by *ab initio* calculations (Puppin et al., 2022).

TR-ARPES papers on monolayer TMD/graphene heterostructures have reported an ultrafast and opposite-in-energy band shift of the VB of WS_2 and the π band of graphene (Aeschlimann et al., 2020), as well as charge and energy transfer between WSe_2 and graphene (S. Dong et al., 2023), evidence of a charge-separated transient state with photoexcited electrons and holes located in the TMD and graphene layer, respectively. More recently Majchrzak et al. (2021b) comprehensively characterized the quasiparticle band gap in monolayer and bilayer MoS_2 and WS_2 on different substrates: graphene, Au(111), and Ag(111). They reported a clear influence of the substrate on the electronic gap, as well as on the relaxation dynamics of the photoexcited carriers. In the specific case of bulk MoS_2, Wallauer et al. (2020) showed that the surface exhibits an electronic gap larger than the bottom layers by employing tunable visible excitations across the different gap amplitudes. In particular, by pumping carriers solely into the bottom layer's K points, they observed an interlayer charge transfer into the Σ valley of the topmost layer on a ~20 fs timescale. These papers demonstrate the capability of TR-ARPES both to access the unoccupied
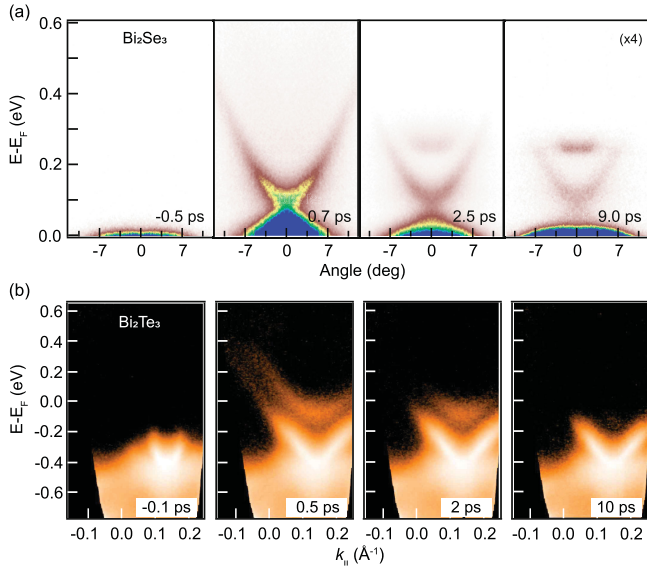
FIG. 12. TR-ARPES mapping of the unoccupied states acquired near the Γ point with ~ 6 eV probe upon a 1.5 eV pump of two topological insulators: (a) Bi_2Se_3 and (b) Bi_2Te_3. The near-IR excitation promotes carriers into the TSS and the CB. Subsequent relaxation processes lead to an accumulation of hot carriers at the bottom of the bulk CB. (a) Adapted from Sobota et al., 2014b. (b) Adapted from Hajlaoui et al., 2012.

band structure in perturbative regimes and to map out-of-equilibrium light-induced renormalizations of the electronic properties of quantum materials.

TR-ARPES studies have also demonstrated the selective population of K/K' valleys in $2H$-WSe$_2$ and single-layer WS$_2$ via dichroic excitation (Bertoni et al., 2016; Ulstrup et al., 2017; Beyer et al., 2019; Volckaert et al., 2019) (see Sec. VII and Fig. 45 for further details), as well as the population of the Σ valley (which is the CB minimum in $2H$-TMDs, also denoted as Δ and Q in the literature) on sub-100-fs timescales (Bertoni et al., 2016; Hein et al., 2016; Wallauer et al., 2016, 2020). This comprehensive momentum-resolved mapping of the out-of-equilibrium redistribution of the electronic population via intraband and interband scattering processes in TMDs further attests to the capability of TR-ARPES to reveal fundamental electrodynamics that remain hidden to other equilibrium and time-resolved techniques.

B. Topological insulators

Three-dimensional topological insulators (TIs) are materials in which the strong spin-orbit interaction leads to the emergence of a metallic topological surface state (TSS) that lies within a bulk gap and has a Dirac-like dispersion with a helical spin structure (Fu, Kane, and Mele, 2007; Hasan and Kane, 2010). An extensive experimental campaign to study TIs via TR-ARPES began in 2012 for both technical and scientific reasons. To begin, since the TSS is commonly centered at Γ in these materials, it is easily accessible to a low-photon-energy source. In addition, the scientific community was interested in evaluating the dispersion of the Dirac cone and bulk bands in the unoccupied states, as well as the intrinsic scattering processes of Dirac electrons with

topological protection. As a result, these compounds served as a highly effective stimulus for commissioning and characterizing the performance of new TR-ARPES systems, thereby significantly advancing this ultrafast spectroscopy technique. Sobota et al. (2012), followed closely by Crepaldi et al. (2012), Hajlaoui et al. (2012), and Wang et al. (2012), first mapped the unoccupied dispersion of the TSS and bulk bands for the prototypical TIs Bi_2Se_3 and Bi_2Te_3. The vanishing of the density of states at the Dirac point, together with the inefficient coupling between the bulk and surface states, leads to relaxation times ranging from a few hundred femtoseconds for unoccupied bulk bands 0.5 eV above E_F to several tens of hundreds of picoseconds for the bottom of the conduction band and TSS; see also Sec. V.A.1. These relatively long decay rates favor the mapping of unoccupied states in TIs. Figure 12 shows the unoccupied band structure of Bi_2Se_3 and Bi_2Te_3 (Hajlaoui et al., 2012; Sobota et al., 2012, 2014b). After the pump photoexcitation from the occupied states (bulk and surface) into the unoccupied bulk bands, the carriers' thermalization is characterized by the accumulation at the bottom of the bulk CB and the slow bulk-to-surface diffusion, leading to delayed (~ 500 fs) transient population of the TSS (Hajlaoui et al., 2012; Sobota et al., 2012; Sánchez-Barriga et al., 2016; Hedayat et al., 2018). In the work of Sobota et al. (2012) on p-doped Bi_2Se_3, a parabolic dispersion is populated before time zero and decays toward negative delays. This feature does not belong to the band structure of Bi_2Se_3 but results from the transient population of the first image potential state, a bound state between an electron in vacuum in front of a metallic surface and the photohole left behind. It is populated by the 6 eV beam and photoemitted by the 1.55 eV pulse (Petek and Ogawa, 1997; Lüth, 2013).

Following these initial studies, the TR-ARPES community has widely applied the technique to probe the unoccupied electronic structure of a variety of TIs (Kanasaki, Tanimura, and Tanimura, 2014; Reimann et al., 2014; Neupane et al., 2015; S. Zhu et al., 2015; Sterzi et al., 2017; Sumida et al., 2017; Hedayat et al., 2018; Xu et al., 2019; Maklar et al., 2022b; Ponzoni et al., 2023). Sobota et al. (2013) employed two-photon photoemission with two 6 eV beams and Niesner et al. (2012) employed circularly polarized optical excitations to reveal the presence of a second topological surface state in the unoccupied bulk electronic gap of Bi_2Se_3 and Bi_2Te_2Se, respectively. Furthermore, the advent of spin-resolved TR-ARPES allowed the intrinsic spin polarization of the unoccupied TSS to be mapped, the evolution of optically induced spin-polarized electronic population to be tracked, and the presence and spin polarization of the surface resonance states to be revealed (Cacho et al., 2015; Jozwiak et al., 2016; Sánchez-Barriga et al., 2016, 2017; Fukushima et al., 2023); see Sec. VII. Kuroda et al. (2016, 2017) and Reimann et al. (2018) showed that the use of mid-IR light (below 0.5 eV) and terahertz radiation can generate ultrafast photocurrents in the TSS. In particular, the seminal work of Reimann et al. (2018) was the first to successfully implement terahertz excitations as the pumping scheme in a TR-ARPES experiment. Figure 13 (top row) shows the ARPES images and the corresponding integrated photoemission intensity for two branches of the Dirac cone (Fig. 13, bottom row) acquired
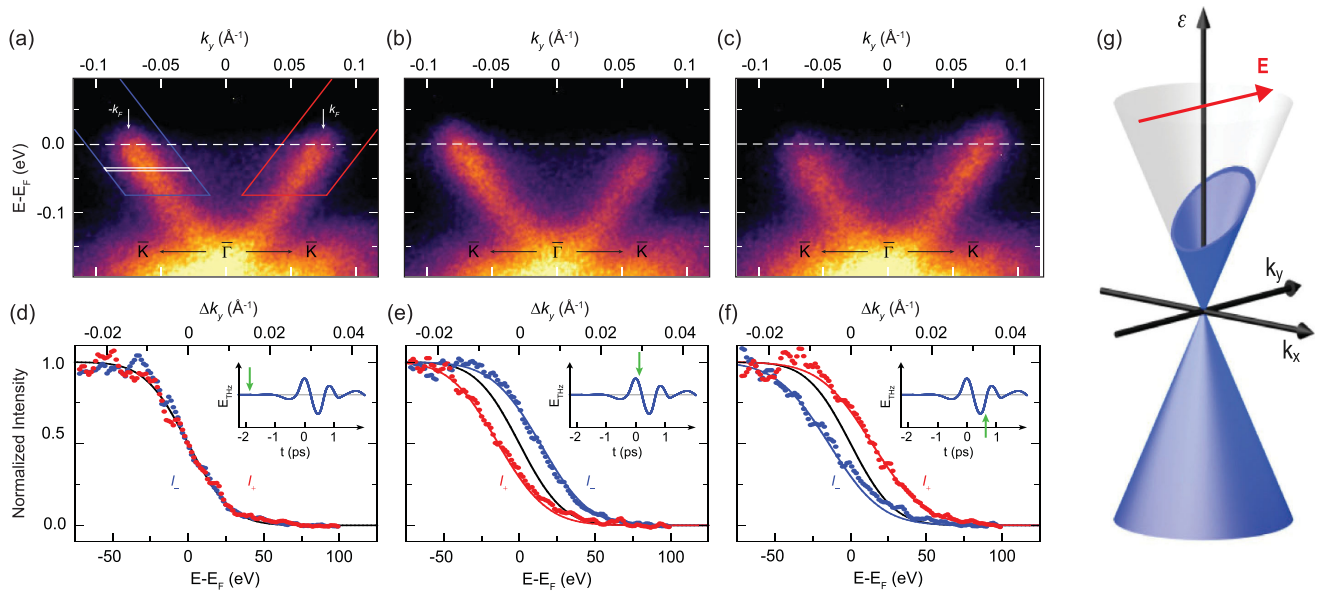
FIG. 13.   Probing the effect of terahertz pump excitation on the topological surface state of Bi_2Te_3 in momentum space. TR-ARPES spectra along ΓK acquired (a) before the teraherz pump, (b) at the electric field node with the largest negative gradient, and (c) at the field node with the largest positive gradient. (d)–(f) Photoemission intensity of the left (blue) and right (red) branches of the Dirac cone integrated inside the blue and red boxes shown in (a)–(c). Red and blue solid lines represent simulations based on the Boltzmann equation, while the black line is the Fermi-Dirac distribution convolved with the experimental resolution. Insets in (d)–(f): illustration of the electric field waveform in which the green arrows mark the time delay of each snapshot. The observed asymmetric population (i.e., a transient momentum shift of the electrons) arising when the electric field is applied indicates the emergence of a transient surface current driven by the ultrashort terahertz pump pulse. (g) Sketch detailing how the acceleration of Dirac fermions in the topological surface state can shift the Fermi surface via an electric field. Adapted from Reimann *et al.*, 2018.

on Bi_2Te_3 at different pump-probe delays after the terahertz streaking of photoemitted electrons was corrected for. These experimental results indicate that the in-plane electric field of the terahertz pulse induces a transient displacement of the Fermi surface dependent on the field's direction, i.e., a transient surface current (Ashcroft and Mermin, 1976). Moreover, by comparing the photoinduced current density at the surface to the terahertz field, Reimann *et al.* (2018) were able to infer that TSS electrons are weakly scattered ($\sim$1 ps as the lower bound). This work demonstrates that the mapping of ARPES spectra with subcycle resolution may provide a new way to track transport processes in complex materials.

Finally, in recent years magnetic TIs have attracted substantial attention because of the coexistence of magnetism and topology (J. Li *et al.*, 2019; Otrokov *et al.*, 2019), which may prompt novel quantum phenomena such as the quantum anomalous Hall effect (Deng *et al.*, 2020). Only a few TR-ARPES papers have explored ultrafast dynamics in magnetic TIs to date, in $MnBi_{2n}Te_{3n+1}$ and $EuSn_2As_2$ (H. Li *et al.*, 2019; Nevola *et al.*, 2020; Zhong *et al.*, 2021; Lee *et al.*, 2023; Majchrzak *et al.*, 2023). Zhong *et al.* (2021) employed TR-ARPES with micrometer resolution to specifically resolve one of the four surface terminations of $MnBi_8Te_{13}$ and reported a long-lasting ($>$10 ns), light-induced filling of the hybridization gap originating from the hybridization between the $MnBi_2Te_4$ septuple layer and the Bi_2Te_3 quintuple layer. This light-induced filling of the hybridization gap was discussed in terms of a transient change of the interlayer coupling due to charge redistribution.

C. Excitons in semiconductors

Excitons are correlated bound states composed of electrons photoexcited in the conduction band and holes left behind in the valence band, and they are commonly observed in semiconductors. Exciton physics is of particular importance in the context of semiconducting 2D TMDs as they dominate their optical properties, thus making the fundamental research of how excitons emerge and interact essential for future applications in optoelectronics and valleytronics (Wang *et al.*, 2018). Exciton physics is commonly explored via all-optical techniques with no momentum resolution, which mainly access bright excitons. These excitons consist of pairs of electrons and holes with the same crystal momentum, and can thus be created via direct optical excitation (for instance, by photoexciting an electron from the VB to the CB at the K point of monolayer TMDs). However, all-optical techniques are commonly (to the first order) blind to excitons with a nonzero total momentum, also known as dark excitons, which are composed of bound electrons and holes located in different valleys in momentum space. For this reason, a time- and momentum-resolved technique able to directly probe dark excitons, as well as to track how and on which timescale photoexcited electrons and holes are bound into excitonic states, has been of great interest.

Excitons have been studied via time-resolved photoemission for the past two decades (Weinelt *et al.*, 2004, 2005), but only in recent years have theoretical studies discussed how TR-ARPES, which accesses the transient evolution of the single-particle band structure (see Sec. II.B), could serve as a

Photoelectron Energy
$E_e(k) = (h\nu-\phi)+E_{ex} - E_h(k)$

Exciton Energy
$E_{ex} = E_g - E_B$

CB

CB

e⁻

E_g

VB

h⁺

Hole Energy
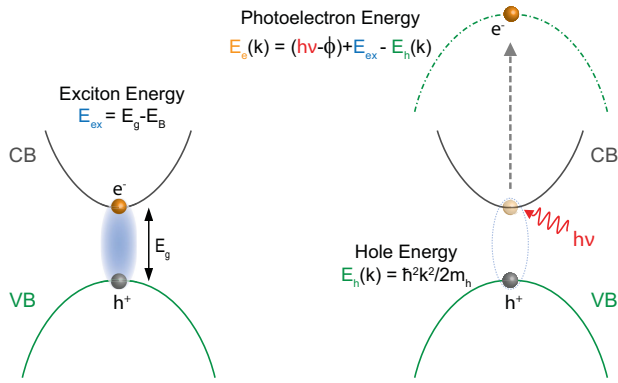$E_h(k) = \hbar^2 k^2/2m_h$

$h\nu$

VB

h⁺

FIG. 14. Schematic illustration of the dispersion of an electron photoemitted from an exciton. Following conservation laws, an electron photoemitted from an excitonic bound state exhibits an energy-momentum dispersion that mimics that of the valence band, with a spectral intensity that diminishes when one moves away from the initial momentum location of the bound state.

probe to study excitons, which are two-fermion quasiparticles (Perfetto *et al.*, 2016; Rustagi and Kemper, 2018; Christiansen *et al.*, 2019). Experimental evidence of excitons in momentum space has been reported in Si(100) (Weinelt *et al.*, 2004, 2005), ZnO (Deinert *et al.*, 2014), Cu_2O (Tanimura, Tanimura, and Van Loosdrecht, 2019) and $ReSe_2$ semiconductors (Volckaert *et al.*, 2023). Following the recent development of momentum microscopes that allow the investigation of micrometer-sized samples, Madéo *et al.* (2020) reported the direct observation in momentum space of bright and dark excitons in monolayer WSe_2. By employing TR-ARPES with micrometer spatial resolution and an optical excitation resonant to the first bright exciton (namely, the *A* exciton at 1.72 eV), Madéo *et al.* (2020) observed an accumulation of intensity ∼400–500 meV below the bottom of the CB developing instantly at the *K* valley, and with a few hundred femtosecond delay at the *Q* valley. The appearance of such transient spectral weight and its position in momentum space are direct signatures of the excitonic state in WSe_2 and allowed them also to extract the ∼400 fs intrinsic timescale associated with the formation of the dark *Q*-valley excitons through scattering from the *K* valley. Using sub-50-fs visible pump pulses, Wallauer *et al.* (2021) subsequently showed that the formation of dark excitons in WS_2 takes place within a few tens of femtoseconds via exciton-phonon scattering of the electron-hole polarization cloud at the *K* points.

The momentum dispersion of the electron photoemitted from the *A* exciton (at *K*) in monolayer WSe_2 was later obtained in follow-up TR-ARPES studies by Dong *et al.* (2021) and Man *et al.* (2021). When an exciton is annihilated through a photoemission process, the dispersion of the previously bound electron mimics the dispersion of the VB, as theoretically predicted (Perfetto *et al.*, 2016; Rustagi and Kemper, 2018; Christiansen *et al.*, 2019) and in agreement with the exciton dispersion reported in Cu_2O (Tanimura, Tanimura, and Van Loosdrecht, 2019). Figure 14 shows how energy and momentum conservation laws determine the dispersion of an electron photoemitted from a bright exciton. In addition, assuming a direct relation between the **k**

dependence of the TR-ARPES spectral weight and the square of the excitonic wave function, Dong *et al.* (2021) and Man *et al.* (2021) computed via Fourier transform an estimate of the spatial extent of the excitonic wave function itself, obtaining a root mean square value of ≈2 nm for the *A* exciton of WSe_2. These studies demonstrated and established how the TR-ARPES technique can map excitons, thus paving the way toward the first observation and estimate of the spatial extent of interlayer excitons (IXLs) in moiré WSe_2/MoS_2 heterostructures (Karni *et al.*, 2022; Schmitt *et al.*, 2022). Figures 9 and 15 show the ARPES mapping of the entire BZ (via momentum microscope) of WSe_2/MoS_2 heterostructures with a twist angle of ∼10° and ∼2°, respectively, highlighting the appearance of a transient spectral weight ∼1 eV above the maximum of the VB. For the ∼2°-twist heterostructure, TR-ARPES maps along the Γ-*K* direction shown in Fig. 15(b) demonstrate the presence of interlayer exciton-bound holes and electrons at the *K* valleys (holes are located at the maximum of the VB, while electrons are bound at 1 eV binding energy) (Karni *et al.*, 2022).

We mention that a TR-ARPES investigation of monolayer MoS_2 showed how excitonic correlations may renormalize the band dispersion of both the CB and the VB. In particular, the simultaneous enhancement of both the band gap and the effective mass may act as a direct probe of excitonic many-body correlations (Lin *et al.*, 2022).

Recently Mori *et al.* (2023) reported evidence of a buildup of intensity below the CB of Bi_2Te_3, as shown in Fig. 16(a). By tracking the transient evolution of the spectral weight below the CB and verifying its spin polarization via spin-resolved TR-ARPES, as well as reporting changes in the topological surface state dispersion, they attributed this intensity buildup to a long-lived spatially indirect spin-polarized exciton in which the photohole resides at the top of the bulk valence band and the electron is in a mixed state between the topological surface state and the CB, thus being somewhat localized at the surface; see Fig. 16(b).

Overall, these recent studies demonstrated the ability of TR-ARPES to access and map the momentum dispersion of excitonic wave functions, as well as to track the excitons' ultrafast formation and interactions. These results open the door to the use of TR-ARPES for investigating many-particle excitations, such as excitons, biexcitons, and trions in TMDs, topological systems, and quantum materials in general.

D. Floquet-Bloch states

Breaking or modifying the underlying symmetries of materials can have noteworthy effects on their electronic properties. In recent years this approach has attracted the interest of the broad scientific community and has led to notable discoveries. Twisted bilayer graphene is an exemplary case (Cao *et al.*, 2018; Cao, Fatemi *et al.*, 2018) in which novel electronic properties emerge from the fine-tuning of its spatial translational symmetry via a moiré pattern. Floquet engineering promises a similar level of control over electronic properties by taking advantage of the temporal periodicity of the electric field of light excitation and can potentially be applied to nearly any material (Oka and Kitamura, 2019; Rudner and Lindner, 2020).
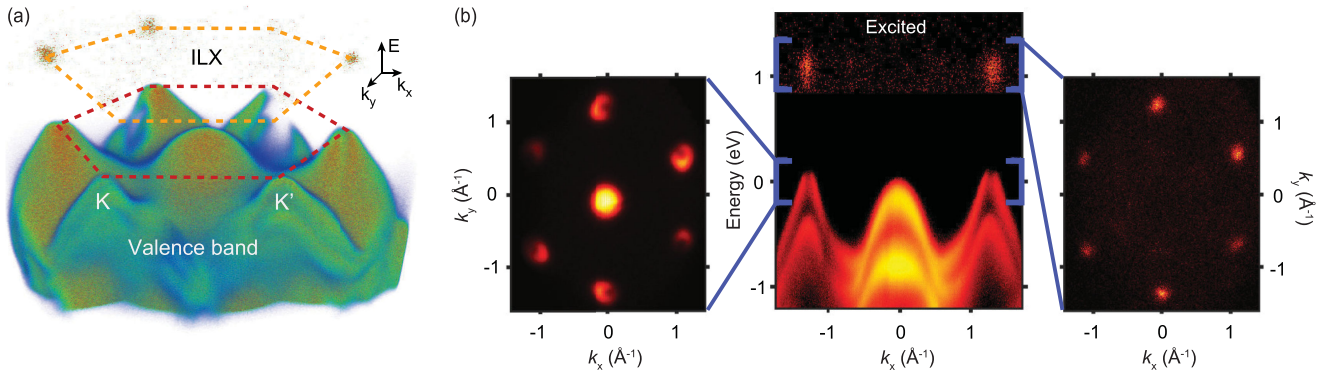
FIG. 15. TR-ARPES employed to map excitons in momentum space. (a) 3D rendering of the TR-ARPES mapping of the occupied and unoccupied band structures of a WSe_2/MoS_2 heterostructure with $\sim 2°$ twist angle and micrometer resolution via momentum microscopy, featuring the presence of an interlayer exciton (ILX) above E_F. (b) TR-ARPES spectrum along the K-Γ direction 25 ps after optical excitation, along with isoenergy maps displaying the momentum location of (left image) the top of the VB and (right image) the top of the ILX. Note the decrease of spectral weight in the VB accompanying the formation of the ILX. These maps were generated by integrating over the energy ranges specified by the blue brackets. Adapted from Karni *et al.*, 2022.

The Floquet theorem, a time analog of the Bloch theorem (Ashcroft and Mermin, 1976), states that when a Hamiltonian $H(\tau) = H(\tau + T)$ is periodic in time, new *quasistatic* energy levels (also known as Floquet levels) emerge with a spacing of $2\pi/T$ (Faisal and Kamiński, 1997). Since Bloch states are intrinsically present in crystalline materials, Floquet states in solids are commonly referred to as Floquet-Bloch states. In principle, Floquet-Bloch states can be driven by any generic time-periodic perturbation. However, at the moment successful experimental investigations of Floquet physics have relied solely on taking advantage of the intrinsic time periodicity of the electric field of light pulses, with emblematic examples in molecules and photonic crystals (Bandrauk and Sink, 1981; Rechtsman *et al.*, 2013). In solids, the crossing of Floquet-Bloch replicas with original bands may lead to hybridization and the opening of electronic gaps, thus effectively engineering the systems' electronic properties. Figure 17 illustrates the emergence and temporal evolution of such nonequilibrium states induced by an optical excitation in a topological insulator.

Wang *et al.* (2013) first reported the appearance of Floquet-Bloch states in Bi_2Se_3 with energy and momentum resolution. As a function of the polarization of the impinging mid-IR field, energy gaps may or may not open along different momentum directions (Oka and Aoki, 2009; Zhou and Wu, 2011). In the case of Bi_2Se_3, a linearly polarized mid-IR excitation prompts a gap opening only along the k_y direction. In contrast, the use of circularly polarized light with photon energy comparable with the bulk energy gap breaks the intrinsic time-reversal symmetry of the system and opens a full gap at the Dirac point, as well as Floquet-Bloch hybridization gaps along all momentum directions (Wang *et al.*, 2013).

Although both Floquet physics and the laser-assisted photoemission (LAPE) phenomenon[2] (Saathoff *et al.*, 2008)

lead to the appearance of replica bands along the energy direction, they originate from different physics. Light-induced Floquet-Bloch states emerge from the dressing of a bound electron inside the solid by a photon, whereas LAPE describes the photon dressing of a free electron outside the solid and results in Volkov states (Mahmood *et al.*, 2016). Therefore, band hybridization and consequent gapping of the electronic band structure can originate only from Floquet-Bloch states, not from Volkov states. The different contributions to the light-induced band replicas observed in ARPES images arising from Floquet-Bloch and Volkov states can be distinguished via a careful assessment of the intensity and gapping of the light-induced replicas as a function of the momentum direction and polarization of the driving light pulse; see Fig. 8 (Mahmood *et al.*, 2016; Schüler and Beaulieu, 2022).

A recent TR-ARPES work offered further insights into the subcycle formation of Floquet-Bloch replicas (Ito *et al.*, 2023). Using probe pulses with a temporal duration shorter than the optical cycle of the mid-IR driving pulse [see Fig. 18(a)], they reported the emergence of Floquet-Bloch replica bands in Bi_2Te_3 within a single optical cycle of the driving mid-IR pulse. Figure 18(c) shows how intraband currents fill the Floquet sidebands at opposite momenta that depend on the orientation of the driving electric field until interband electron scattering destroys the Floquet bands (Ito *et al.*, 2023).

In systems other than TIs, Reutzel *et al.* (2020) and Aeschlimann *et al.* (2021) successfully observed Floquet-Bloch replica via four-photon photoemission and TR-ARPES in $Cu(111)$ and WSe_2, respectively. While evidence of Floquet engineering in exfoliated graphene has been reported in a time-resolved transport experiment (McIver *et al.*, 2020), subsequent TR-ARPES exploration of the effects of strong mid-IR excitation on graphene did not result in any gap opening observations. Instead, Aeschlimann *et al.* (2021) observed a pronounced broadening of the spectral features, which they attributed to efficient decoherence scattering, pointing out the possible practical limitations of Floquet engineering for systems with intrinsically short scattering times; see Sec. V.A.

Recently Zhou *et al.* (2023) provided the first demonstration of Floquet engineering of the electronic band structure of
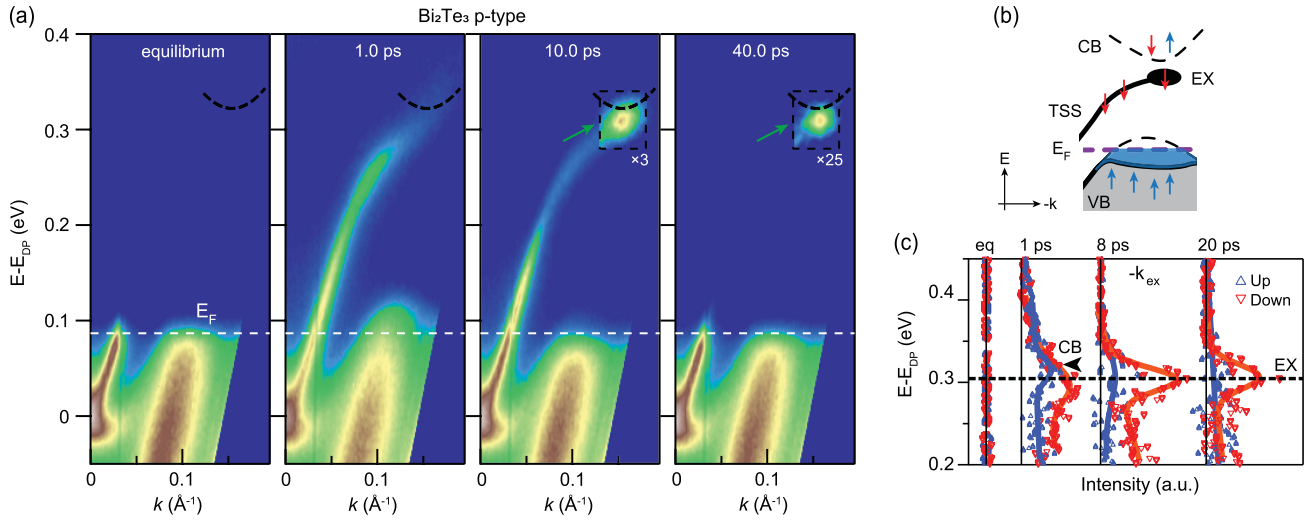
---

[2]LAPE is commonly used to find the zero pump-probe delay of TR-ARPES systems and characterize their temporal resolution (Eich *et al.*, 2014). Operationally, LAPE appears only when the pump electric field has an out-of-plane component relative to the sample surface.

FIG. 16. Spatially indirect excitons in 3D topological insulators. (a) TR-ARPES spectra along Γ-M of p-doped Bi_2Te_3 at equilibrium and three different pump-probe delays. The energy scale refers to the position of the Dirac point in energy. (b) Sketch of the experimental observation highlighting the spin polarization and formation of the excitonic state in the intensity buildup and the topological surface state. (c) Spin-resolved spectra of the exciton intensity buildup at the exciton momentum k_{EX}, measured at a delay time of 20 ps. Adapted from Mori *et al.*, 2023.

black phosphorus. Figure 19 displays the hybridization of the valence band with the first Floquet replica of the conduction band as a function of the mid-IR photon energy. By varying the photon energy of the driving field, the Floquet-driven hybridization gap moves across the valence band, effectively tuning the position in the energy of the light-induced electronic band gap; see Fig. 19(c) (note that these data also suggest a possible band inversion between the valence band and conduction band edges by increasing the pump photon energy). Overall, the recent work of Ito *et al.* (2023) and Zhou *et al.* (2023) established Floquet engineering as a promising approach to control the electronic properties of quantum materials, even when non-negligible dissipation processes are present.

E. Summary and outlook

TR-ARPES has become the preferred technique for mapping the momentum dispersion of unoccupied states, such as the conduction band of semiconductors or the topological surface state of 3D topological insulators, as well as for observing the emergence of electronic states with no equilibrium counterpart, such as excitons in TMDs and TIs or Floquet-Bloch states. Although we have not comprehensively reviewed all of the many different systems in which TR-ARPES offers direct access to unoccupied or transient states [for example, Dirac semimetals (Gatti *et al.*, 2020; Bao *et al.*, 2022) and transition-metal pentatellurides (Manzoni *et al.*, 2015; Zhu *et al.*, 2022), as well as graphene (Gierz *et al.*, 2013) and charge-ordered systems (Hellmann *et al.*, 2012a; Nicholson *et al.*, 2018; J. Dong *et al.*, 2023a)], note that the process of mapping unoccupied or transient states often also characterizes the intrinsic thermalization timescales of electrons photoinjected into these states. In this regard, although insufficient energy resolution can sometimes limit the observation of unoccupied states, electron dynamics can

nonetheless provide indirect evidence for the dispersion or gapping of the unoccupied states; see Crepaldi *et al.* (2017).

In addition, in Sec. III.A.2 we discussed light-induced band gap renormalizations in TMDs. Other types of ultrafast modifications of electronic gaps are broadly found in TR-ARPES investigations of quantum materials, and they are often related to the transient modification of the screening following changes in electron correlations (i.e., a U/W ratio, where U is the on-site interaction and W is the electronic bandwidth) (Tancogne-Dejean, Sentef, and Rubio, 2018;
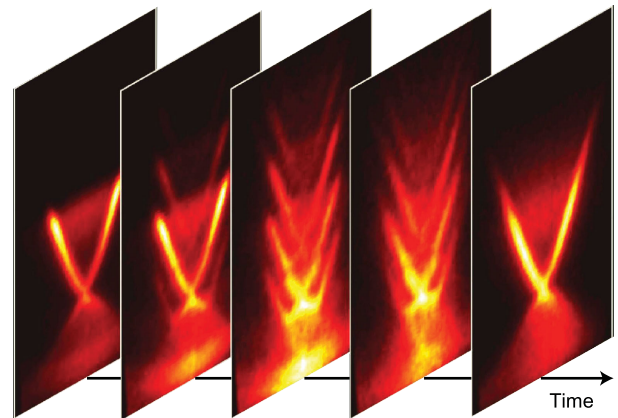

FIG. 17. Emergence of Floquet-Bloch states on the surface of Bi_2Se_3 driven by a 160 meV, 300 fs light pulse. The coherent interaction between the time-periodic potential of the light pulse and the electrons in the Dirac cone results in Floquet-Bloch states that appear to be replicas in energy of the original Dirac cone. Dynamical gaps in the electronic structure open up at positions where the replica cones intersect with the original cone. The replica bands disappear once the driving field dies off. Adapted from Gedik and Vishik, 2017, and Mahmood *et al.*, 2016.
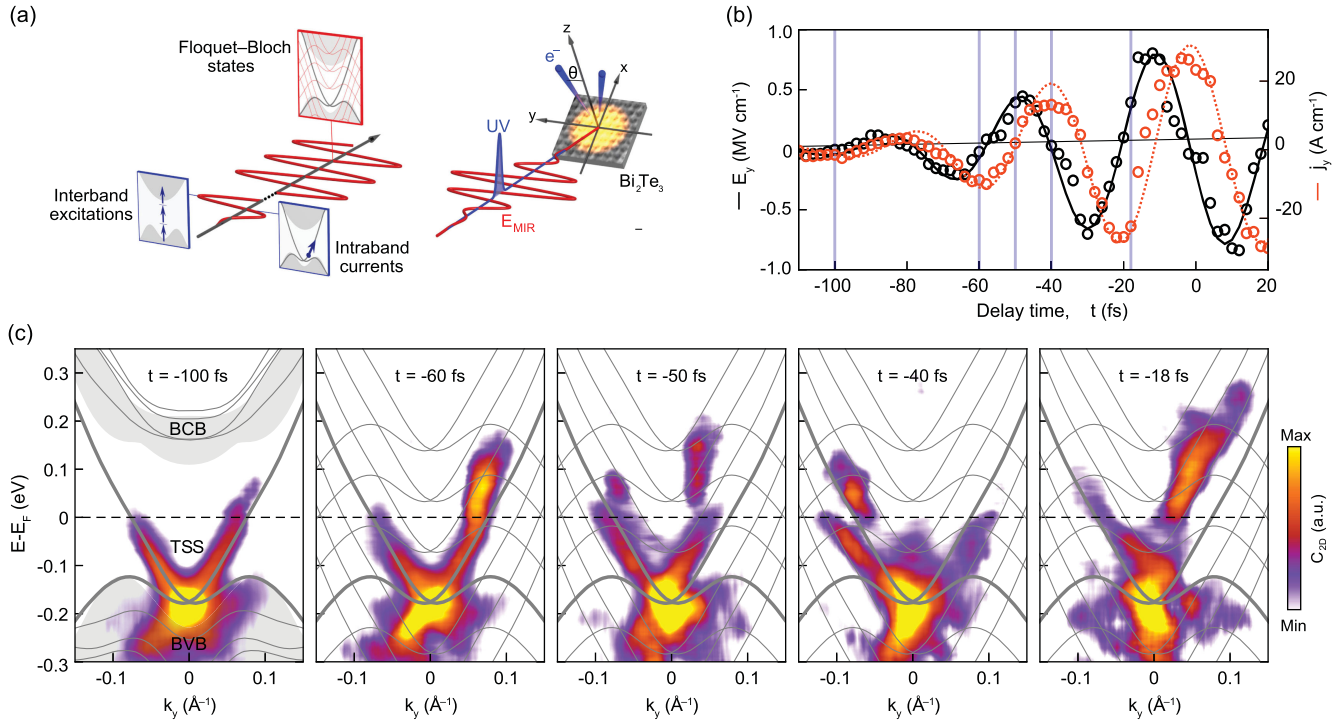
FIG. 18. Floquet-Bloch states on subcycle timescales in Bi_2Te_3. (a) Left graphic: illustration of electronic processes driven via mid-IR excitation, such as multiphoton interband excitation and intraband currents, which may also result in the emergence of Floquet-Bloch states. Right graphic: schematic experimental strategy to investigate the emergence of Floquet-Bloch states on subcycle timescales. (b) Electric field waveform from mid-IR-induced momentum streaking (black markers) and current density (red markers). The black solid line shows the analytic function of the electric field with a peak amplitude of 0.8 MV/cm, while the dashed red line is the electric current induced by this electric field according to the Boltzmann model (Reimann et al., 2018). (c) Curvature-filtered TR-ARPES maps recorded at different pump-probe delays during the first half of the mid-IR driving pulse. The gray lines display the band structure calculated using density functional theory (DFT). The electronic distribution splits into multiple branches that follow the Floquet-Bloch replicas of the TSS. Adapted from Ito et al., 2023.

Gatti et al., 2020; Nilforoushan et al., 2020; Beaulieu et al., 2021; Bao et al., 2023).

In all of the systems discussed in this section, electron scattering processes are slow enough to allow one to map unoccupied and transient states. When strong electron correlations are present (and thermalization times are considerably faster than the temporal resolution), accessing unoccupied states could be challenging. However, information on the unoccupied states and their dispersion can be inferred by tracking light-induced renormalizations of the electronic dispersion, as demonstrated in Bi-based cuprate superconductors where transient shifts of the chemical potential have been discussed in terms of the particle-hole asymmetry of the pseudogap (Miller et al., 2017) and transient shifts of the Fermi momentum have been attributed to the presence of small nodal pockets (Freutel et al., 2019).

Over the next few years, we foresee improved capabilities to map unoccupied and transient states via TR-ARPES owing to technical advances in the detection of photoelectrons (i.e., new detectors with lower dark counts and higher dynamical ranges), as well as the development of ultrastable XUV or UV and pump pulses. Furthermore, recent advances in time-resolved momentum microscopes, which record 3D datasets $I(k_x, k_y, \omega)$ as a function of the pump-probe delay τ without the need to scan across the sample, have opened a pathway

toward mapping the occupied or unoccupied electronic band structure of solids over a large momentum region and with spatial resolution of the order of a few micrometers (Krömker et al., 2008; Schönhense, Medjanik, and Elmers, 2015; Tusche et al., 2016; Jansen et al., 2020; Keunecke et al., 2020; Xian et al., 2020; Neef et al., 2023; Ponzoni et al., 2023). These technical advances may allow investigating Floquet engineering on moiré patterned systems, an approach that promises precise control on the electronic and topological properties of matter (Topp et al., 2019, 2021; Rodriguez-Vega, Vogl, and Fiete, 2021).

In addition to mapping of electronic dispersion, we also expect to see an increase in the number of studies applying state-of-the-art analysis of the out-of-equilibrium ARPES spectral features in order to disentangle population and many-body effects. Only in this way will the TR-ARPES community be able to access light-driven electronic states in a robust fashion, thus providing a pathway toward the optimized mapping and control of out-of-equilibrium phases of quantum materials.

IV. PHOTOINDUCED PHASE TRANSITIONS

The study of phase transitions in condensed matter is of pivotal interest for the entire scientific community not only on
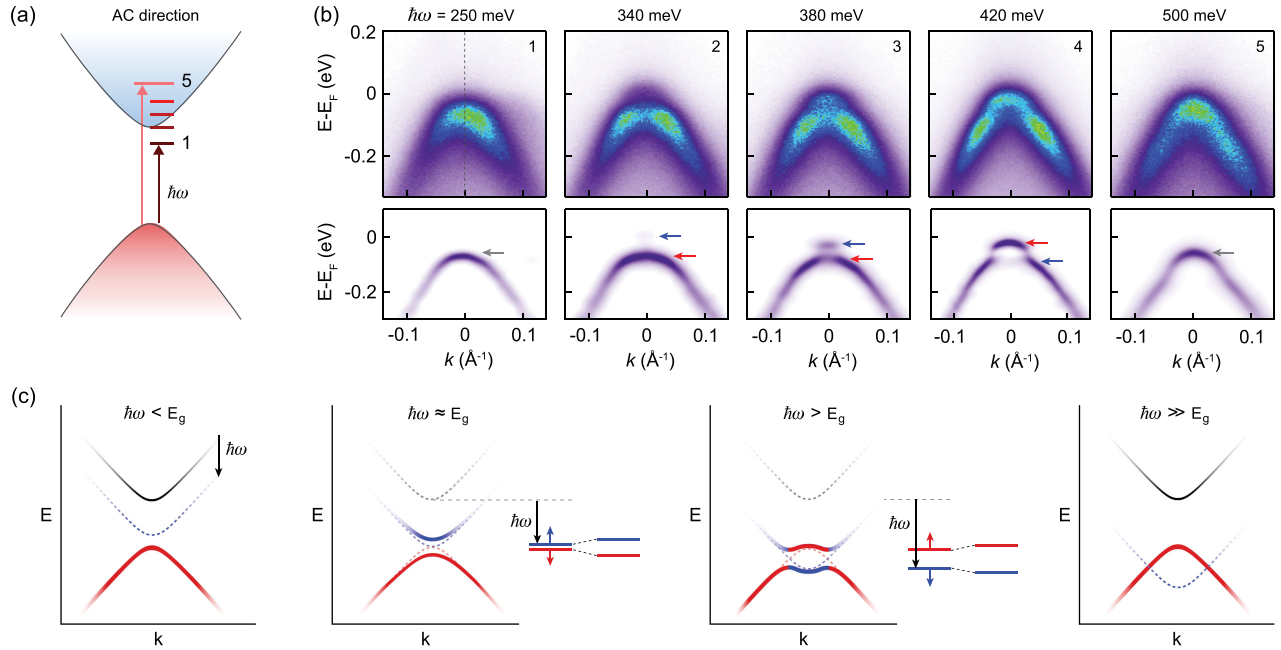
FIG. 19. Floquet engineering of black phosphorus. (a) Schematic of the band structure of semiconducting black phosphorus (with an electronic gap $E_g \sim 340$ meV) with the different mid-IR photon energies used. (b) TR-ARPES maps at zero pump-probe delay (top row) and corresponding second-derivative images (bottom row) for different excitation energies. (c) Sketch of the light-induced modifications of the electronic band structure for four different pump photon energies: below the gap, comparable to the gap, slightly above the gap, and above the gap. Adapted from Zhou *et al.*, 2023.

a fundamental level but also as a source of future technological advances. A frequent complication encountered when one attempts to model and understand phase transitions in complex materials is the involvement of several intertwined degrees of freedom, often occurring on the same energy scale. Moreover, with respect to second-order phase transitions, the development of long-range order may be anticipated by dynamical short-range precursors, making the identification of the energetic hierarchy challenging. By directly accessing the time domain, time-resolved spectroscopies can unveil the dynamical nature of all degrees of freedom participating in the phase transition, thus disentangling their individual contributions (Giannetti *et al.*, 2016). Capitalizing on its momentum and energy resolutions, TR-ARPES can track the dynamical behavior of specific electronic states and energy gaps and correlate them to the transient evolution of carriers or collective modes, enormously aiding the interpretation of time-resolved signals in comparison to all-optical probes.

This section discusses a few representative cases in which TR-ARPES has offered invaluable insights into equilibrium and dynamical light-induced phase transitions. Section IV.A starts by reviewing TR-ARPES studies on the ultrafast melting of long-range charge order in tritellurides and transition-metal dichalcogenides. Section IV.B presents experimental evidence of metal-to-insulator transitions on subpicosecond timescales, followed by a discussion of how light excitations may melt or enhance excitonic condensates in Sec. IV.C. Finally, Sec. IV.D concludes by addressing the ultrafast response of the superconducting condensate, with a specific focus on the dynamical evolution of the superconducting gap of Bi-based cuprate high-temperature superconductors.

A. Melting of charge order

Charge order (CO), or alternatively charge density waves (CDWs), is the phase of matter in which the charge density self-reorganizes with a spatial periodicity that differs from that of the underlying lattice (either commensurate or incommensurate). CO or CDWs are a recurrent feature of numerous quantum materials and may originate from a variety of microscopic mechanisms, microscopic mechanisms, such as Fermi-surface nesting, Peierls instability (or, generally, electron-phonon coupling), and strong electron-electron interactions (Comin and Damascelli, 2016). Although the terms CO and CDWs typically refer to slightly different phenomenology (weak and strong involvement of the lattice, respectively), the following discussion refers to the entire phenomenology as CO. Common manifestations of CO include softening of phonons at the CO wave vector (i.e., the Kohn anomaly) and, in the case of long-range CO, the folding of electronic bands and opening of a gap at the crossing points between the original and folded bands (X. Zhu *et al.*, 2015). The amplitude of such a spectroscopic gap reflects the interaction strength underlying the CO itself. However, given the inevitable intertwining between lattice and electronic degrees of freedom in solids, there has historically been a question of causality as to whether electron-phonon or electron-electron interactions are the main driving force of charge instabilities.

TR-ARPES has been instrumental in addressing this question in CO systems by tracking the transient evolution of the in-gap spectral weight and the appearance or disappearance of CO-folded bands, as well as by extracting valuable dynamical information of collective phenomena, such as the CO
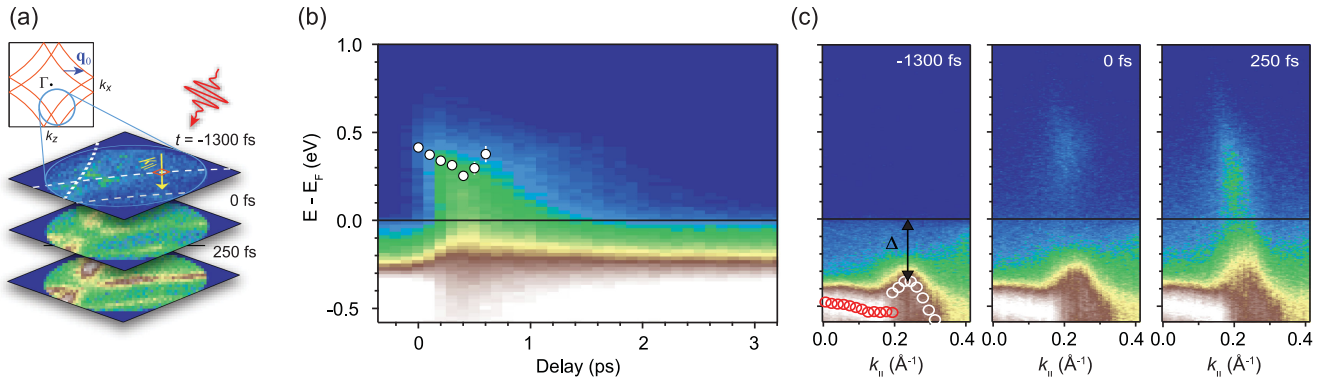
FIG. 20. Ultrafast melting of the CO phase upon near-IR pumping in $LaTe_3$. (a) Top illustration: tight-binding plot of the normal-state Fermi surface of $LaTe_3$ formed by the Te p bands in the first BZ. The circle highlights the probed part of the Fermi surface and the arrow marks the CO wave vector $\mathbf{q}_0$. Bottom illustration: Fermi surface maps at different pump-probe delays across the photoinduced phase transition. The CO gap present before the pump arrival closes on a timescale of $\sim$100 fs, whereas a full recovery of the long-range CO phase occurs only after $\sim$5.5 ps. (b) Detailed time evolution of the gapped region highlighted by the orange box drawn in the $t = -1300$ fs slice in (a). The white dots mark the fitted positions of the upper CO band edge. (c) Time evolution of the band structure near the Fermi level after photoexcitation acquired along the $k_\parallel$ direction highlighted in (a) by the yellow line. Adapted from Zong *et al.*, 2019b.

amplitude mode. Rare-earth tritellurides (RTe_3, with R indicating a rare-earth element) are a model system for investigating the CO phenomenology driven by Fermi-surface nesting. Figure 20 offers an emblematic example of TR-ARPES data on $LaTe_3$ (Zong *et al.*, 2019b), where the Fermi surface is folded by the CO wave vector $\mathbf{q}_0$. A near-IR pump excitation of tritellurides results in the following two main observations (Schmitt *et al.*, 2008, 2011; Rettig *et al.*, 2016; Zong *et al.*, 2019a, 2019b; Maklar *et al.*, 2021, 2022a): (i) coherent oscillations of electronic bands and (ii) the suppression or filling of the CO gap [Fig. 20(c)]. In particular, while coherent oscillations of the electronic band structure may reflect specific phonon modes launched by impulsive or displacive resonant optical excitation (see Sec. V.B), the pump-induced 2.3 THz mode is observed solely in momentum regions near the CO gap and disappears at high excitation fluences or above the CO onset temperature (T_{CO}). As a result of these observations, Schmitt *et al.* (2008) interpreted the 2.3 THz mode as the CO amplitude mode. As for the dynamical evolution of the in-gap spectral weight, the ultrafast melting of the CO phase does not occur instantaneously upon pump excitation but instead develops on a timescale of $\sim$100 fs, indicating the key role of the lattice in stabilizing the CO phase. Moreover, while the gap amplitude recovers within 1 ps, the long-range coherence of the CO phase is reestablished only after $\sim$5.5 ps. Zong *et al.* (2019b) proposed that this long timescale arises as a consequence of the optical generation of topological defects in the CO-ordered phase.

TMDs such as $1T$-TaS_2 and $1T$-$TiSe_2$ are another class of CO materials that have been investigated extensively via TR-ARPES (Rohwer *et al.*, 2011; Hellmann *et al.*, 2012a; Mathias *et al.*, 2016; Monney *et al.*, 2016; Majchrzak *et al.*, 2021a; Y. Zhang *et al.*, 2022; J. Dong *et al.*, 2023b; Sayers *et al.*, 2023). Strong electron interactions in $1T$-TMDs may prompt the emergence of Mott localization and excitonic insulator physics, thus challenging the study of the microscopic origin of the CO phase. The contribution of TR-ARPES is to look for dynamical signatures of the CO phase in specific momentum regions, distinguishing among the different energetic contributions (Sohrt *et al.*, 2014). This role is exemplified in the study of the CO in $1T$-$TiSe_2$. While the ultrafast evolution of the spectral weight at the zone center Γ does not directly characterize the CO phase, due to the interplay of other degrees of freedom (Perfetti *et al.*, 2006, 2008; Hellmann *et al.*, 2012a; Hedayat *et al.*, 2019), the transient disappearance of the CO-folded bands at the M point instead serves as a clear signature of the light-induced melting of the CO phase (Petersen *et al.*, 2011; Rohwer *et al.*, 2011; Hellmann *et al.*, 2012a; Rohde *et al.*, 2014; Mathias *et al.*, 2016; Monney *et al.*, 2016; Huber *et al.*, 2022). Hellmann *et al.* (2012a) explored the transient response of the CO in several TMDs, as shown in Fig. 21. Pristine $1T$-TaS_2 shows a sub-50-fs melting of the Mott gap at Γ and an $\sim$225 fs response of the CO gap at the M point, with the subsequent observation of a CO amplitude mode. The CO gap melts in approximately half the period of the CO amplitude mode, supporting a structural origin for the CO in $1T$-TaS_2, although the presence of purely electronic contributions has also been discussed (Hellmann *et al.*, 2010; Ishizaka *et al.*, 2011; Petersen *et al.*, 2011).

Long-range CO has also been observed in *in situ* Rb intercalated $1T$-TaS_2 (Rb : $1T$-TaS_2), with a large energy gap of 400 meV around the BZ center. Although both the amplitude and the period of the oscillations are smaller than in the pristine case, the temporal evolution of the order parameter in Rb : $1T$-TaS_2 exhibits the same fingerprint of Peierls physics, with a gap melting time of 125 fs, corresponding to half an oscillation cycle of the amplitude mode. In contrast, optical melting of CO in $1T$-$TiSe_2$ takes place on a timescale of 30–80 fs, depending on the excitation fluence (Rohwer *et al.*, 2011; Mathias *et al.*, 2016). This time constant is too fast for a structural transition, and at the same time slower than the conventional electron-hopping timescale (Hellmann *et al.*, 2012a). The relation between the melting of the CO gap and
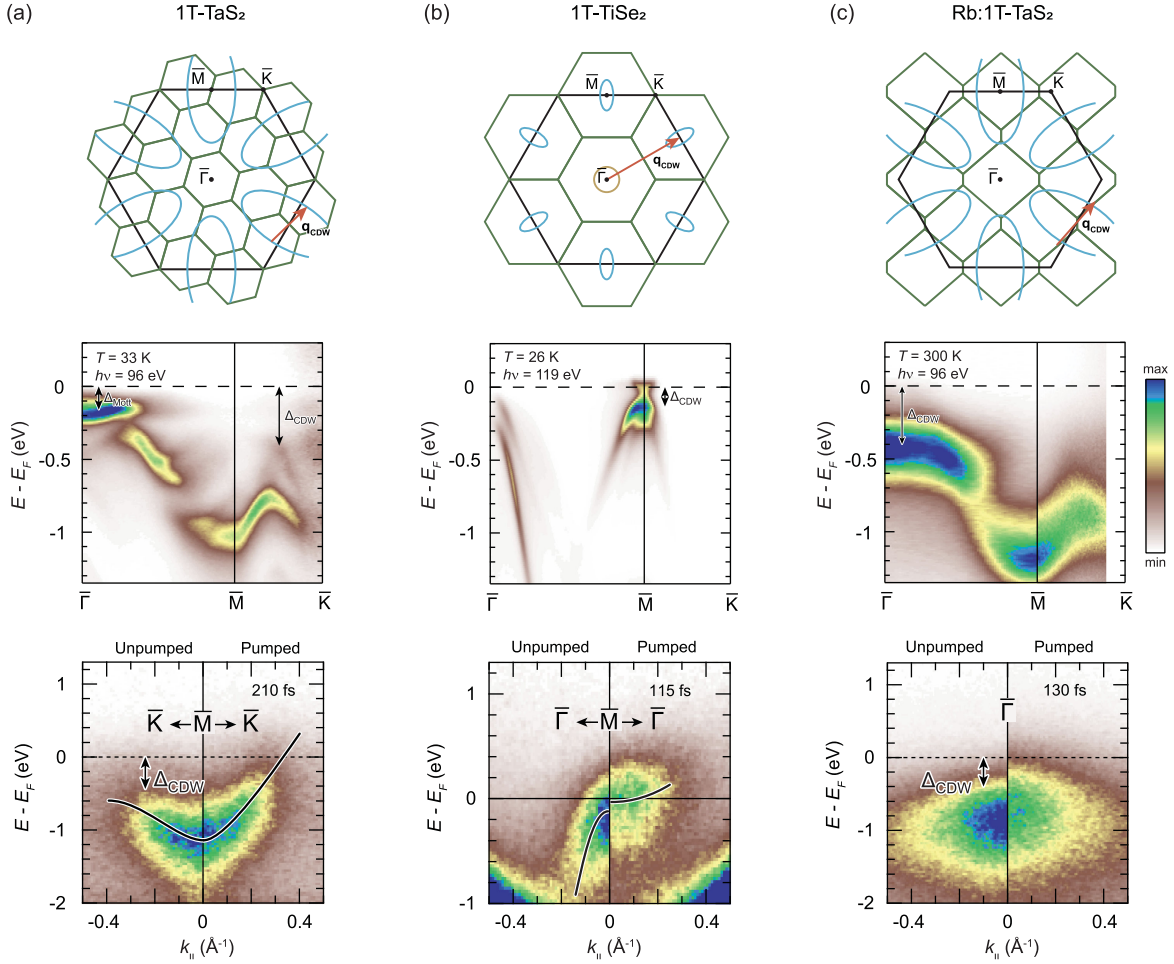
FIG. 21. TR-ARPES spectroscopic signatures of the light-induced melting of the CO in various layered transition-metal dichalcogenides. Top row: illustration of the reconstructed (green lines) and original (black lines) projected Brillouin zones of three CO phases in $1T$-TMDs: (a) TaS$_2$, (b) $1T$-TiSe$_2$, and (c) Rb:$1T$-TaS$_2$. The original schematic Fermi surfaces (circle and ellipses) are shown along with CO wave vectors (arrows). Middle row: static ARPES dispersion of the three compounds highlighting the different characteristic energy gaps in the Brillouin zone. Bottom row: unpumped and pumped TR-ARPES spectra acquired at (a) the $\bar{M}$ point of $1T$-TaS$_2$, (b) the $\bar{M}$ point of $1T$-TiSe$_2$, and (c) the $\bar{\Gamma}$ point of Rb: $1T$-TaS$_2$. The absorbed pump energy density and temperature were set to 300 J cm^{-3} and 110 K, respectively. Adapted from Hellmann et al., 2012a.

the density of transient free carriers is incompatible with a pure Peierls scenario, and it has been discussed in terms of a transient enhancement of the screening (Rohwer et al., 2011; Rohde et al., 2014; Monney et al., 2016), which is in agreement with the presence of an underlying excitonic condensate (see Sec. IV.C), although we note that these fast electron dynamics might be related to the metallic nature of $1T$-TiSe$_2$ even at low temperature. However, a recent multitechnique study combining TR-ARPES and time-resolved reflectivity showed that electron-phonon coupling contributes to the stabilization of the CO phase and the exitonic condensate in 1T-TiSe$_2$ (Hedayat et al., 2019).

TR-ARPES has both offered invaluable insights into the dynamical properties of CO in various systems and established how light-matter interactions can drive transient and metastable states unachievable in equilibrium conditions (Shi et al., 2019; Zong et al., 2019b; Duan et al., 2021; Maklar et al., 2021, 2023; Y. Zhang et al., 2022; Azouri et al., 2023). As a paradigmatic example, TR-ARPES data corroborated by MeV ultrafast electron diffraction measurements have

revealed a transient metastable 2D-ordered electronic state at the surface of 1T-TiSe$_2$ (Duan et al., 2021, 2023). As shown in Fig. 22(b), analysis of the transient evolution of the spectral features has identified an ultrafast modification of the electronic dispersion at the Γ point upon near-IR excitation [Fig. 22(a) displays the 3D BZ], as well as a counterintuitive sharpening of the ARPES line shape for certain excitation fluences. The transient modification of the electronic dispersion and sharpening of the ARPES spectral features have been interpreted as evidence of the optically induced inversion of the 3D CO phase at the surface of 1T-TiSe$_2$ [Fig. 22(c)], and a consequent formation of long-range 2D domain walls, realizing a new metastable phase of matter (Duan et al., 2021).

Finally, Crepaldi et al. (2022) studied the quasi-1D Weyl semimetal (TaSe$_4$)$_2$I, in which the emergence of CO is thought to open electronic gaps at the Weyl points, leading to the formation of an axionic insulator phase. They took advantage of the light-induced filling of the CO gap to restore the Weyl phase in (TaSe$_4$)$_2$I and explore the dynamical
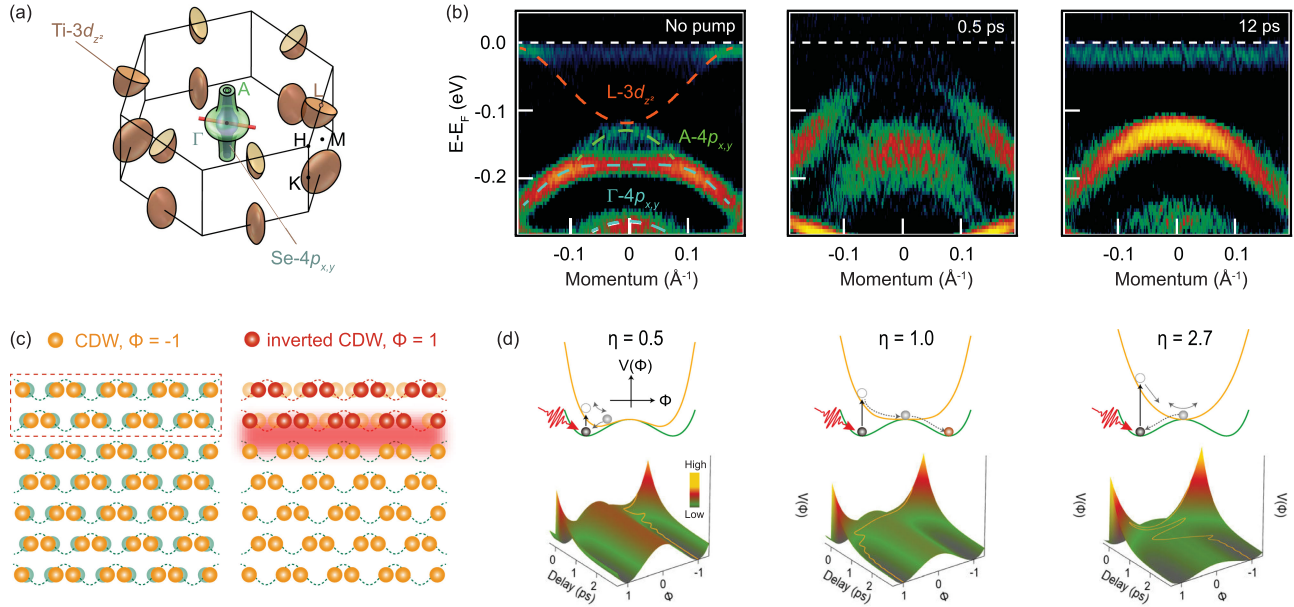
FIG. 22. Light-induced 2D metastable electronic state at the surface of $1T$-TiSe$_2$. (a) 3D BZ of $1T$-TiSe$_2$. (b) Second-derivative ARPES spectra of the time-dependent electronic structure of $1T$-TiSe$_2$ acquired along the Γ-M direction at 4 K [the red line in (a)]. The dashed blue, green, and red lines mark the dispersion of the Se $4p_{x,y}$ band at Γ, the Se $4p_{x,y}$ band folded from point A, and the Ti $3d_{z^2}$ band folded from point L, respectively. A clear ultrafast modification of the electronic dispersion is observed, with a recovery dynamics of tens of picoseconds. (c) Schematic of the CO inversion mechanism in real space. Left graphic: The original 3D CO lattice has an order parameter $\phi = -1$. Right graphic: Upon photon excitation, phase inversion occurs at the surface leading to an order parameter $\phi = +1$. As a result, quasi-2D electronic states form between the inverted and original CO layers (red shaded area). (a)–(c) Adapted from Duan *et al.*, 2021. (d) Time-dependent Ginzburg-Landau model as a function of the order parameter for three selected pump fluences: schematics of the energy potential before and after photoexcitation (top row) and calculated transient energy potential (bottom row). Adapted from Duan *et al.*, 2023.

crossover between the Weyl semimetal state and the postulated axionic insulator phase.

B. Metal-to-insulator transitions

The Mott insulating phase is one of the fundamental phases that can give rise to strongly correlated materials: it emerges when the Coulomb repulsion between electrons overcomes their kinetic energy, leading to the localization of charge carriers and the development of a Mott band gap between the lower Hubbard band (LHB) and the upper Hubbard band (UHB). However, as illustrated in Sec. IV.A, electron-electron interactions may also prompt the emergence of other quantum phases of matter, such as charge order. Therefore, although the Mott insulating phase is driven purely by electron-electron interactions, the transition into or out of such a state may be accompanied by a charge or structural reorganization, thus calling for investigative tools capable of distinguishing among the different contributions (competing or coexisting) to the phase transition. While photoinduced metal-to-insulator transitions (MITs) have been reported by optical and transport studies (Rini *et al.*, 2007; Morrison *et al.*, 2014), TR-ARPES provides a direct probe of the temporal modifications of the electronic structure in momentum space upon the breakdown of the insulating phase and can both track the transient renormalization and collapse of the electronic Mott gap and disentangle the different degrees of freedom involved in the transition in the time domain.

TMDs have been extensively investigated by TR-ARPES to explore their MITs (Perfetti *et al.*, 2006, 2008; Hellmann *et al.*, 2012a; Ligges *et al.*, 2018; Biswas *et al.*, 2021) and other ultrafast techniques, with the exemplary report of a light-induced metastable hidden phase in $1T$-TaS$_2$ (Stojchevska *et al.*, 2014; Stahl *et al.*, 2020; Maklar *et al.*, 2023). Early TR-ARPES studies of $1T$-TaS$_2$ showed that an ultrashort near-IR pump excitation leads to a nearly instantaneous melting of the Mott insulating state at the Γ point as the spectral weight is transferred from the LHB to the originally gapped region at the Fermi level [Figs. 23(a)–23(c)]. The initial fully insulating state is then restored on a subpicosecond timescale, as shown by the temporal evolution of the LHB peak intensity in Fig. 23(b). In addition to this substantial transfer of spectral weight, coherent oscillations corresponding to the CO amplitude mode have also been detected modulating the electrons' binding energy in the TR-ARPES spectra; see also Secs. IV.A and V.B. The different relaxation time and pump-fluence dependence allows the dynamics of the electronic and lattice subsystems to be disentangled. While the photoinduced ionic displacement increases linearly with the employed pump fluence, the change in the LHB intensity does not, and the periodic oscillations persist for >20 ps without affecting the Mott insulating state recovered within 1 ps (Perfetti *et al.*, 2006, 2008).

These results indicate the primary role played by the electronic degrees of freedom in the photoinduced ultrafast
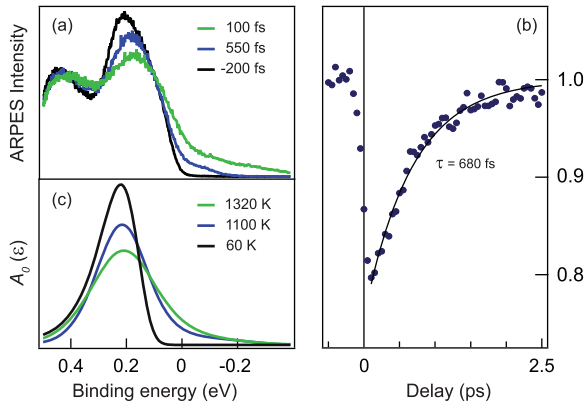
FIG. 23. Ultrafast Mott gap renormalization in $1T\text{-}TaS_2$ upon near-IR optical excitation. (a) Γ-point EDCs at different pump-probe delays measured at 30 K base temperature, highlighting the pump-induced transfer of spectral weight from the LHB to the previously gapped region. (b) Dynamic response of the Mott phase as outlined by the transient LHB intensity peak normalized to the equilibrium value. The almost-instantaneous collapse is followed by a subpicosecond recovery. (c) Simulated spectral function of the curves in (a) calculated via a single-band Hubbard model in which the electronic temperature T_e at different delays is the dominant term driving the phase transition. From Perfetti et al., 2006.

MIT in $1T\text{-}TaS_2$. This conclusion agrees with that of Ligges et al. (2018), who investigated the recombination dynamics of doublons (i.e., doubly occupied sites). In particular, they demonstrated an instantaneous light-induced population of the UHB that subsequently disappears in less than 100 fs, as shown in Figs. 24(a) and 24(b). The doublon-hole recombination processes are estimated to occur on a timescale analogous to that of electron hopping $\hbar/J \sim 14$ fs, which is much faster than the half period of the highest-frequency phonons in $1T\text{-}TaS_2$ of 11.9 THz. This finding, supported by nonequilibrium dynamical mean field theory calculations, suggests that the observed doublon dynamics is purely electronic in origin, thus excluding any CO-related lattice contributions (Ligges et al., 2018).

With respect to the coexistence of Mott and CO physics in $1T\text{-}TaS_2$, Wang et al. (2020) showed that the commensurate CO phase features interlayer stacking with dimerization (i.e., doubling of the unit cell along the c axis). To investigate the contributions of the out-of-plane dimerization and electronic correlations to the MIT, J. Dong et al. (2023a) tracked the ultrafast gap filling at Γ of $1T\text{-}TaS_2$ in the commensurate CO phase with different probe polarizations. Corroborated by ab initio calculations, they reported evidence of both light-induced melting of the CO long-range order (i.e., structural contribution) and the appearance of midgap states on a timescale faster than half a period of the CO amplitude mode [a hint of electron correlations (Perfetti et al., 2006; Ligges et al., 2018)]. Another TR-ARPES study tracked light-induced dynamics in an intermediate phase of $1T\text{-}TaS_2$ that can be attained upon heating the sample from the commensurate CO to the triclinic CO phase (Bao et al., 2023). In this intermediate phase, Bao et al. (2023) reported evidence of Mott physics, while the commensurate CO phase with layer

dimerization behaves like a band insulator. Moreover, recent studies on a similar but less studied compound ($1T\text{-}TaSe_2$) mapped how coherent oscillations of the CO amplitude mode (~ 2.2 THz) modulate the energy position of the valence band at Γ, thus suggesting a direct link between the CO amplitude mode and the electronic gap near the Fermi level (Sayers et al., 2020). Further exploration of ultrafast charge dynamics points toward a charge-transfer gap rather than a Mott gap at Γ (Sayers et al., 2023).

A quasi-instantaneous closure of the band gap upon optical pumping has also been observed in VO_2, a prototypical system exhibiting a transition from a monoclinic insulating phase to a rutile metallic phase at 340 K (Morrison et al., 2014). Note that while at equilibrium this MIT transition involves a fundamental crystallographic modification, Wegkamp et al. (2014) reported a transient metallic state reached by near-IR excitation that retains the monoclinic structure characteristic of the insulating state, resulting in a photoinduced state with no thermally driven counterpart. The observed ultrafast gap renormalization in VO_2 is then described in terms of enhanced screening upon photoexcitation from the V valence bands, which precedes significant charge carrier relaxation (occurring within 200 fs) and atomic rearrangement (Wegkamp et al., 2014; Wegkamp and Stähler, 2015). A study of the sibling compound V_2O_3 investigated the nonthermal phases that develop immediately after photoexcitation not only for the paramagnetic insulating phase but also for the correlated metallic phase of this prototypical Mott-Hubbard compound. This TR-ARPES study showed that in both cases the out-of-equilibrium phases are electronic in nature and driven by transient orbital overpopulation (Lantz et al., 2017).

The capability of unraveling the full pathway of photo-induced MITs in detail was showcased in recent TR-ARPES
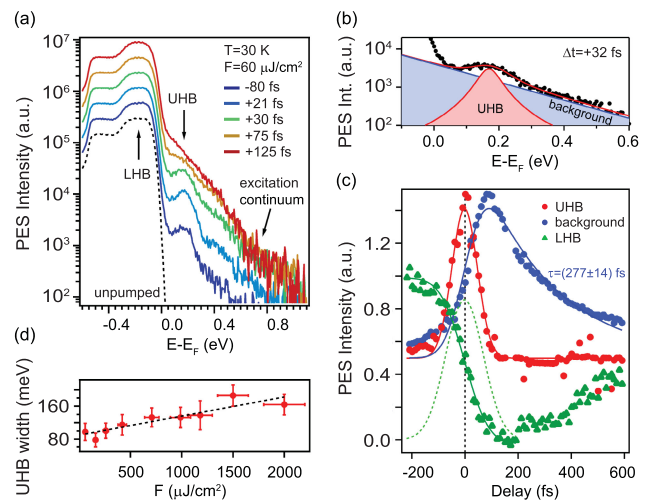

FIG. 24. Light-induced doublon dynamics in $1T\text{-}TaS_2$. (a) Transient EDCs acquired at normal emission for selected pump-probe delays showing the ultrafast population of the UHB. (b) Exemplary fit of an EDC above E_F consisting of a linear background and a Lorentzian peak corresponding to the UHB. (c) Comparison between the ultrafast evolution of the UHB and the slower dynamics of LHB and the underlying background supporting an electronic origin of the UHB dynamics. (d) Fluence dependence of the UHB peak width. From Ligges et al., 2018.

studies of indium nanowires on a silicon (111) surface In/Si(111) (Chávez-Cervantes *et al.*, 2018, 2019; Nicholson *et al.*, 2018, 2019). This system undergoes a transition from a low-temperature CO-mediated insulating phase to a metallic state at 130 K. While the former phase is defined by an (8×2) symmetry of the lattice characterized by distorted In hexagons, the latter exhibits a (4×1) symmetry with arrays of In zigzag chains leading to the emergence of three bands crossing E_F. When the system is irradiated in the insulating state with a near-IR pump excitation, TR-ARPES data reveal a MIT developing in three distinct stages [Figs. 25(a)–25(c)]. First, the gap at the (8×2) zone boundaries closes within 200 fs (the red arrows in Fig. 25). Next the conduction bands at $\Gamma_{(8 \times 2)}$ gradually shift down in energy and cross E_F after 500 fs (the yellow arrows in Fig. 25) due to the structural transition, which is in agreement with time-resolved electron diffraction data (Frigge *et al.*, 2017)]. Finally, the now-metallic bands draw apart in momentum along k_x (the blue arrows in Fig. 25), marking the final structural transition into the (4×1) metallic phase. The map of the photoexcited carriers in momentum space shown in Fig. 25(d) highlights the strongly delocalized character of the photoexcited electrons across the BZ, while the photoholes are localized at the zone boundaries. Starting with the photoinduced electron and hole distributions across the BZ as input, *ab initio* molecular dynamics calculations accurately reproduce the three stages of the MIT observed experimentally and provide insights about the dynamics of nuclei and chemical bonds. In fact, this procedure reveals the ultrafast formation of the delocalized metallic bond along the zigzag chains on the same timescale as the gap closing.

Nicholson *et al.* (2018) exemplified how TR-ARPES can be combined with theory to achieve a comprehensive understanding of photoinduced MITs, including both momentum- and real-space descriptions. In addition, Chávez-Cervantes *et al.* (2019) investigated the MIT in In/Si(111) upon sub-CO-gap excitation. They showed that mid-IR excitation with a peak electric field of up to 0.9 MV/cm ($h\nu_{pump} = 190$ meV $\lesssim$ 300 meV) drives a MIT via multiphoton absorption on a timescale comparable to that observed with near-IR excitation, thus hinting at a similar microscopic mechanism.

Finally, Gierster, Vempati, and Stähler (2021) recently reported a photoinduced ultrafast semiconductor-to-metal transition at the surface of ZnO at low excitation fluences (~ 10 μJ/cm^2) in comparison to the other systems described in this section. This ultrafast transition is driven by the concomitant depletion of in-gap states and the emergence of a surface photovoltage (see Sec. VI) that leads to partially filling states at the Fermi level.

C. Excitonic insulators

In semimetals or narrow-gap semiconductors when conduction electrons and valence holes form excitons, bound states whose energy exceeds the small band gap, a macroscopic condensation may occur, leading to the emergence of a novel excitonic insulating (EI) phase (Jérome, Rice, and Kohn, 1967). Among the materials proposed to exhibit an EI ground state are $1T$-TiSe$_2$ and Ta$_2$NiSe$_5$. Both were recently investigated using TR-ARPES not only to provide supporting evidence of the excitonic nature of their insulating
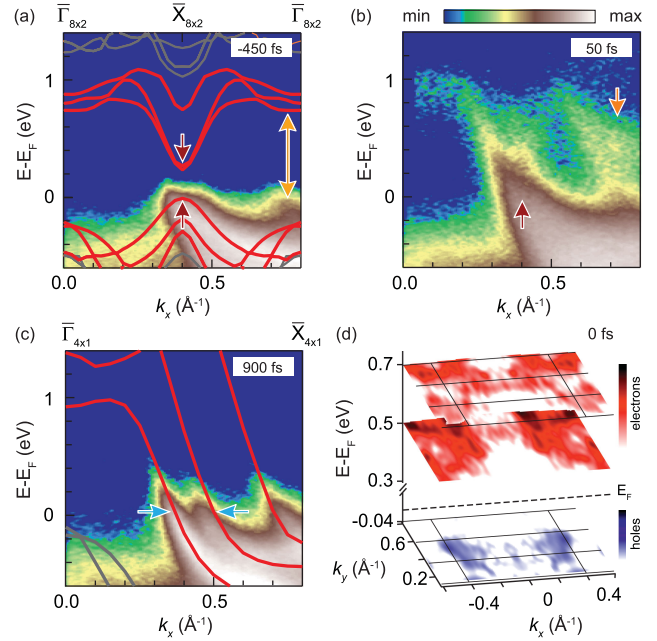

FIG. 25. Pathway of the photoinduced MIT captured in momentum space in indium nanowires on a silicon (111) surface In/Si(111). (a)–(c) TR-ARPES spectra of In/Si(111) at 25 K for selected time delays highlighting the transition from an insulating (8×2) to a metallic (4×1) phase. The solid lines in (a)–(c) are the calculated electronic band structures in the (8×2) and (4×1) phases. The pump-induced transition occurs in three stages: closing of the gap at $X_{(8 \times 2)}$ (red arrows), downward shift of the CB at $\Gamma_{(8 \times 2)}$ (yellow arrows), and separation in momentum of the now-metallic band (blue arrows) to reach the final (4×1) structure. (d) Experimental momentum-space distribution of excited electrons (red) and holes (blue) at the time of the pump excitation. The map is obtained by subtracting the photoemission signal measured at -1 ps from that measured at 0 ps. Adapted from Nicholson *et al.*, 2018.

state but also to pursue optical control of the electron-hole pairs for future applications.

$1T$-TiSe$_2$ is characterized by an indirect band gap and undergoes a CO transition below 200 K. The study of its spectral response in the time domain (Rohwer *et al.*, 2011; Hellmann *et al.*, 2012a; Monney *et al.*, 2016) revealed a characteristic sub-80-fs gap melting time, which is much faster than the dynamics observed for the M-point Peierls gap in $1T$-TaS$_2$ (see also Sec. IV.A), and it exhibits a distinct pump-fluence dependence. In particular, Rohwer *et al.* (2011) reported a direct relation between the gap response time in $1T$-TiSe$_2$ and the inverse of $\sqrt{n}$ (where n is the photoinduced carrier density), which corresponds to the timescale of the carriers' screening buildup in response to an ultrashort optical excitation. Both the ultrafast response time and the photo-enhanced screening hypothesis are consistent with a description of the insulating state in terms of EI physics [in agreement with momentum-resolved electron energy-loss spectroscopy results (Kogar *et al.*, 2017)], although the presence of strong CO band folding prevents one from conclusively excluding the possibility that electron-lattice interactions may contribute to the gap formation in $1T$-TiSe$_2$.
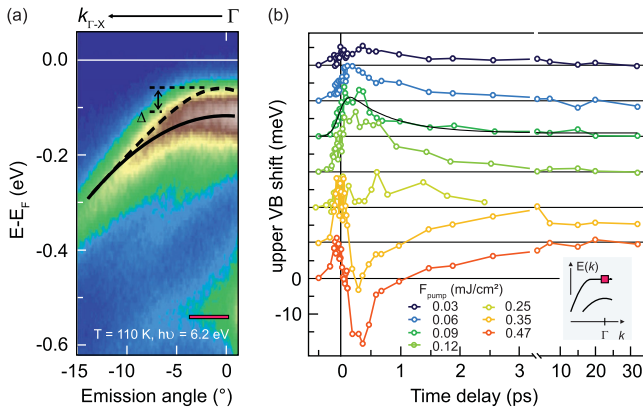
FIG. 26. Transient changes in the valence band of the excitonic insulator TNS upon a near-IR excitation. (a) Equilibrium ARPES spectra of TNS acquired around Γ at 110 K. The solid (dashed) black line is a guide for the eye for the VB dispersion before (after) the optical excitation. The red bar indicates the momentum integration interval for extracting EDCs to track the VB peak position. (b) Time-dependent energy shift of the upper VB peak at Γ for different pump fluences. Two different behaviors are observed around an empirical critical fluence $F_C \sim 0.2$ mJ/cm^2. An upward shift with a 1 ps recovery to the original binding energy at low fluences is opposed to a 200-fs-delayed downward shift at higher fluences, which is followed by a settling into a lower-energy position relative to the equilibrium case. Adapted from Mor et al., 2017.

In contrast to 1T-TiSe$_2$, in Ta$_2$NiSe$_5$ (TNS) the proposed excitonic insulating phase does not coexist with a CO phase, and it is defined by a direct band gap of $\sim$0.15 eV at the Γ point [Fig. 26(a)]. However, the characteristic flattening of the valence band below the critical temperature 326 K is concomitant with a structural phase transition from an orthorombic to a monoclinic unit cell (Wakisaka et al., 2012). Whether the phase transition is excitonic or structural (i.e., electronic or elastic) in nature remains an open question. Since the two phenomena would occur on the same energy scale and with no symmetry distinction, distinguishing between them may rely on the different time dependences of the electronic and phononic instabilities. All of these aspects make TNS an excellent system for investigation using low-photon-energy TR-ARPES to explore the photoinduced electronic dynamics of an EI candidate. However, despite extensive recent experimental efforts, the hierarchy of the fundamental interactions involved in the gap formation of TNS is still under debate. Upon near-IR pump excitation, a significant loss of spectral weight occurs at the top of the upper VB in the first 100–200 fs. The fluence dependence of the VB depletion resembles that of 1T-TiSe$_2$ (i.e., higher fluences lead to faster depletion) (Mor et al., 2017; Okazaki et al., 2018a), thus supporting the description of TNS in terms of the excitonic insulator. Along with the loss of spectral weight, a photoinduced shift in binding energy of the top VB at Γ was reported and analyzed as a function of the pump fluence by Mor et al. (2017). As illustrated in Fig. 26(b), two different behaviors are observed around an empirically reported critical fluence $F_C \sim 0.2$ mJ/cm^2. At low fluences the VB shifts toward the Fermi level and recovers its original position within

1 ps, whereas above F_C a deviation to higher energy is detected at $\sim$200 fs after the pump excitation and its relaxation process overshoot the initial equilibrium position. While the upward shift (gap closure) is understood in terms of a gap renormalization stemming from the transiently enhanced screening (as expected in a semiconductor), the downward shift in energy (gap enhancement) has been interpreted as a signature of an increase in the excitonic condensate density. These results suggest the possibility of controlling the gap parameter in TNS by tuning the fluence of the optical pump.

Other TR-ARPES studies of TNS have instead reported a transition from an insulating to a semimetallic state upon near-IR excitation (Okazaki et al., 2018a; Tang et al., 2020; Saha et al., 2021), as well as transient electron dynamics in the CB (Mor et al., 2022). In particular, a CB electronlike pocket is observed emerging at Γ on an ultrafast timescale, as illustrated in Fig. 27(a). By analyzing the EDCs at the top of the VB as a function of the pump fluence, Tang et al. (2020) showed that the drastic reduction of the gap amplitude upon increasing fluence reaches a saturation at $F_C = 0.29$ mJ/cm^2, above which a residual gap of $\sim$15% of the initial value persists [see Figs. 27(b) and 27(c)], possibly due to a forbidden band crossing between the CB and the VB. The decay rate of the
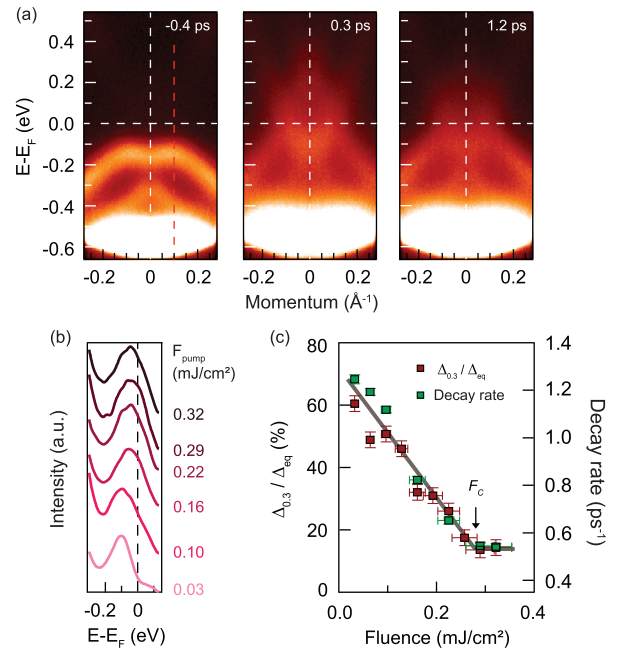

FIG. 27. Photomelting of the excitonic gap in TNS. (a) TR-ARPES spectra of TNS acquired along the Ta and Ni chains at a base temperature of 30 K showing the ultrafast emergence of a CB electronlike pocket at Γ upon a 1.77 eV excitation. (b) EDCs extracted at the top of the VB [the dashed red line in (a)] at time delay 0.3 ps as a function of the pump fluence. (c) Fluence dependence of the photoinduced change of the energy gap extracted from the EDCs in (b) (red squares). While a linear decrease in the gap size is reported at low fluences, a saturation point is reached at $F_C = 0.29$ mJ/cm^2, resulting in a residual gap even at high fluences. The same fluence dependence is also observed for the decay rate of the nonequilibrium electrons obtained in a 0.1 eV window above E_F (green squares). Adapted from Tang et al., 2020.

nonequilibrium quasiparticles above E_F exhibits the same fluence dependence. These findings demonstrate that ultrafast near-IR excitations suddenly and significantly alter the electronic distribution of TNS, although the direct band gap remains finite at all times, regardless of the high electronic temperature attained. We also note that tailored light excitations have been predicted to drive band insulators into excitonic insulators, renormalizing the dispersion of the VB and the CB (Perfetto *et al.*, 2019).

To assess the phononic contribution to the observed gap renormalization, the pump-induced coherent oscillations of the upper VB binding energy were analyzed in recent investigations by Tang *et al.* (2020) and Baldini *et al.* (2023). Several coherent modes of A_{1g} and B_{1g} symmetry have been identified in the TR-ARPES spectra; the frequencies of these modes in the 1–5 THz range are in agreement with previous Raman experiments on TNS (Werdehausen *et al.*, 2018). Despite probing the same set of coherent modes, the two studies reached different conclusions in regard to the nature of the instability in TNS. On the one hand, Tang *et al.* (2020) argued that the observed ultrafast phase transition is purely electronic in origin and occurs without a structural transition owing to the pump-fluence independence of the observed coherent modes. This interpretation suggested that the system retains its low-temperature monoclinic structure across the transition even above F_C. On the other hand, the combined TR-ARPES and ultrafast electron diffraction study of Baldini *et al.* (2023) reported (i) a slow (∼0.3–0.4 ps) and long-lasting response of the VB depletion to the optical pumping, (ii) the detection of coherent oscillations in the upper VB even during the pump-probe signal rise time, and (iii) a sudden drop followed by a slower decrease over several picoseconds of the diffraction peaks corresponding to the monoclinic structure. Based on this evidence, Baldini *et al.* (2023) excluded a dominant role for the electronic degree of freedom in the gap formation in TNS and instead attributed it to the symmetry lowering that accompanies the structural transition.

Further contributing to the debate on the relative roles of electron-electron and electron-phonon interactions in TNS, Golež *et al.* (2022) recently reported a significant photo-induced broadening of the valence band of TNS, while changes in the band gap amplitude are an order of magnitude smaller. These experimental observations are summarized by the EDCs of Fig. 28(b), as well as the transient evolution of the VB linewidth for three different excitation fluences in Fig. 28(c). Indeed, the response of TNS to an external optical perturbation (with E and A representing the electric field and vector potential, respectively) can be qualitatively modeled by two-band (CB and VB) spinless fermions in one dimension coupled to dispersionless phonons of energy Ω_0 as

$$H = \sum_{k,\alpha \in (0,1)} [\epsilon_{k-A}]^{\alpha\alpha'} c^\dagger_{k,\alpha} c_{k,\alpha'} + V \sum_i n_{i,0} n_{i,1}$$
$$+ \sum_i \left[\sqrt{\lambda} X_i - E(t) \right] c^\dagger_{k,0} c_{k,1} + \sum_i \frac{1}{2} \left[X_i^2 + \frac{1}{\Omega_0^2} \dot{X}_i^2 \right]$$
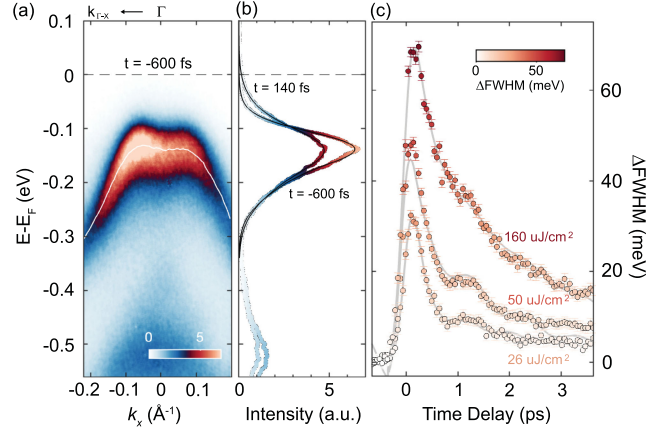$$+ \text{H.c.}, \tag{5}$$

FIG. 28. Tracking the light-induced broadening of the VB line shape as an indicator of the strength of electron-electron interactions in TNS. (a) TR-ARPES spectrum acquired along the Γ-X direction of Ta_2NiSe_5 before photoexcitation. (b) EDCs centered at Γ before and after the optical excitation showing a pump-induced broadening of the peak. (c) Transient variation of the spectral broadening of the VB at Γ for three different excitation fluences. Adapted from Golež *et al.*, 2022.

where $c^\dagger_{k,\alpha}$ is the electron creation operator, V is the Coulomb interaction between the CB and the VB, and λ is the electron-phonon interaction strength corresponding to a displacement X_i. The ratio between V and λ determines whether an optical excitation leads mainly to a spectral feature broadening (V driven) of gap closure (λ driven). By comparing the fluence and momentum dependence of the ARPES linewidth with nonequilibrium many-body simulations, Golež *et al.* (2022) demonstrated the dominant (but not necessarily sole) contribution of the electron-electron interaction to the stabilization of the excitonic gap in TNS. They further emphasized how a detailed analysis of transient many-body interactions (encoded in the transient evolution of the spectral function; see Sec. II.B.1), in parallel with state-of-the-art nonequilibrium simulations, can offer an unprecedented degree of information on the microscopic origin of the order parameter in correlated systems.

D. Superconducting condensate

The normal-to-superconducting-state phase transition in (quasi-)2D systems has been the subject of extensive investigation over the past four decades. Among the major classes of high-temperature superconductors, quasi-2D Bi-based copper oxides in single crystal form are particularly suitable for study using ARPES and TR-ARPES because they present a natural cleavage plane and can be doped across a wide range. The cuprates family is characterized by a layered perovskite structure in which the square planar CuO_2 plane forms a single-layer or multilayer conducting block separated by insulating charge reservoir layers. Since the Cu-O bands are the lowest-energy electronic states, the CuO_2 block is believed to hold a key role in the development of the macroscopic electronic properties in these materials, including high-temperature superconductivity. In particular, a band stemming from the hybridization between Cu $d_{x^2-y^2}$ and O
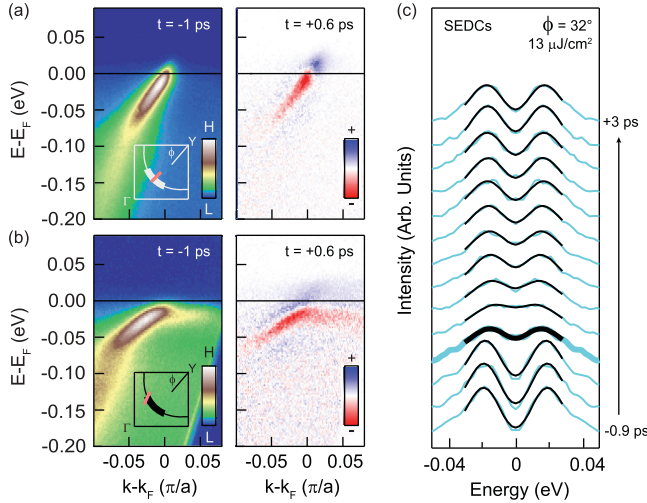
FIG. 29. Transient evolution of the near-nodal superconducting gap of optimally doped Bi2212 ($T_c = 91$ K). (a) TR-ARPES dispersion acquired along the gapless nodal direction ($\phi = 45°$) before and after near-IR optical pumping. For positive delays, the differential spectrum, obtained by subtracting the ARPES map at negative delay, is shown. Inset in the left panel: location of the cut in the Fermi surface. (b) Same as in (a) but along the off-nodal cut ($\phi = 31°$), where the band bending due to the presence of the gap is clearly visible. (c) Transient evolution of the superconducting gap at $\phi = 32°$ mapped via symmetrized EDCs. The spectroscopic modifications observed within the originally gapped region are described using a phenomenological model (black solid lines) that includes a single-scattering term and the superconducting gap amplitude. Adapted from Smallwood, Hinton et al., 2012.

$2p_x$ and $2p_y$ orbitals is observed near the Fermi level; see Figs. 29(a) and 29(b). Owing to the distinct d-wave symmetry of the superconducting order parameter in cuprates, the gap disappears along the direction diagonal to the Cu–O bond [nodal direction; Fig. 29(a)], becomes finite off-node [Fig. 29(b)], and reaches its maximum at the edge of the Brillouin zone at the antinode (Shen et al., 1993; Damascelli, Hussain, and Shen, 2003).

Various all-optical probes were employed over the past few decades to explore Bi-based cuprates in the time domain (Giannetti et al., 2016). These investigations suggested that, while perturbative near-IR excitations melt the superconducting condensate on subpicosecond timescales in a nonthermal fashion (Kabanov et al., 1999; Gedik et al., 2005), intense mid-IR pulses may drive a transient superconducting state above the critical temperature T_c (Fausti et al., 2011; Hu et al., 2014; Liu et al., 2020). The development of TR-ARPES systems with energy resolution comparable to the superconducting gap of cuprates (Smallwood, Jozwiak et al., 2012; Cilento et al., 2016; Parham et al., 2017) has triggered extensive studies of the transient response of the superconducting condensate in momentum space. To date TR-ARPES studies of cuprates have relied almost solely on near-IR pumping; while this excitation range does not couple directly to the superconducting condensate, it does redistribute carriers within the charge-transfer gap, driving an ultrafast

superconducting-to-normal-state phase transition (Giannetti et al., 2016; Baldini et al., 2020).

The initial TR-ARPES investigations focused on the gapless nodal direction (Perfetti et al., 2007; Cortés et al., 2011), where transient suppression of the coherent spectral weight at the Fermi momentum was reported and attributed to the light-induced melting of the superconducting condensate via an enhancement of phase fluctuations (Graf et al., 2011). However, recent investigations on various Bi-based cuprates have excluded an unequivocal relation between the observed suppression of the nodal spectral weight and superconductivity, and have instead discussed the phenomenon as a direct manifestation of the energy and temperature dependence of the single-particle lifetime within the Fermi-liquid formalism (Zonno, Boschini, and Damascelli, 2021; Zonno et al., 2021).

A major milestone in the study of the physics of cuprates via TR-ARPES came in 2012, when Smallwood, Hinton et al. (2012) demonstrated for the first time the ability to track the evolution of the near-nodal superconducting gap in optimally doped $Bi_2Sr_2CaCu_2O_{8+\delta}$ [(Bi2212-OP91); $T_c = 91$ K] with subpicosecond temporal resolution. Figures 29(a) and 29(b) show the effect of near-IR pumping on the nodal and gapped off-nodal (gap of $\sim$15 meV) electronic dispersions, respectively, via TR-ARPES differential maps. Along with the expected redistribution of photoemission intensity across the Fermi level, a transient modification of spectral weight within the originally gapped region is observed in the off-nodal cut. To quantify such transient behavior for different pump fluences and Fermi-surface angles, Smallwood, Hinton et al. (2012) analyzed the symmetrized EDCs at $\mathbf{k}_F$ in terms of a phenomenological model defined by the superconducting gap amplitude and a single-particle scattering rate $\Sigma(\omega) = -i\Gamma + \Delta^2/(\omega + i\Gamma)$; see Fig. 29(c). While for angles close to the nodal direction the pump excitation largely affects the gap response and quasiparticle recombination rates remain higher than 20 ps, shifting the angle away from the node reduces the pump-induced effect on the gap and makes the quasiparticle dynamics faster.

This seminal work created the foundation for TR-ARPES exploration of dynamical processes in high-temperature superconductors and, in particular, the study of the hierarchy in the gap formation of cuprates, including the long-lasting investigation of the interplay between phase coherence and pairing strength in determining T_c (Emery and Kivelson, 1995; Caviglia et al., 2008). In this regard, while early investigations reported a photoinduced gap closure in the near-nodal region (Smallwood, Hinton et al., 2012; Smallwood et al., 2014), subsequent studies have instead revealed a filling of the superconducting gap accompanied by only a minimal modification of the gap amplitude itself upon near-IR excitation (Parham et al., 2017; Zhang et al., 2017; Boschini et al., 2018; Zonno, Boschini, and Damascelli, 2021). This ultrafast filling of the superconducting gap is illustrated in Figs. 30 and 31(b) by the temporal evolution of the TR-ARPES differential spectra of optimally doped Bi2212 and the off-nodal EDCs at $\mathbf{k}_F$ normalized to the thermal broadening of underdoped Bi2212, respectively. Spectral weight is observed inside the gapped region without a significant energy shift of the quasiparticle peak toward the Fermi level. The observed

transient filling of the gap has been interpreted in terms of a photoinduced loss of phase coherence, which quenches superconductivity on an ultrafast timescale.

A quantitative analysis of this phenomenon has been conducted by introducing an additional scattering rate into the self-energy used to fit the gapped spectral function, the pair-breaking scattering rate Γ_p, which is associated with the density of phase fluctuations $\Sigma(\omega) = -i\Gamma_s + \Delta^2/(\omega + i\Gamma_p)$. This extended self-energy has been successfully employed to fit the transient evolution of the off-nodal EDCs at $\mathbf{k}_F$ (either symmetrized or normalized to momentum-integrated EDCs along the gapless nodal direction) and track the light-induced dynamics of the pairing strength and pair-breaking scattering rate, as shown in Fig. 31(c) (Boschini *et al.*, 2018; Zonno, Boschini, and Damascelli, 2021). While both the dynamics of the single-particle scattering rate Γ_s and the gap amplitude Δ are locked to the evolution of the electronic occupation, i.e., the electronic temperature T_e, the transient filling of the superconducting gap represented by Γ_p exhibits much faster ($\sim$1 ps) and decoupled dynamics, as shown in Fig. 31(d). This result established the nonthermal origin of the pump-induced melting of the coherent condensate and was interpreted in terms of a light-induced nonequilibrium bosonic population that, by enhancing phase fluctuations via pair-breaking events, fills the superconducting gap and does not affect the pairing strength [Fig. 31(e)] (Boschini *et al.*, 2018). Moreover, the observation of similar gap-filling dynamics in different Bi-based compounds suggests a universal mechanism for the superconducting-to-normal-state phase transition in Bi-based cuprates that relies on the loss of macroscopic phase coherence in the underdoped-to-optimally-doped regime (Zonno, Boschini, and Damascelli, 2021). Note that evidence of phase fluctuations above T_c was also reported in Bi2212 after analysis of the nodal electron dynamics across a range of dopings and temperatures (Zhang *et al.*, 2013).

Furthermore, evidence of an ultrafast filling of the superconducting gap was also reported for Fe-based superconductors in a recent high-energy-resolution TR-ARPES study on the Fe-chalcogenide $FeSe_{0.45}Te_{0.55}$ superconductor (Nevola *et al.*, 2023). However, in contrast with the cuprates, in this case the quenching of the superconducting phase has been associated with a metastable light-induced modification of the underlying antiferromagnetic order.

In contrast to the extensive efforts made to study the superconducting gap, the transient evolution of the pseudogap (PG), i.e., the partial suppression of the density of states near the Fermi level even above T_c, has yet to receive comparable attention. This neglect is due to the larger BZ momenta defining the PG phenomenon in hole-doped cuprates, which makes such studies unattainable with the limited momentum space accessible by low-photon-energy laser systems employed to study the cuprates' near-nodal region. To date only a few TR-ARPES studies have focused on the transient evolution of the PG (Miller *et al.*, 2017; Cilento *et al.*, 2018; Boschini *et al.*, 2020b). At the antinode of the hole-doped Bi2212 cuprate, Cilento *et al.* (2018) reported the appearance of short-lived ($\sim$0.5 ps) in-gap states in tandem with an ultrafast broadening of the O $2p_x$ band. They attributed this finding to a resonant photoinduced transfer
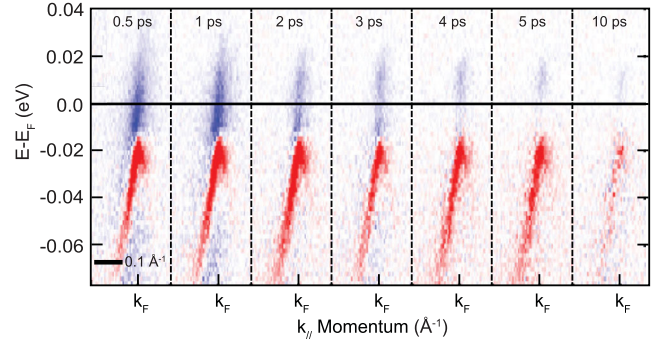

FIG. 30. Visualizing the filling of the superconducting gap in optimally doped Bi2212 upon near-IR pump excitation. The off-nodal TR-ARPES differential spectra at various pump-probe delays (0–10 ps range) highlight the transfer of spectral weight within the gap region without a notable energy shift of the quasiparticle peak toward E_F. Adapted from Parham *et al.*, 2017.

of electrons between Cu and O orbitals, attesting to the close relationship between low- and high-energy scales in high-temperature cuprates, as well as indicating a correlation-driven origin of the PG phenomenon (Cilento *et al.*, 2018). Another example of a TR-ARPES investigation of the PG in cuprates is the study by Boschini *et al.* (2020b) at the antiferromagnetic hot spot of the optimally doped electron-doped cuprate $Nd_{2-x}Ce_xCuO_4$, which can also be accessed at low photon energies, as discussed in Sec. VII.C (Boschini *et al.*, 2020b).

E. Summary and outlook

This section has summarized a few representative examples of how TR-ARPES has offered insights into the dynamics of quantum materials, highlighting the underlying mechanisms, the reaction pathways, and the ability to disentangle competing interactions of photoinduced phase transitions in quantum materials. To date this technique has relied almost exclusively on high-photon-energy excitations that are not resonant with specific collective modes (Basov, Averitt, and Hsieh, 2017; de la Torre *et al.*, 2021), and thus for the most part correspond to light-induced melting of ordered phases. In fact, in all of the previously discussed cases, light excitations have led to the quenching of order parameters or the loss of long-range coherence. Recent developments in the generation of tunable pump excitations in concert with high-repetition-rate XUV sources (see Sec. II.C) promise revolutionary insights into control of quantum matter by light, opening the way to momentum-resolved surveys of novel light-induced phases of matter previously studied only via momentum-integrated techniques (Fausti *et al.*, 2011; Mitrano *et al.*, 2016; Cavalleri, 2018; X. Li *et al.*, 2019; Disa, Nova, and Cavalleri, 2021).

V. ELECTRON-PHONON COUPLING

As discussed in Sec. II, equilibrium ARPES is a useful tool for investigating the occupied electronic band structure of quantum materials but does not offer direct insights into bosonic degrees of freedom, such as the phonons' occupation and dispersion, which can instead be obtained via complementary particle or light scattering experiments. Whereas ARPES may
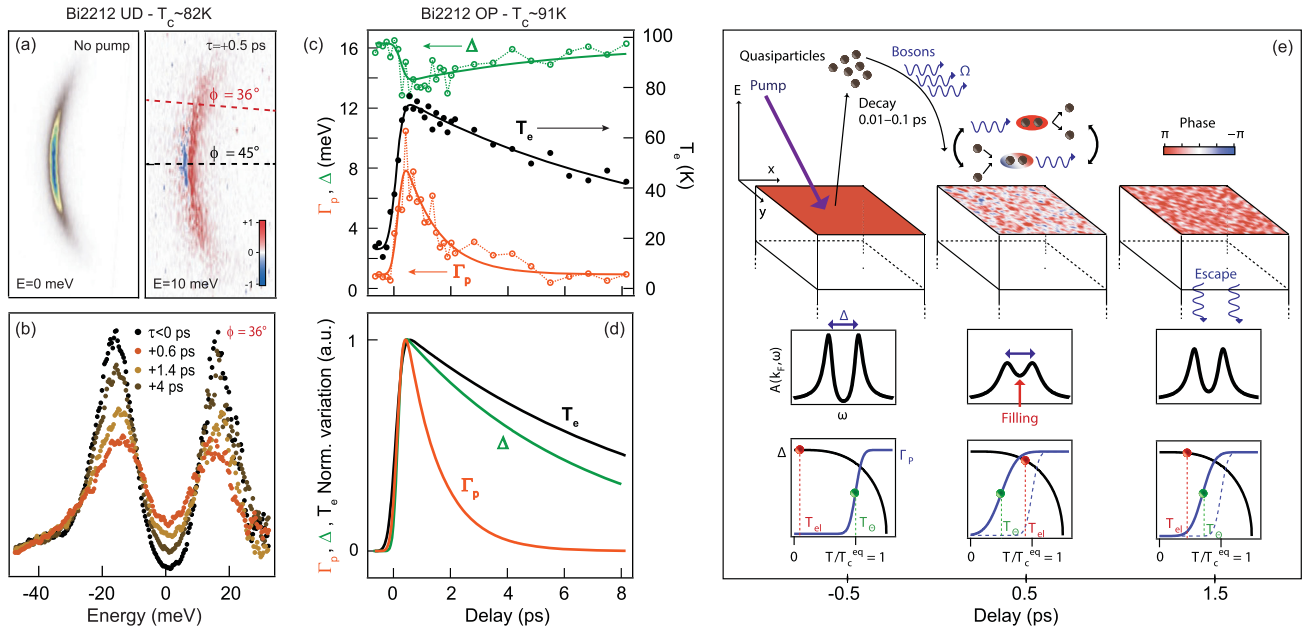
FIG. 31. Key role of phase fluctuations in the transient filling of the superconducting gap in Bi-based cuprates. (a) Equilibrium Fermi surface and differential $[I(\tau = +0.5\text{ ps}) - I(\tau = -0.5\text{ ps})]$ isoenergy contour mapping at 10 meV above the Fermi level for underdoped Bi2212 with $T_c \sim 82$ K. (b) Off-nodal EDCs at $\mathbf{k}_F$ of underdoped Bi2212 with $T_c \sim 82$ K normalized to momentum-integrated nodal EDCs ($\phi = 45°$) at different pump-probe delays ($\sim 8\ \mu\text{J/cm}^2$ incident fluence). EDCs have been deconvolved from the energy-resolution broadening prior to the division. (c) Transient evolution of the superconducting gap Δ and pair-breaking scattering rate Γ_p extracted by fitting symmetrized EDCs (left axis), and T_e extracted along the nodal direction (right axis) for optimally doped Bi2212 with $T_c \sim 91$ K. The solid lines are phenomenological double-exponential decay fits to the data. (d) Comparison between the normalized transient variation of the quantities in (c). The faster and disentangled dynamics characterizing Γ_p attest to the nonthermal origin of the ultrafast enhancement of the phase fluctuations. (e) Sketch of the transient collapse of the condensate driven by a loss of phase coherence. The top panels show a schematic diagram of the energetics of the process and the related real-space condensate phase coherence, the middle panels display the spectral function at $k = k_F$ when phase fluctuations are induced, and the bottom panels show the temporal evolution of the pairing strength (Δ, black line) and of Γ_p (blue line). While the pairing is defined by T_e (red spheres and dashed lines), the superconductivity and the macroscopic T_c are determined by the onset of phase coherence T_Θ (green spheres and dashed lines), which is proportional to the superfluid density. Adapted from Boschini *et al.*, 2018, and Zonno, Boschini, and Damascelli, 2021.

provide hints via analysis of the electron self-energy $\Sigma(\omega, \mathbf{k})$ as to how many-body interactions influence the electronic band dispersion and lifetime, such an approach often relies on specific working assumptions (for example, knowledge of the bare electronic dispersion). This requirement makes identifying the different electron interactions on the basis of equilibrium ARPES spectra challenging and typically impractical. Since its first applications, the extension of ARPES into the time domain has offered a new pathway for exploring different electron scattering processes on their intrinsic timescales, such as electron-electron (commonly under 100 fs) and electron interactions with underlying collective excitations. In this regard, we note that the observation of multiple decay times is at odds with Matthiessen's rule, which states that multiple scattering channels should lead to a single effective relaxation time (Kemper, Abdurazakov, and Freericks, 2018). In the past two decades, several methods with different levels of sophistication have been developed within the realm of TR-ARPES in an effort to provide a direct and precise estimate of relevant electron-boson couplings.

This section reviews the main TR-ARPES approaches to qualitatively or quantitatively estimate the fundamental electron-phonon coupling (EPC) phenomenon in quantum

materials. Section V.A discusses the use of multitemperature models and collision integrals to describe the transient evolution of the electronic temperature and photoemission intensity, from which a qualitative estimate of the EPC is derived. Their application to two specific systems, topological insulators and graphene or graphite, is presented in detail. Section V.B covers how the photoexcitation of coherent phonons may drive a transient modulation of the binding energy of electronic states, offering a direct way to estimate the EPC, as well as the application of a novel analysis procedure of TR-ARPES spectra in the Fourier frequency domain. Finally, Sec. V.C focuses on how detailed tracking of the transient evolution of the electron self-energy provides insights into EPC, with particular emphasis on the case of cuprate superconductors. Finally, Sec. V.D reviews a recently developed TR-ARPES method for extracting the momentum- and mode-resolved electron-phonon matrix elements by detecting quantized relaxation processes of photoexcited electrons.

A. Multitemperature model and collision integrals

The multitemperature model (MTM) is one of the most commonly used semiclassical approaches for qualitatively

estimating the strength of electron scattering processes from nonequilibrium spectroscopy experiments. Going all the way back to early pump-probe studies, MTM has been implemented to extract EPC in metals and BCS superconductors (Kaganov, Lifshitz, and Tanatarov, 1957; Anisimov, Kapeliovich, and Perel'Man, 1974; Allen, 1987; Brorson *et al.*, 1990; Tao and Zhu, 2010). The simplest MTM comprises just two coupled subsystems with different temperatures; it is known as the two-temperature model (2TM) (Carpene, 2006; Bovensiepen, 2007). The 2TM assumes that the incoming light couples directly to the electronic bath, which subsequently transfers energy to the phononic bath (i.e., only excitations nonresonant to phononic modes are considered). The timescale at which such redistribution of energy occurs is dictated by the fundamental EPC strength of the material, as well as the natural frequency of the phonons involved in the process. Within this framework, tracking how the electronic temperature $T_e(\tau)$ evolves in a TR-ARPES experiment enables one to also infer valuable information about the phononic population and EPC in terms of the evolution of the lattice temperature $T_l(\tau)$.

Under the assumptions that only one Einstein phonon mode with frequency Ω is involved and that the Eliashberg function is given by $\alpha^2 F(\omega) \propto \delta(\omega - \Omega)$, the following rate equations hold (Allen, 1987; Perfetti *et al.*, 2007; Sterzi *et al.*, 2016):

$$\frac{\partial T_e(\tau)}{\partial \tau} = \frac{S(\tau)}{C_e} - \frac{3\lambda\Omega^3(n_e - n_l)}{\hbar\pi k_b^2 T_e(\tau)}, \tag{6}$$

$$\frac{\partial T_l(\tau)}{\partial \tau} = \frac{C_e}{C_l}\frac{3\lambda\Omega^3(n_e - n_l)}{\hbar\pi k_b^2 T_e(\tau)}, \tag{7}$$

where $S(\tau)$ describes the temporal profile of the optical excitation, $C_{e(l)}$ is the electronic (lattice) specific heat, k_b is the Boltzmann's constant, and $n_{e,l}$ define the Bose-Einstein distribution functions for phonons calculated at temperatures T_e and T_l, respectively. Here we note that the Eliashberg function $\alpha^2 F(\omega)$ and, consequently, the EPC constant $\lambda = 2\int_0^\infty d\omega[\alpha^2 F(\omega)/\omega]$ depend on (i) the phononic density of states and (ii) the fundamental electron-phonon matrix element[3] (Mahan, 2000; Kemper *et al.*, 2014; Gierz *et al.*, 2015b; Maklar *et al.*, 2022a). Note also that the latter contribution, when integrated over momentum, implicitly contains the electronic density of states, i.e., the available scattering phase space. Therefore, any variations of the electronic structure and screening, including phase transitions accompanied by the filling and/or closure of energy gaps, may result in a transient modification of the available scattering phase space and, consequently, of λ; see Sec. II.B and Fig. 5. In general, any changes of λ across an equilibrium or out-of-equilibrium phase transition or following a modification of the electronic dispersion may result from changes in the electronic

---

[3]The electron-phonon matrix element can be expressed as $g = \sqrt{\hbar/2M_C\Omega_q}\langle\mathbf{k}+\mathbf{q}|\Delta H|\mathbf{k}\rangle$, where $|\mathbf{k}\rangle$ and $|\mathbf{k}+\mathbf{q}\rangle$ denote the electron initial and final states connected by a phonon with momentum $\mathbf{q}$, ΔH is the deformation potential, and M_C is the atomic mass (Grimwall, 1980; Mahan, 2000; Giustino, 2017; Na *et al.*, 2019).
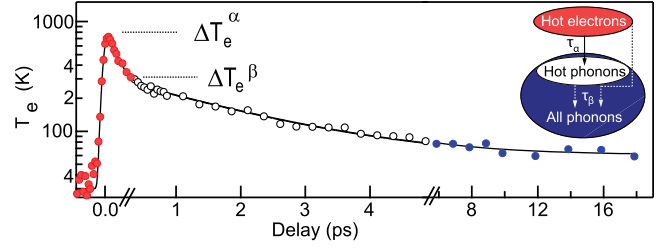

FIG. 32. Application of the MTM to the transient evolution of the effective electronic temperature of $Bi_2Sr_2CaCu_2O_{8+\delta}$ upon a 1.55 eV pump. Three cooling stages are observed, corresponding to different relaxation channels for the electronic and phononic bath following the optical excitation, as sketched in the inset. Adapted from Perfetti *et al.*, 2007.

scattering phase space rather than from significant changes of the phonons' density or fundamental electron-phonon matrix element g connecting two specific $\mathbf{k}$ states (Ciocys and Lanzara, 2023; Razzoli *et al.*, 2023).

One of the main challenges of applying MTMs is determining the timescale at which temperature, which is an equilibrium property, can be properly adopted in an out-of-equilibrium context (Mueller and Rethfeld, 2013; Rohde *et al.*, 2018; Na *et al.*, 2020; Kratzer *et al.*, 2022). In fact, at zero pump-probe delay when pump and probe pulses are overlapped, any optical excitation elicits a highly nonthermal state characterized by an out-of-equilibrium electronic distribution, which may exhibit a marked momentum dependence, as well as significant deviations from the equilibrium Fermi-Dirac distribution. In this respect, applying MTM in the context of TR-ARPES relies on the major assumption that the electronic bath thermalizes on ultrafast timescales via electron-electron interactions into a quasiequilibrium state for which an effective electronic temperature can be defined. The transient evolution of $T_e(\tau)$ can then usually be deduced by fitting the broadening of the spectral weight at E_F to a Fermi-Dirac distribution, although more advanced analysis methods can provide more accurate estimates (Ulstrup, Johannsen *et al.*, 2014). In addition, a light-induced shift of the chemical potential often accompanies the broadening of the Fermi edge. Although this review does not discuss this effect in detail, note that transient shifts of the chemical potential offer valuable insights into the DOS of the unoccupied states and into transient photodoping effects (Crepaldi *et al.*, 2012; Wang *et al.*, 2012; Gierz *et al.*, 2013; Miller *et al.*, 2015, 2017).

Perfetti *et al.* (2007) first applied an extended 2TM to TR-ARPES data of a Bi-based high-temperature cuprate superconductor by extracting $T_e(\tau)$ from fitting a Fermi-Dirac distribution to the broadening of the spectral weight along the gapless nodal direction. As illustrated in Fig. 32, a 50 fs thermalization time was estimated for the electronic bath, followed by further relaxation via a subset (~20%) of strongly coupled phonons on a 110 fs timescale, and then with the entire lattice on the picosecond timescale. By applying Eqs. (6) and (7), Perfetti *et al.* (2007) extracted $\lambda \sim 0.27$ for phonons in the 40–70 meV range, which have been proposed to be responsible for the band-structure renormalization known as the kink phenomenon in Bi-based cuprates (Lanzara *et al.*, 2001).
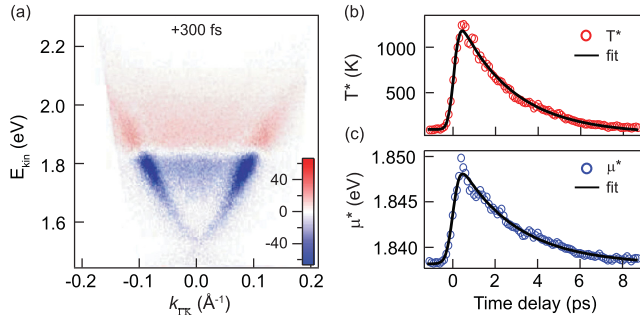
FIG. 33. Transient evolution of the electronic temperature and chemical potential in the topological surface state of Bi_2Se_3 after near-IR pump excitation. (a) Pump-probe TR-ARPES spectrum displayed as the difference between the signal at $+300$ fs and the signal at -500 fs. Temporal evolution of (b) the effective temperature T^* and (c) the effective chemical potential μ^* obtained from fitting a sequence of EDC curves at k_F. In each case, a single decay exponential function captures the observed temporal dynamics, with characteristic relaxation times equal to ~ 2.5 and ~ 2.7 ps, respectively. A simple thermal model based on the extracted $T^*(\tau)$ and $\mu^*(\tau)$ reproduces the ultrafast evolution of the nonequilibrium charge population in the topological surface state at different binding energies. Adapted from Crepaldi et al., 2012.

As with MTMs, collision integrals follow a rate-equation formulation and offer the following general framework for describing electron scattering processes (Ashcroft and Mermin, 1976; Del Fatti et al., 2000; Yang et al., 2015; Sjakste, Tanimura et al., 2018):

$$\frac{\partial f(\epsilon_{\mathbf{k}})}{\partial \tau} = -\int \frac{d\mathbf{k}'}{(2\pi)^3} W_{\mathbf{k},\mathbf{k}'} f(\epsilon_{\mathbf{k}})[1 - f(\epsilon_{\mathbf{k}'})]$$
$$+ \int \frac{d\mathbf{k}'}{(2\pi)^3} W_{\mathbf{k}',\mathbf{k}} f(\epsilon_{\mathbf{k}'})[1 - f(\epsilon_{\mathbf{k}})], \qquad (8)$$

where $\epsilon_{\mathbf{k}}$ is a specific electronic state at momentum $\mathbf{k}$, $f(\epsilon_{\mathbf{k}})$ is the occupation of the $\epsilon_{\mathbf{k}}$ state, and $W_{\mathbf{k},\mathbf{k}'}$ is the probability of scattering from $\mathbf{k}$ to $\mathbf{k}'$ (for example, electron-electron, electron-phonon, and impurity scattering). Collision integrals, and rate-equation-based models in general, can describe the transient evolution of the photoemission intensity $I(\mathbf{k}, \omega, \tau)$ and estimate intrinsic electron relaxation times of the system. However, Yang et al. (2015) highlighted that $I(\mathbf{k}, \omega, \tau)$ [more precisely, $f(\mathbf{k}, \omega, \tau)$, as discussed in Sec. II.B.1] maps the population dynamics and is not directly related to the single-particle lifetime (which is inversely proportional to the imaginary part of the electron self-energy) and, consequently, is not directly related to the momentum-averaged fundamental electron coupling constants. Since the relaxation times of the population dynamics are strongly affected by the momentum and energy dependence of the out-of-equilibrium electronic distribution and light-induced modifications of the scattering phase space (Maklar et al., 2021), relying solely on the fitting of $T_e(\tau)$ and $I(\mathbf{k}, \omega, \tau)$ provides only phenomenological and qualitative estimates of the underlying scattering times and electron coupling constants.

Over the past two decades, MTMs and collision integrals (and, more generally, other phenomenological

multiexponential decay models) have then been applied to a variety of quantum materials, ranging from topological insulators (Crepaldi et al., 2012, 2013; Sobota et al., 2012, 2014b; Reimann et al., 2014; S. Zhu et al., 2015; Kuroda et al., 2016; Sánchez-Barriga et al., 2017; Sterzi et al., 2017) to graphene and graphite (Ishida et al., 2011; Gierz et al., 2013; Johannsen et al., 2013, 2015; Stange et al., 2015; Ulstrup et al., 2015b; J.-A. Yang et al., 2017; Rohde et al., 2018), as well as superconductors (Perfetti et al., 2007; Cortés et al., 2011; Dakovski et al., 2015; Piovera et al., 2015; Smallwood et al., 2015; Zhang et al., 2016; Konstantinova et al., 2018; Fanfarillo et al., 2021), semiconductors and semimetals (Tanimura, Kanasaki, and Tanimura, 2015; Sterzi et al., 2016; Tanimura et al., 2016; Crepaldi et al., 2017; Caputo et al., 2018; Chen et al., 2018, 2020; Bao et al., 2022), and half-metals (Battiato et al., 2018). Before continuing on to closely examine the application of MTMs and collision integrals in two classes of materials that have been extensively studied by the TR-ARPES community (topological insulators and carbon-based layered compounds such as graphene and graphite), we remark that these measurements mainly access local effects (i.e., relaxation processes) and provide little (or at best indirect) insights into nonlocal effects (i.e., diffusive transport). Brorson, Fujimoto, and Ippen (1987) proposed an experimental strategy to distinguish local and nonlocal effects in pump-probe studies by optically exciting the sample on both sides (front and back) while probing its out-of-equilibrium response only on one side (the front). This method was successfully applied to a Au/Fe/MgO(001) heterostructure (Beyazit et al., 2020, 2023) and, by applying a 2TM accounting for diffusive electronic transport, revealed the transition from superdiffusive to diffusive electronic transport in the Au layer as a function of its thickness (Kühne et al., 2022).

1. Topological insulators

Since the first observation of the topological surface state in TIs (Hasan and Kane, 2010), the ARPES community has sought to estimate the strength of EPC for Dirac electrons, with contradictory results (Hatch et al., 2011; Pan et al., 2012). In an effort to resolve this controversy, MTM together with general considerations about the decay rates of the photoinduced electronic population have been applied in a qualitative fashion to various TIs to gain insights into electron scattering processes within the bulk bands and the topological surface state. As discussed in Sec. III.B, near-IR optical excitation of TIs induces a nonthermal redistribution of carriers within both valence and conduction bulk bands and surface states. Owing to the limited scattering phase space of the surface state, relaxation timescales can extend up to hundreds of picoseconds for Dirac electrons in systems where the chemical potential falls inside the bulk band gap, and a few picoseconds for bulk electrons in systems where the chemical potential lies outside the bulk band gap. Several intertwined relaxation mechanisms have been proposed to account for these relaxation timescales, ranging from inefficient electron-phonon scattering to surface-to-bulk diffusion (Crepaldi et al., 2012, 2013; Hajlaoui et al., 2012; Sobota et al., 2012, 2014a; Wang et al., 2012; Reimann et al., 2014; Sánchez-Barriga
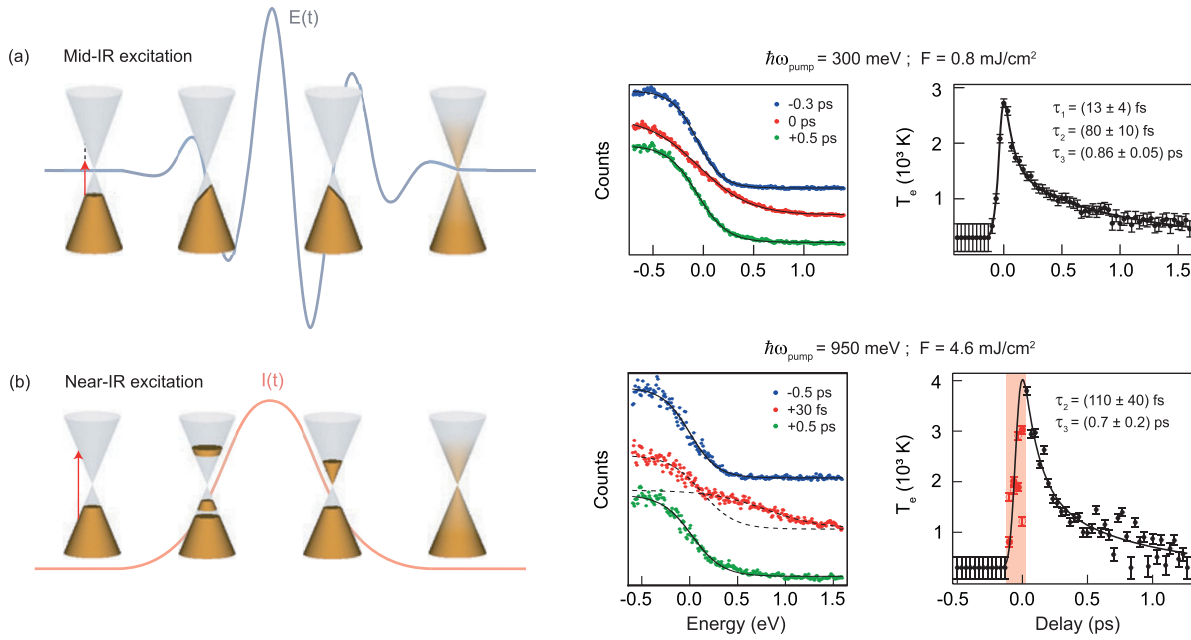
FIG. 34.   MTM analysis of TR-ARPES data of graphene upon (a) mid-IR and (b) near-IR excitations. Left graphic: schematics of the two different excitation schemes illustrating how only the near-IR pump pulse accesses direct optical transitions. The light gray line represents the electric field of the 300 meV pump pulse and the light red line represents the intensity of the 950 meV pump pulse. Middle panels: momentum-integrated EDCs around the K point for selected pump-probe delays, along with Fermi-Dirac distribution fits. Right panels: transient electronic temperature with multiexponential decay fits. Note that while in (a) the pump-induced thermal broadening follows the conventional Fermi-Dirac distribution for all delays, in (b) EDCs at times close to zero are best described by two different Fermi-Dirac fits for electrons and holes (the dashed black lines). These time delays are indicated by red data points and the shaded area in the transient evolution of T_e. Adapted from Gierz *et al.*, 2013.

etal., 2017; Sterzi *et al.*, 2017; Freyse *et al.*, 2018; Khalil *et al.*, 2019; Zhong *et al.*, 2021), as well as bottleneck effects at the Dirac point and surface photovoltage (SPV) effects; see Sec. VI (Hajlaoui *et al.*, 2014; Neupane *et al.*, 2015; S. Zhu *et al.*, 2015; Sánchez-Barriga *et al.*, 2016; Sumida *et al.*, 2017, 2019; Hedayat *et al.*, 2018; Papalazarou *et al.*, 2018; Ciocys *et al.*, 2020). With particular emphasis on electron-phonon coupling in TIs, pioneering studies by Crepaldi *et al.* (2012, 2013), Sobota *et al.* (2012), and Wang *et al.* (2012) extracted the transient electronic temperature for the unoccupied conduction band of Bi_2Se_3 and Bi_2Te_3 and associated the observed decay of ~0.7–2.5 ps to inefficient electron-phonon coupling. Figure 33 showcases the transient evolution of the effective electronic temperature and chemical potential (with characteristic relaxation times of 2.5 and 2.7 ps, respectively) for the topological surface state of Bi_2Se_3 upon near-IR excitation. While the former is ascribed to electron-phonon relaxation processes (via 2TM considerations), the latter is attributed to the relaxation of the excess charge in the CB via diffusion (Crepaldi *et al.*, 2012). Moreover, Sobota *et al.* (2014b) reported a counterintuitive temperature dependence of the decay rate of the conduction band of Bi_2Se_3 (lower decay rates with higher temperatures), and they showed via collision integrals that it originates directly from electron-phonon scattering processes.

The weak electron-phonon coupling of the topological surface state has been further qualitatively assessed in studies that (i) observed a power-law dependence of the surface temperature decay rate on carrier density (Wang *et al.*, 2012), (ii) used XUV light (17.5 eV) to increase the surface

sensitivity, which revealed a saturated electronic temperature at the surface (Crepaldi *et al.*, 2013), and (iii) showed the vanishing of transient pump-induced spin polarization in the topological surface state after ~1.2 ps, a timescale compatible with electron-phonon scattering (Sánchez-Barriga *et al.*, 2016); see also Sec. VII.A.2.

2. Graphene and graphite

Graphene and its three-dimensional allotropic compounds, such as graphite, are characterized by Dirac-like dispersive bands at the corners of the hexagonal Brillouin zone, as well as strong coupling of electrons to optical phonons with momentum $Q = 0$ (Γ phonons) and $Q = K$ (K phonons). Efficient electron-phonon scattering is one of the possible limiting factors for the transport properties of graphene-based devices, hindering their use for energy-harvesting purposes (Bonaccorso *et al.*, 2010; Scheuch *et al.*, 2011; Tielrooij *et al.*, 2013; Johannsen *et al.*, 2015).

MTMs have been extensively applied to TR-ARPES investigations of graphene and graphite to gain valuable insights into the intrinsic timescale of electron-phonon scattering. Although no electronic states are expected in the proximity of E_F away from the BZ corners, an early 6 eV TR-ARPES investigation of graphite reported a transient modification of the photoemission intensity at the Γ point (Ishida *et al.*, 2011). Such incoherent spectral weight in the BZ center stems from a scattering of K/K' electrons into Γ mediated by the emission of an optical phonon with a momentum $Q = K$, and is therefore a manifestation of the
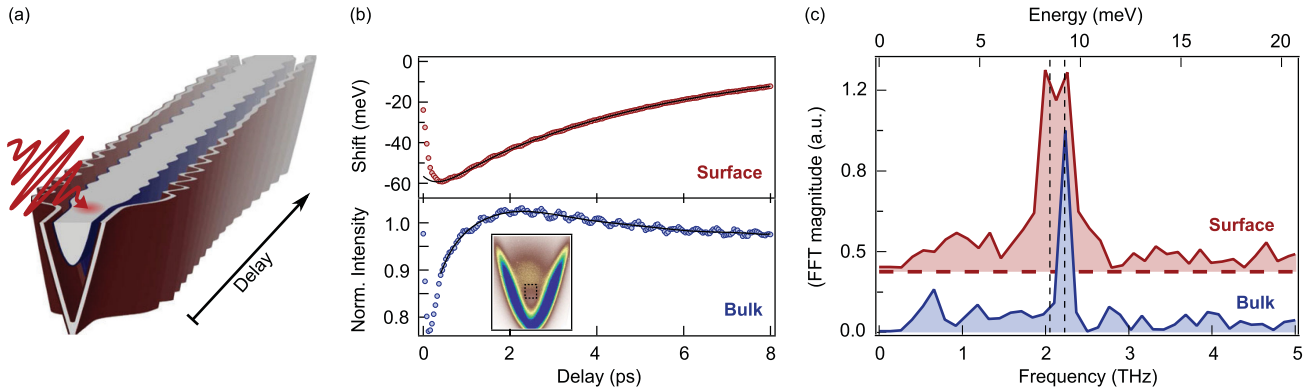
FIG. 35. Disentangling the surface and bulk contributions to the light-induced coherent oscillations in Bi_2Se_3. (a) Sketch of the optical excitation and relaxation of coherent phonons in the bulk and surface bands. (b) Top panel: time-dependent shift of the TSS. Bottom panel: temporal evolution of the CB photoemission intensity integrated within the black box indicated in the inset. The black solid lines are smooth curve fits using tenth-order polynomials. (c) Fast Fourier transform (FFT) of the residuals from the fit for the TSS and CB showing the presence of distinct frequencies. While the oscillations of the CB can be captured by a single undamped cosine, the oscillations of the TSS are best fit using a beat pattern represented by the sum of two cosine functions. Adapted from Sobota et al., 2014a.

strong electron-phonon coupling characteristic of graphite (Liu et al., 2010). By inspecting the transient evolution of the spectral broadening at Γ, Ishida et al. (2011) reported the emergence of a nonthermal electronic distribution in the first ~200 fs and suggested that the generation of strongly coupled optical phonons occurs mainly during this ultrafast timescale. Moreover, given the impossibility of reliably extracting the transient $T_e(\tau)$ at these early time delays, Ishida et al. (2011) proposed that the 2TM is applicable in graphite only after ~200 fs.

Subsequent TR-ARPES studies employed XUV probe light to explore the ultrafast electrodynamics at the K point of graphene or graphite. Among these, Gierz et al. (2013) investigated the evolution of $T_e(\tau)$ of 200 meV hole-doped graphene upon both mid-IR (0.3 eV) and near-IR (0.95 eV) excitations, as shown in Fig. 34. While the mid-IR photon energy is too low to drive any direct optical transitions and leads to a spectral broadening well captured by a Fermi-Dirac distribution [Fig. 34(a)], a nonthermal distribution is observed around time zero upon near-IR pump excitation [Fig. 34(b)]. In the latter case, the photoemission signal can be described as the sum of two distinct Fermi-Dirac distributions centered above and below the Dirac point (Ulstrup et al., 2014; Gierz et al., 2015a; Gierz, Mitrano et al., 2015; Gierz, 2017). Moreover, in both excitation schemes of Fig. 34, $T_e(\tau)$ exhibits a ~100 fs decay associated with the fast scattering of electrons off optical phonons, and a slower picosecond component stemming from the anharmonic decay of optical phonons into acoustic phonons and from electron-acoustic phonon scattering. Other XUV-probe TR-ARPES studies on graphene (Johannsen et al., 2013, 2015; Stange et al., 2015; Ulstrup et al., 2015b) reported similar decay times.

Extended MTMs have also been applied to TR-ARPES data in an effort to evaluate the impact of supercollisions [i.e., the coupling between electrons and acoustic phonons mediated by disorder, which acts as a source of momentum (Alencar et al., 2014)] on the electron relaxation processes. These studies have led to apparently contradictory results: whereas the

inclusion of supercollisions appears to be necessary to describe the evolution of $T_e(\tau)$ in graphene (Johannsen et al., 2013; Someya et al., 2017), a basic strongly coupled phonon model, which neglects any coupling between electrons and acoustic phonons, succeeds in reproducing the experimental data of graphite (Stange et al., 2015). This apparent disagreement may originate simply from the different impurity levels of graphite and exfoliated graphene on different substrates.

Pomarico et al. (2017) first investigated how the EPC of bilayer graphene on SiC(0001) may be modulated via resonant excitation of the in-plane E_{1u} bond-stretching phonon at 200 meV. By combining terahertz time-domain spectroscopy and analysis of the decay time of the transient electronic temperature extracted from TR-ARPES data, they reported a transient threefold enhancement of the EPC constant.

Despite the extensive adoption of MTMs in studying graphene and graphite, two general limitations remain in this approach to analyzing TR-ARPES data: (i) MTMs cannot identify specific optical phonons involved in the ultrafast thermalization processes and (ii) MTMs are not strictly valid for short pump-probe delays when an electronic temperature cannot be defined unambiguously. The first obstacle can be overcome either by combining TR-ARPES with complementary time-resolved techniques, such as time-resolved Raman spectroscopy (J.-A. Yang et al., 2017) and ultrafast electron diffuse scattering spectroscopy (Stern et al., 2018), or by applying more advanced analysis procedures to the TR-ARPES signal (Na et al., 2019); see Sec. V.D. Leveraging these methods, the aforementioned experimental investigations established that the optical K phonons are the main drivers of the observed ultrafast sub-100-fs relaxation processes. Rohde et al. (2018) addressed the second obstacle by showing that the nonthermal electronic distribution converges to a single Fermi-Dirac distribution within ~50 fs (incident fluence >0.9 mJ/cm^2) as a result of electron-electron and electron-phonon scattering. However, the duration of the nonthermal window depends on the excitation density and
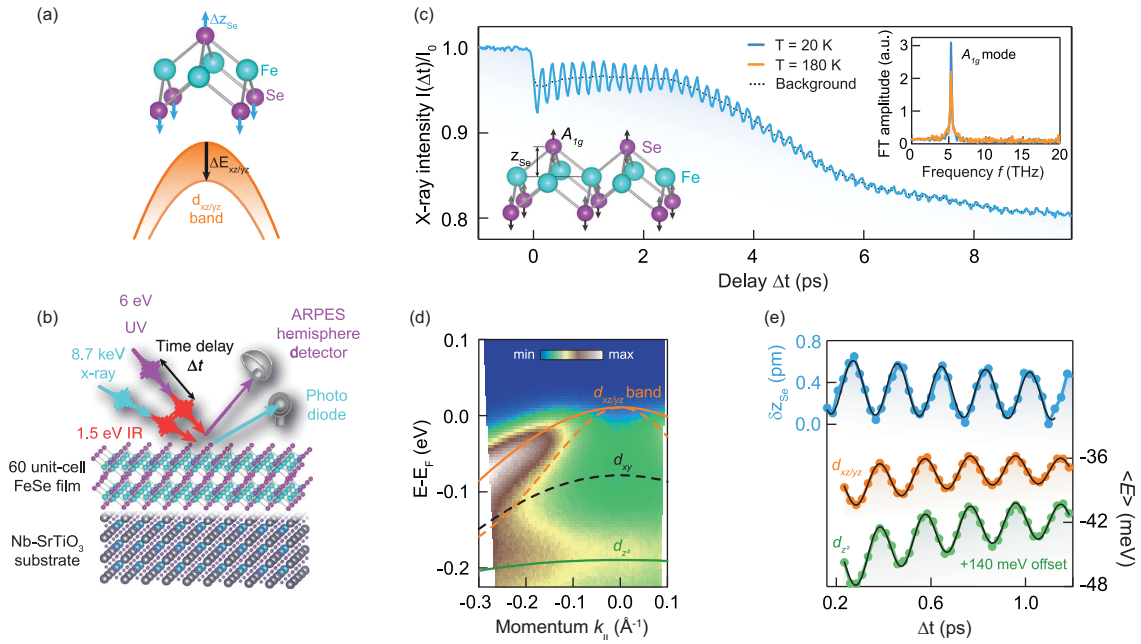
FIG. 36. Response to optical excitations of the A_{1g} phonon mode in FeSe/SrTiO$_3$ films tracked via combined time-resolved x-ray diffraction and TR-ARPES measurements. (a) Schematic of the A_{1g} phonon mode, which periodically modulates the electronic band energies. (b) Sketch of the experimental strategy. (c) Temporal evolution of the x-ray intensity of the (004) Bragg peak upon near-IR pumping, which excites a coherent A_{1g} phonon mode; see inset. (d) Equilibrium ARPES spectrum of FeSe along the $\Gamma - X$ direction acquired at 20 K. Renormalized density functional theory calculations for the electronic band dispersions are represented by superimposed lines (solid for ARPES-detected bands and dashed for unresolved bands). The orbital characters of the bands are also indicated. (e) Relationship between (blue line) the oscillations of the Se displacement δz_{Se} probed by time-resolved x-ray scattering and (orange and green lines) the momentum-averaged binding energy shift of the electronic bands obtained using TR-ARPES. Adapted from Gerber *et al.*, 2017.

may lengthen in low-fluence regimes (Na *et al.*, 2020; Kratzer *et al.*, 2022). We emphasize that semiclassical models of the TR-ARPES data based on collision integrals do not strictly require equilibrium thermodynamic variables such as temperature to be well defined, which allows a description of the overall transient evolution of the photoemission intensity even in highly nonthermal regimes (Na *et al.*, 2020).

B. Light-driven coherent phonons

When performing TR-ARPES experiments, it is not uncommon to observe coherent oscillations in the transient photoemission intensity or the binding energy of the probed electronic states. Light-inducing coherent phononic modes provide advantageous approaches [via resonant phonon pumping (Först *et al.*, 2011), nonresonant excitation (Zeiger *et al.*, 1992; Dhar, Rogers, and Nelson, 1994), or coherent control (Rettig *et al.*, 2014)] to investigate how the electronic bath couples to specific phonon modes. While TR-ARPES studies with light excitations resonant to specific phonon modes are still rare (Gierz *et al.*, 2015b; Pomarico *et al.*, 2017), the use of nonresonant visible and near-IR pump pulses has led to observations of phonon-mediated coherent oscillations in the photoemission signal. This phenomenology has been reported for different classes of materials ranging from metals (Papalazarou *et al.*, 2012; Sakamoto *et al.*, 2022) and superconductors (L. Yang *et al.*, 2014; Gerber *et al.*, 2017; Okazaki *et al.*, 2018b; Yang, Sobota *et al.*, 2019; Suzuki, Shin, and Okazaki, 2021; Yang *et al.*, 2021)

to topological insulators (Sobota *et al.*, 2014a, 2023; Golias and Sánchez-Barriga, 2016) and chalcogenides (Perfetti *et al.*, 2006; Hein *et al.*, 2020; Tang *et al.*, 2020; Suzuki *et al.*, 2021; Baldini *et al.*, 2023). Nonresonant high-photon-energy light pulses can drive coherent phonons through two main mechanisms (Garrett *et al.*, 1996): (i) impulsive stimulated Raman processes, usually occurring in transparent compounds where the pump photon energy is smaller than the optical gap and prompting sinelike oscillations (Zeiger *et al.*, 1992), and (ii) displacive processes, commonly observed in opaque materials as a consequence of an abrupt modification of the electronic density, which in turn triggers cosinelike displacive motions of ions around new coordinates (Dhar, Rogers, and Nelson, 1994).

Generally speaking, any shift in the binding energy $\Delta_{\mathbf{k}}$ of the Bloch state $|\mathbf{k}\rangle$ can be related to the atomic displacement u driven by a particular mode and the electron-phonon matrix element $g_{\mathbf{k}}$ for that electronic state and phonon mode ($\Delta_{\mathbf{k}} = g_{\mathbf{k}} u$) (Grimwall, 1980; Giustino, 2017). The direct relation between $\Delta_{\mathbf{k}}$ and $g_{\mathbf{k}}$ enables one to gain valuable insights into the coupling of the electronic states probed via TR-ARPES with coherent phonon modes by tracking the coherent oscillations of the electronic band structure at the frequency of the light-induced phonon mode.

1. Coherent oscillations in the TR-ARPES signal

This section focuses on two emblematic TR-ARPES studies in which detection of coherent oscillations allowed
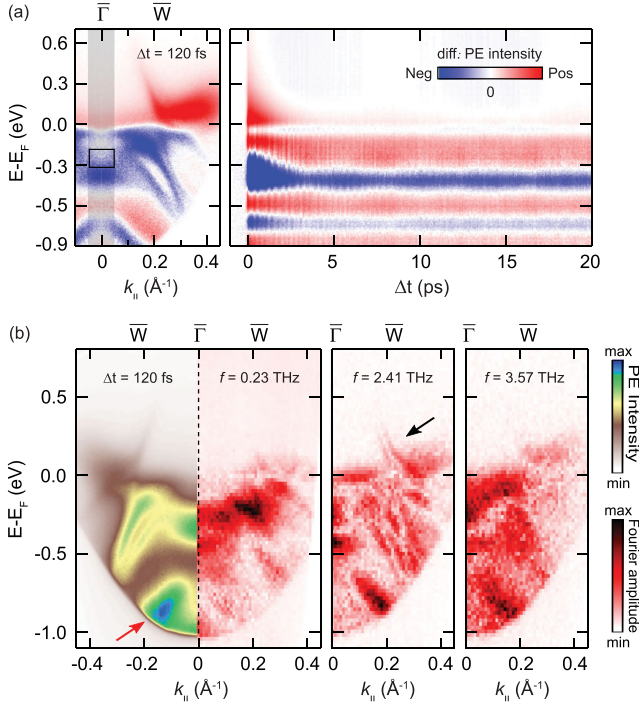
FIG. 37. Momentum-space visualization of the band selectivity of the electron-phonon coupling in T_d-WTe$_2$ via frequency-domain ARPES. (a) Left panel: differential ARPES spectrum of T_d-WTe$_2$ along the $\bar{\Gamma} - \bar{W}$ direction acquired 120 fs after near-IR pump excitation. Right panel: transient evolution of the differential ARPES intensity around Γ showing clear oscillations of the binding energies modulated by multiple frequencies. (b) Frequency-domain ARPES maps (i.e., Fourier-transformed photoemission signals) for selected frequencies. The analysis highlights the band selectivity of the phonon excitations (the red arrow) and also applies to excited states above E_F (the black arrow). From Hein et al., 2020.

quantitative information on the underlying EPC to be extracted. In the work by Sobota et al. (2014a), out-of-plane A_{1g} optical phonons were coherently driven by near-IR light in the topological insulator Bi$_2$Se$_3$. As a result, both the topological surface state and the bulk conduction band displayed oscillations in their binding energies; see Figs. 35(a) and 35(b). Note that the frequency of the coherent modulation of the surface's energy shift was ~10% lower than that observed for the bulk band [2.05 and 2.23 THz, respectively, as depicted in Fig. 35(c)]. This work showcased the capability of TR-ARPES to reveal how coherent phonons may couple differently to surface and bulk states, and crucially relied on high-frequency sensitivity to resolve the softening of the phonon mode at the surface.

In their seminal work, Gerber et al. (2017) combined time-resolved x-ray diffraction and TR-ARPES to track the orbital-resolved deformation potential for the A_{1g} mode in bulk FeSe, an unconventional superconductor in which strong electron correlations are expected to renormalize the EPC. Figures 36(a) and 36(b) illustrate the motivating concept of this work: relate lattice changes (probed via time-resolved x-ray diffraction) to energy shifts of electronic states (accessed via TR-ARPES). Figure 36(c) shows the coherent oscillations in

the x-ray intensity induced by the excitation of the displacive 5.3 THz A_{1g} optical phonon mode, which triggers a periodic variation of the anion height δz_{Se}; see the inset of Fig. 36. This atomic variation was related to the pump-induced energy modulation of two electronic bands observed using TR-ARPES at the Γ point; the two bands exhibit different orbital characters ($d_{xz/yz}$ and d_{z^2}), as illustrated in Figs. 36(d) and 36(e). By combining the lattice and electronic experimental values, Gerber et al. (2017) extracted the value of the deformation potential for the two bands and compared it to the theoretical value obtained by DFT and self-consistent DFT—dynamical mean field theory calculations. Only the latter, which accounts for electron correlations, was able to reproduce the experimental results, thus demonstrating the key role of electron correlations in renormalizing the EPC in FeSe. We mention that a recent TR-ARPES study, by tracking light-induced shifts of the d orbitals around the Brillouin zone center, determined that the tetragonal-to-orthorhombic structural transition plays a key role in the emergence of the electronic nematic phase and shift of the electronic bands of FeSe (Yang et al., 2022).

To conclude, two recent works investigated light-induced coherent phonons in topological insulators by combining TR-ARPES and time-resolved x-ray diffraction. In particular, they demonstrated how the topological surface state of Bi$_2$Te$_3$ couples to different phonon modes (Sobota et al., 2023) and extracted the coupling between the topological surface states of Bi$_2$Se$_3$ and Bi$_2$Te$_3$ and light-induced A_{1g} phonon modes by evaluating mode- and band-resolved deformation potentials (Huang et al., 2023).

2. Frequency-domain ARPES

The detection of coherent oscillations of the band structure requires the use of a probe pulse with (i) a bandwidth sufficiently narrow to resolve any energy shift of the band (commonly of the order of few meV) and (ii) a temporal duration shorter than the phonon cycle. These two conditions have limited the detection of coherent modulations of the electronic dispersion in the TR-ARPES signal to *slow* phonons (<3–4 THz). A novel approach known as frequency-domain ARPES (FD-ARPES) promises to circumvent these difficulties in detecting high-frequency phonons by offering a direct estimate of EPC via a Fourier-like analysis of the TR-ARPES signal. FD-ARPES was recently discussed theoretically (De Giovannini et al., 2020) and demonstrated experimentally (Hein et al., 2020; Suzuki et al., 2021; Lee et al., 2023; Ren et al., 2023). The key advantage of FD-ARPES relies on the fact that, even if the probe bandwidth greatly exceeds the band shifts in energy $\Delta_{\mathbf{k}}$, the Fourier-transformed photoemission signal grants access to the diagonal and off-diagonal electron-phonon matrix elements.

Under the assumption that a single phonon mode Ω_0 [whose displacive motion is parametrized by $u(\tau) = u_0 \sin(\Omega_0 \tau)$] induces variations in both the band energy and the orbital character, the Fourier transform of the TR-ARPES signal [see Eq. (3) in Sec. II.B] evaluated at Ω_0 can be expressed as (De Giovannini et al., 2020)

$$\tilde{I}(\omega, \Omega_0) \propto \frac{i}{2} M \Delta_{\mathbf{k}} \frac{\delta A(\omega)}{\delta \omega} + \frac{1}{2} \frac{\delta M[u(\tau)]}{\delta u(\tau)} \Omega_0 A(\omega). \quad (9)$$

Equation (9) is valid when (i) the band shift $\Delta_{\mathbf{k}}$ is smaller than the probe bandwidth, (ii) u_0 is sufficiently small, and (iii) the electron-phonon coupling is adiabatic. The first term of $\tilde{I}(\omega, \Omega_0)$ depends on the ARPES matrix elements and the derivative of the spectral line shape and is proportional to the diagonal electron-phonon matrix element $g_{\mathbf{k}} = \Delta_{\mathbf{k}}/u_0$. The second term of Eq. (9) stems from the transient modulation of the photoemission matrix elements weighted by the ARPES line shape, and it is proportional to interband electron-phonon matrix elements (De Giovannini *et al.*, 2020). In single-band systems with a well-defined orbital character, only the first term of Eq. (9) survives and the FD-ARPES signal directly probes the EPC. Multiband systems in which interband electron-phonon coupling may have non-negligible contributions can be more challenging to unravel. In addition, the pump-induced modification of the photoemission matrix elements, which has been described theoretically (Freericks and Krishnamurthy, 2016) and reported experimentally (Boschini *et al.*, 2020a), may further complicate a quantitative analysis of the FD-ARPES signal.

Nevertheless, Hein *et al.* (2020) first demonstrated the capabilities of FD-ARPES on the type-II Weyl semimetal T_d-WTe$_2$. The noncentrosymmetric T_d crystal structure is a pivotal requirement for the emergence of Weyl points in nonmagnetic materials (Soluyanov *et al.*, 2015), and a light-induced structural phase transition into a centrosymmetric phase is predicted to annihilate the Weyl points. Such a structural phase transition is expected to occur upon the excitation of the 0.24 THz interlayer shear mode (Sie *et al.*, 2019). In the work of Hein *et al.* (2020) five A_1 coherent phonon modes were excited via a near-IR optical pump, including the 0.24 THz shear mode. Figure 37(a) shows the presence of coherent phonon modes via a conventional analysis of the differential ARPES image, as discussed in Sec. V.B.1. Figure 37(b) compares the TR-ARPES map acquired along the $\bar{\Gamma} - \bar{W}$ direction immediately after the pump excitation (far left panel) with the corresponding FD-ARPES maps obtained at three different frequencies (red maps). The data illustrate how the different pump-induced phonons selectively couple to specific electronic bands, as exemplified by the band indicated by the red arrow, whose FD-ARPES spectral weight is nearly null at 0.23 THz, but intense at 2.41 THz. Owing to the nature of TR-ARPES, this method can resolve the effect of the electron-phonon coupling on individual bands even above the Fermi level [the black arrow in the third panel of Fig. 37(b)]. By specifically focusing on the FD-ARPES map at 0.23 THz, Hein *et al.* (2020) showed how the shear mode modifies the electronic structure of T_d-WTe$_2$ and modulates the spin splitting of bands, a spectral signature that is linked to the broken inversion symmetry of the crystal.

C. Transient evolution of the self-energy

As discussed in Sec. II.B, since the photoemission intensity is proportional to the one-electron-removal spectral function, TR-ARPES can access the transient evolution of many-body
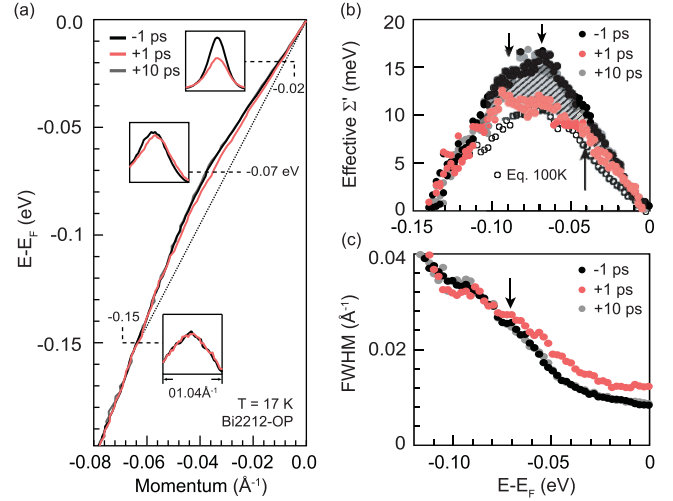

FIG. 38. Evaluation of the electron-phonon coupling response in an optimally doped Bi2212 cuprate via an analysis of the transient electron self-energy. (a) Nodal dispersion for three distinct pump-probe delays, showing the softening of the characteristic kink at ~70 meV at +1 ps. The dashed line corresponds to the linear bare band dispersion. Insets: comparisons of MDCs before and after near-IR pumping around the kink energy. (b) Real part of the electron self-energy extracted at different delays (full circles) and at 100 K in equilibrium conditions (open circles). Arrows mark the suppression of different peaks. (c) Corresponding MDC's full-width at half maximum (FWHM), which is proportional to the imaginary part of the self-energy. A clear pump-induced modification of both the real and imaginary parts of Σ is reported at the kink energy. Adapted from W. Zhang *et al.*, 2014.

interactions via the electron self-energy $\Sigma = \Sigma' + i\Sigma''$, where the real and imaginary parts of Σ are connected by Kramers-Kronig relations. In particular, careful analysis of the experimentally determined ARPES band-structure renormalizations and spectral broadening can evaluate Σ' and Σ'' (Damascelli, Hussain, and Shen, 2003; Sobota, He, and Shen, 2021). However, when a material is perturbed by an optical excitation, the electron self-energy is expected to vary (Kemper *et al.*, 2013; 2014, 2017; Sentef *et al.*, 2013; Kemper, Abdurazakov, and Freericks, 2018). Even for an interacting electron gas without any couplings to bosonic modes, a sudden increase in the electronic temperature is accompanied by a broadening of the spectral line shape, for example, $\Sigma''_{\text{FL}}(\omega, T_e(\tau)) \propto \beta[\omega^2 + \pi^2 k_B^2 T_e(\tau)^2]$ in the Fermi-liquid scenario (Zonno *et al.*, 2021).

In the case of electrons interacting with a bosonic mode of energy Ω_0, the band dispersion deviates from the noninteracting case and a kink appears in the dispersion. Paradigmatic examples of the observation and analysis of an electron-boson kink in the ARPES spectrum range from metals (Valla *et al.*, 1999) to cuprates (at $\Omega_0 \sim 70$ meV) (Johnson *et al.*, 2001; Lanzara *et al.*, 2001) and graphene (at $\Omega_0 \sim 200$ meV) (Bostwick *et al.*, 2007). In equilibrium, the imaginary part of a generic electron-phonon (*e*-ph) self-energy has the form

$$\Sigma''_{\text{e-ph}}(\mathbf{k}, \omega) = \int d\omega' \alpha^2 F(\mathbf{k}, \omega') K(\omega, \omega'), \quad (10)$$
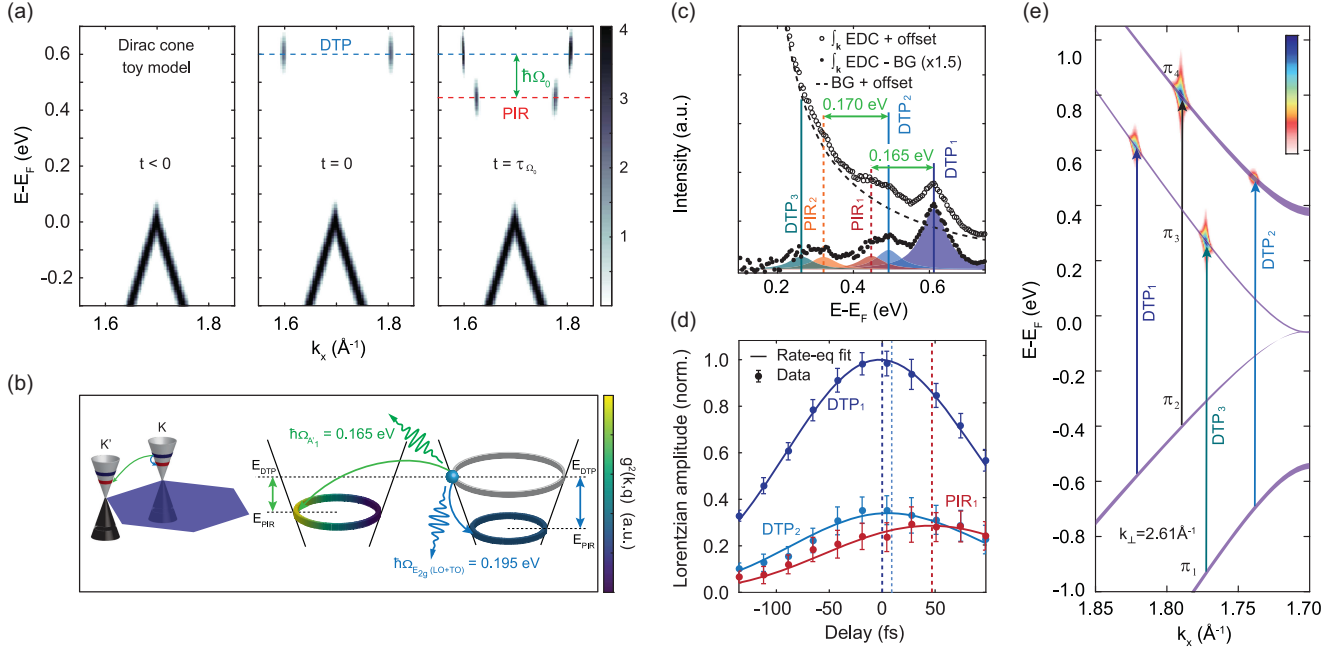
FIG. 39. Momentum-resolved analysis of the quantized electron-phonon decay processes in graphite, allowing the extraction of the mode-projected electron-phonon matrix element $g_{\bar{\mathbf{k}}}$. (a) Simulation of the transient TR-ARPES intensity for a Dirac cone pumped with 1.2 eV photons, including a retarded e-ph interaction with a phonon of energy $\hbar\Omega_0$. At time $t = 0$, the direct transition peak (DTP) feature is observed at $E_{DTP} = 0.6$ eV; at $t = \tau_{\Omega_0}$, the phonon-induced replica (PIR) is observed at $E_{DTP} - \hbar\Omega_0$. (b) Calculation of $g_{\bar{\mathbf{k}}}$ for both an electron in K scattering with an A'_1 mode with a momentum $\sim K$ (green line) into a final state in K' and an electron in K scattering with an E_g^2 mode with a momentum ~ 0 (blue line) into a final state in K. (c) Momentum-integrated EDC around the K point immediately after the pump excitation. Multiple DTPs and PIRs can be identified on top of the hot-electron background based on the momentum-resolved optical joint DOS in (e). (d) Transient evolution of the amplitude of the most prominent peaks: DTP_1 (DTP_2) in dark (light) blue and PIR_1 in red. The dashed lines indicate the peak delays: DTP_2 (PIR_1) is delayed 9 fs (47 fs) with respect to DTP_1. Solid curves represent the electronic occupation of the specified states derived from a rate-equation model fit. The transfer of spectral weight from DTP_1 to PIR_1 is associated with an e-ph scattering time constant $\tau_{\Omega_0} = 174 \pm 35$ fs. Adapted from Na *et al.*, 2019.

where the kernel $K(\omega, \omega')$ depends on the electronic and bosonic distributions, as well as the electronic DOS (Mahan, 2000). In the illustrative scenario wherein a single Einstein mode Ω_0 is present [i.e., $\alpha^2 F(\Omega) = \delta(\Omega - \Omega_0)$], the real part of the electron-phonon self-energy peaks at $|\omega| = \Omega_0$, while the imaginary part of the self-energy becomes nonzero for $|\omega| > \Omega_0$. By extending Eq. (10) into the time domain, it becomes clear that any light-induced changes of the electronic distribution, electron-phonon coupling, or electronic DOS may lead to a transient modification of the self-energy $\Sigma_{e\text{-ph}}(\tau)$.

Different experimental methods have been employed for extracting Σ from TR-ARPES data. Given the inverse relation between Σ'' and the quasiparticle lifetime, qualitative estimates of underlying many-body interactions have been offered by tracking the energy- and momentum-resolved population dynamics. Although population dynamics do not correspond to the single-particle lifetime (Yang *et al.*, 2015), the energy dependence of the population dynamics may qualitatively mimic $\Sigma''(\omega)$ (Smallwood *et al.*, 2015; Yang *et al.*, 2015). This approach has been successfully applied in Bi-based cuprates where the population relaxation rates change abruptly outside the boson window $|\omega| > 70$ meV (Rameau *et al.*, 2016).

The development of TR-ARPES systems with an energy resolution better than the electron-phonon energy window has

paved the way to extract the temporal evolution of the many-body self-energy $\Sigma(\tau)$ via analysis of the transient spectral function (Rameau *et al.*, 2014; W. Zhang *et al.*, 2014; Ishida *et al.*, 2016; Miller *et al.*, 2018; Hwang *et al.*, 2019; Duvel *et al.*, 2022; Zhang, Bao *et al.*, 2022). W. Zhang *et al.* (2014) reported transient changes of the electron-boson kink in Bi2212 cuprate superconductors. As depicted in Fig. 38, near-IR excitation leads to an ultrafast softening of the ~ 70 meV band-structure renormalization, which manifests as transient modifications of both the real and imaginary parts of the electron self-energy at the kink energy [Figs. 38(b) and 38(c), respectively]. W. Zhang *et al.* (2014) also reported a close link between the extracted $\Sigma(\tau)$ and the superconducting gap, thus suggesting that the electron-boson interaction responsible for the ~ 70 meV kink also plays an important role in the formation of the pairing gap. Nonetheless, Eq. (10) shows that transient changes in the self-energy are not unequivocally driven by the modification of the EPC, i.e., $\alpha^2 F(\omega)$, but may also stem from pump-induced modifications to the electronic DOS (Razzoli *et al.*, 2023), which has indeed been reported to occur on an ultrafast timescale in cuprates (Smallwood, Hinton *et al.*, 2012; Parham *et al.*, 2017; Zhang *et al.*, 2017; Boschini *et al.*, 2018), although TR-ARPES data on metallic Bi2212 (nonsuperconducting) still shows a signature of transient changes of the EPC (Hwang *et al.*, 2019).

Although the extraction of $\Sigma(\tau)$ from TR-ARPES data has thus far followed equilibrium analysis procedures, we note that this procedure is not formally correct since the optical creation of a nonthermal electronic distribution may significantly impact the functional form of the self-energy (at least at early pump-probe delays) (Kemper *et al.*, 2017; Kemper, Abdurazakov, and Freericks, 2018). Therefore, achieving a new robust understanding of light-induced changes of electron interactions will require a meticulous analysis of the TR-ARPES spectra, accompanied by a full-nonequilibrium treatment of the TR-ARPES signal.

D. Mapping quantized electron-phonon decay processes

When escaping from a solid, photoelectrons can couple to gapped collective modes and exchange a quantized amount of energy, leading to the emergence of shakeoff replica bands in the equilibrium ARPES spectra (Li and Sawatzky, 2018). A similar phenomenon has recently been observed in the time domain via TR-ARPES, offering a new method for quantitatively extracting the momentum- and mode-resolved electron-phonon matrix elements (Na *et al.*, 2019).

The experimental strategy consists of selectively injecting electrons into specific unoccupied states by optical pumping and then carefully tracking the transfer of spectral weight from those photoexcited states as they begin to relax to lower-energy states via emission of a phonon with energy $\hbar\Omega_0$, as sketched in the toy model of Fig. 39(a). The time constant associated with this transfer of spectral weight (τ_{Ω_0}) is directly related to the electron-phonon contribution to Σ for the specific phonon involved (Na *et al.*, 2019),

$$\frac{1}{\tau_{\Omega_0}} = 2\pi\hbar g_{\bar{\mathbf{k}}}^2 D(\omega_p - \hbar\Omega_0). \tag{11}$$

In Eq. (11) ω_p is the energy of the direct optical transition, $g_{\bar{\mathbf{k}}}^2$ is the square of the mode-projected electron-phonon matrix element averaged over the states $\bar{\mathbf{k}}$ populated by the optical excitation, and D is the electronic DOS (Razzoli *et al.*, 2023). Note that the time constant τ_{Ω_0} defines the contribution to the single-particle lifetime of an electron photoexcited in ω_p and then scattering off the specific phonon Ω_0, and it is not directly related to the population dynamics extracted by tracking the transient evolution of the photoemission intensity (discussed in Sec. V.A). Na *et al.* (2019) observed that the relaxation of nonthermal carriers at the K point of graphite occurs in quantized energy steps corresponding to the emission of strongly coupled optical K phonons. As seen in Figs. 6(b) and 39(c), a series of peaks emerge in the momentum-integrated EDC of the unoccupied states; each peak represents either a direct transition peak (DTP) or a phonon-induced replica (PIR). By tracking the transient evolution of DTP and PIR pairs [Fig. 39(d)], as well as by solving a system of rate equations, Na *et al.* (2019) were able to model the ultrafast timescales of the transfer of spectral weight and also to provide a quantitative estimate for the specific EPC involved in the process. The calculated $g_{\bar{\mathbf{k}}}^2 = 0.050 \pm 0.011$ eV^2 for the coupling of photoexcited electrons ~ 0.6 eV above the E_F to K-optical A_1 phonons agreed with theoretical estimates

[Fig. 39(b)], as well as with the experimental value obtained from ultrafast electron diffuse scattering (Stern *et al.*, 2018).

In principle, this approach may find applications to a wide variety of quantum materials in which electrons are strongly coupled to a small number of bosonic modes and specific optical transitions are available. By monitoring quantized decay processes across the entire momentum space, this newly proposed method may allow the investigation of the microscopic origin and momentum dependence of the electron-boson coupling in quantum materials.

E. Summary and outlook

This section reviewed multiple TR-ARPES approaches for extracting the electron-phonon coupling strength, and more generally electron-boson coupling, in a variety of quantum materials. Although many of these methods could in principle provide quantitative estimates of electron-boson coupling, in practice interpreting the TR-ARPES signal unambiguously is often challenging (see Sec. II.B), thus hindering a precise estimate of electron-boson scattering processes. The development of advanced TR-ARPES experimental and analytical approaches, in combination with other ultrafast techniques, will be crucial for disentangling electron-boson scattering events by removing spurious contributions (such as transient changes of the scattering phase space, screening, and electronic distribution). We note that nearly all of the previously reviewed TR-ARPES studies rely on light excitations that are nonresonant to bosonic modes. That is, estimates of electron-boson coupling strength are obtained following extensive redistributions of the electronic density, which potentially changes the materials' state, such as its polarizability and screening. There is an opportunity for new studies at the forefront of the field to more quantitatively assess electron-boson processes in quantum materials by combining the previously discussed analysis procedures with selective excitation of collective modes.

VI. SURFACE PHOTOVOLTAGE

As mentioned in Sec. II.B, TR-ARPES provides access to the transient electronic spectral function as a function of energy, momentum, and time. For negative pump-probe delays, i.e., before the arrival of the pump excitation at the sample surface, the system is usually postulated to be in thermal equilibrium, so no dynamics are expected. According to this picture, the energy and momentum of the photoelectrons are fully determined at the moment of photoemission from the material, and any electronic dynamics in the sample left behind do not affect their propagation in vacuum. However, these assumptions do not remain valid if the arrival of the pump pulse on the material's surface induces a time-dependent electric field, as may occur in systems with spatially separated electron-hole pairs, such as semiconductors. This surface photovoltage (SPV) plays a crucial role in governing the efficiency of photoelectric devices. In a simplified description, the SPV can be understood in terms of a light-induced variation of the surface potential driven by the redistribution of photoexcited carriers affecting the intrinsic band bending. To the first approximation, the SPV manifests
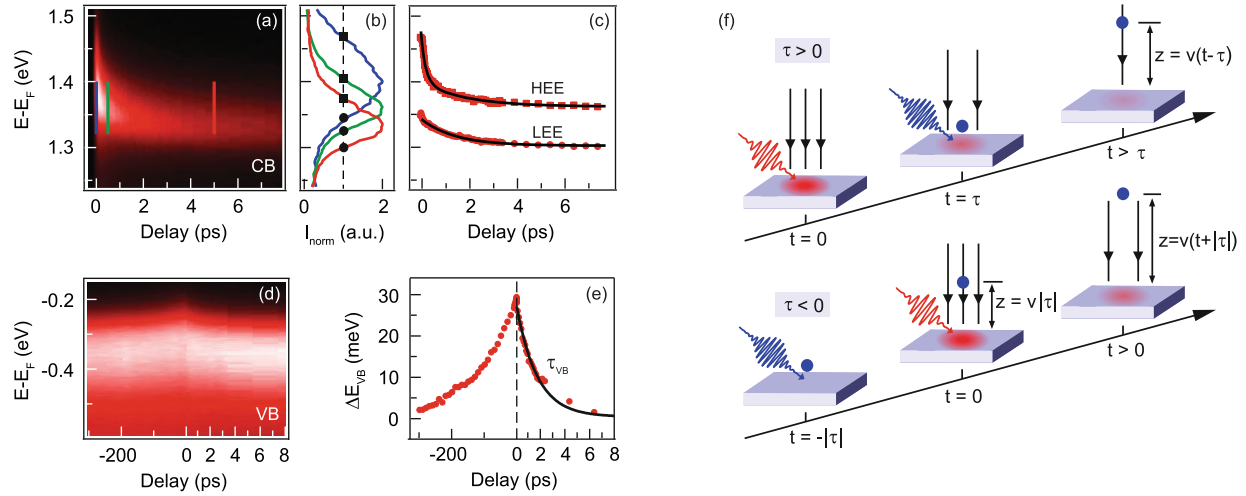
FIG. 40. Emergence of SPV in GaAs(110). (a) CB dynamics around the $\bar{\Gamma}$ point of p-type GaAs(110) upon ultrashort mid-IR optical excitation. (b) Normalized CB EDCs at 0 (blue line), 0.5 (green line), and 5 ps (red line). (c) Temporal evolution of the half-maximum point of the high-energy edge [(HEE), squares] and low-energy edge [(LEE), circles] of the EDC peak. (d) VB $\bar{\Gamma}$-EDC transient map and (e) energy shift dynamics. For both the CB and the VB the energy shift observed at positive delays can be described using double- or single-exponential fits: $\tau_{H1} = 200 \pm 20$ fs and $\tau_{H2} = 1.8 \pm 0.3$ ps for the HEE edge, $\tau_L = 1.4 \pm 0.1$ ps for the LEE edge, and $\tau_{VB} = 1.7 \pm 0.1$ ps for the VB. The shared $\sim$1.5 ps dynamics stem from the emergence of the pump-induced SPV, which also causes the additional upward shift of the VB at negative delays. (f) Schematic interpretation of the positive- and negative-delay dynamics in the presence of SPV, where the black lines perpendicular to the sample surface represent the SPV-induced electric field. Adapted from S.-L. Yang et al., 2014.

in the TR-ARPES data as a time-dependent rigid shift in the binding energy of the electronic band structure, whose direction depends on the direction of the light-induced surface electric field. Note that transient modifications of the surface potential may also result in changes in the confinement of surface states, as discussed in Sec. VI.B.

While SPV in conventional semiconductors had been extensively studied and exploited for many years (Marsi et al., 1997, 2000; Kronik and Shapira, 1999; Schroder, 2001; Widdra et al., 2003; Mönch, 2013), the role of SPV in the context of TR-ARPES measurements was not addressed theoretically until a decade ago (Tanaka, 2012). By systematically solving the classical equations of motion of photoelectrons from the sample's surface to the analyzer, Tanaka (2012) analyzed both the onset and the decay (i.e., at negative and positive delays) of the transient SPV, establishing the importance of considering the electron propagation. Following this theoretical work, various experimental TR-ARPES studies have addressed the SPV phenomenon and factored its effect into both data acquisition and analysis (Rettig, Kirchmann, and Bovensiepen, 2012; S.-L. Yang et al., 2014; Ciocys et al., 2019).

This section discusses the signatures of emerging SPV in TR-ARPES experiments, its implications for interpreting the data, and how SPV can ultimately be exploited to transiently manipulate macroscopic properties of quantum materials. We focus on two classes of materials: semiconductors and semimetals in Sec. VI.A and 3D topological insulators in Sec. VI.B.

A. Semiconductors and semimetals

Owing to their poor electronic screening, semiconductors are particularly sensitive to surface photovoltage. Focusing on

p-type GaAs(110) as the typical semiconductor model system, S.-L. Yang et al. (2014) first explored how SPV may manifest in a TR-ARPES experiment and outlined a basic framework to disentangle the system's intrinsic electronic dynamics from the transient field-induced features in the photoemission signal. Upon 1.5 eV pump excitation, both the VB and the optically occupied CB exhibit a transient energy shift at positive delays with similar relaxation times of $\sim$1.5 ps. Additional ultrafast dynamics are instead observed solely for the CB in the first 0.5 ps accompanied by a change of line shape; see Figs. 40(a)–40(c). While the latter timescale is attributed to the intraband CB electron-phonon scattering, the longer timescale dynamics shared by the CB and the VB are associated with the SPV driven by the downward band bending in a p-type semiconductor, which leads to a rigid shift of the entire band structure. Furthermore, in contrast with what can be expected in a system at equilibrium, an energy shift of the VB is also observed at negative delays (i.e., before pump excitation) lasting for hundreds of picoseconds, as shown in Figs. 40(d)–40(f). This kind of long-lasting preexcitation dynamics represents one of the main signatures of SPV in a TR-ARPES experiment, and it has been observed in different systems, such as the Kondo insulator SmB_6 (Ishida et al., 2015), graphene and black phosphorous (Ulstrup et al., 2015a; Hedayat, Ceraso et al., 2021), and various topological insulators; see Sec. VI.B. As a technical note, we mention that the SPV-induced negative-delay dynamics extending to hundreds of picoseconds may serve as a convenient tool to facilitate the routine operations of spatial and temporal overlap of the pump and probe beams on the sample surface, a crucial requirement for any TR-ARPES experiment.

To disentangle the contributions of different physical processes, S.-L. Yang et al. (2014) specifically included the propagation of photoelectrons through the SPV field in their
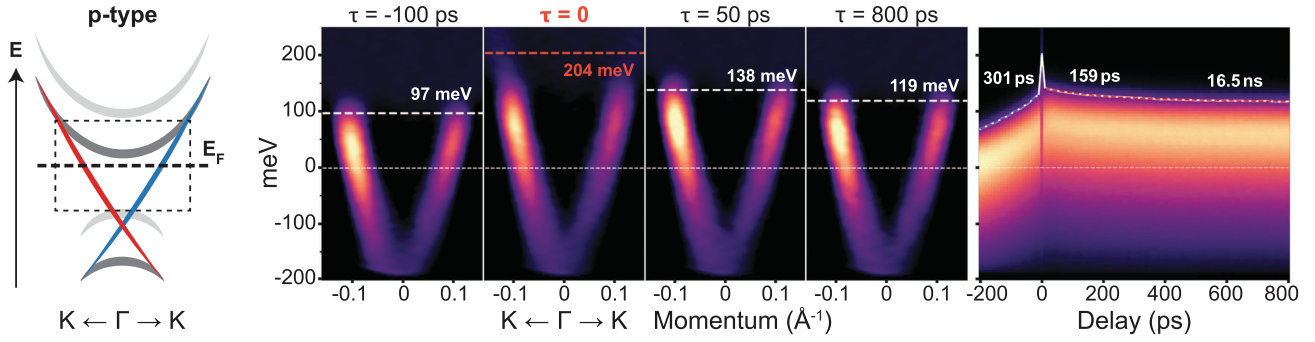
FIG. 41. Visualization of the effects of light-induced SPV in TR-ARPES data of p-doped Bi_2Se_3. The sketch on the left illustrates the topological surface state (red and blue) and bulk bands (gray) of p-doped Bi_2Se_3, where the Fermi level E_F lies within the bulk band gap. The ARPES spectra at different pump-probe delays highlight the shift of the chemical potential observed before and after the optical excitation due to the SPV effect. The far right panel shows the full dynamics of the momentum-integrated intensity along $K - \Gamma - K$. Adapted from Ciocys et al., 2020.

interpretation of TR-ARPES data of GaAs(110), which was in line with the theoretical work of Tanaka (2012). While for positive delays the pump-induced field is generated on the sample's surface before the electrons are photoemitted, thus affecting the entire length of their propagation in vacuum, for negative delays the photoelectrons travel a finite distance before the SPV field develops, leading to a signal that maps the spatial profile of the field.

Owing to its high carrier mobility and tunable band gap, black phosphorus represents a promising candidate for semiconducting devices, and its photovoltaic response was recently studied using TR-ARPES under chemical gating. In particular, Hedayat, Ceraso et al. (2021) and Kremer et al. (2021) showed that the strong surface electric dipole and the associated downward band bending induced by deposition of alkali atoms (such as K or Cs) can be fully compensated via illumination of the surface due to the emergence of SPV lasting on a timescale of nanoseconds. Two main SPV-induced effects are observed in the electronic structure at positive pump-probe delays: (i) a rigid energy shift affecting both the CB and the surface VB and (ii) a transient modification of the VB spectral line shape. The latter is caused by the SPV neutralization of the intrinsic band bending, which leads to bulk and surface VB contributions moving to similar binding energies. Therefore, in this scenario the dynamics of the VB bandwidth reflects the temporal evolution of the SPV probed by TR-ARPES: the linewidth narrows in the first picosecond, remains roughly constant over the next 60 ps, then slowly returns to its equilibrium value over ~1 ns.

Finally, the observation of SPV may reflect additional intrinsic phenomena and interactions of quantum materials. For example, in SmB_6, where topological surface states are predicted to emerge upon formation of a Kondo hybridization bulk gap, an SPV signal lasting >200 μs was detected only below the hybridization temperature 90 K, indicating the development of the surface band bending associated with the evolution of the hybridization gap itself (Ishida et al., 2015).

B. Topological insulators

As discussed in Sec. III.B, TR-ARPES has been extensively exploited to study the electronic response to ultrafast optical

excitations of both bulk and surface states of 3D topological insulators. SPV is one of the phenomena explored in relation to TIs, primarily in respect to electronic relaxation dynamics in bulk-insulating TIs. By comparing various p- and n-type Bi-chalcogenide TIs, Hajlaoui et al. (2014) showed how different surface band bendings spatially separate photoexcited electrons and holes and affect the interplay between surface and bulk state dynamics. Upon near-IR excitation, a large charge asymmetry is observed after a few picoseconds with an excess of holes in the surface states of the n-type sample due to a small upward band bending. In contrast, in p-type $Bi_{2.2}Te_3$ the preexisting downward band bending leads to an even greater excess of hot electrons in the Dirac cone. This charge disequilibrium has been suggested as the main cause of the long carrier relaxation time of >50 ps in $Bi_{2.2}Te_3$ and of the simultaneous transient shift of the chemical potential for 2D Dirac states as large as ~100 meV, which corresponds to half the equilibrium bulk gap (Hajlaoui et al., 2014). Similarly, Ciocys et al. (2020) observed a long-lasting (~10 ns) SPV in n-doped Bi_2Te_3 and p-doped Bi_2Se_3 compounds upon near-IR excitation. Ciocys et al. (2020) employed a large pump-probe delay range (for both negative- and positive-delay values) to reveal the full intrinsic timescale of SPV in the TIs. As shown in Fig. 41, TR-ARPES mapping of p-doped Bi_2Se_3 reveals a shift of the chemical potential at negative delays with a ~300 ps timescale, induced by the interaction between photoelectrons and the SPV-driven electric field at the sample's surface (as discussed in Sec. VI.A for semiconductors), whereas at positive delays this effect persists on a nanosecond timescale. These results demonstrate that examining a large pump-probe delay range is essential to extract the intrinsic formation and decay timescales of the SPV. A narrow time range may preclude detection of the full negative-delay dynamics and incorrectly suggest that the negative-delay shift of the chemical potential arises primarily as a buildup effect from previous pump pulses, thus leading to inaccurate estimates of the SPV lifetime.

A significant rigid shift of the chemical potential μ has also been observed for bulk-insulating ternary TIs driven by the emergence of a large SPV (Neupane et al., 2015; Sánchez-Barriga, Battiato et al., 2017; Sumida et al., 2017; Papalazarou et al., 2018; Yoshikawa et al., 2018, 2019).
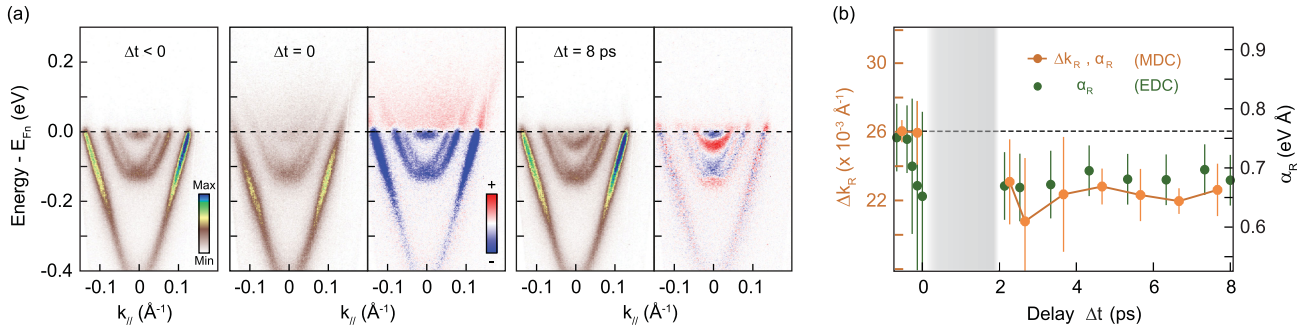
FIG. 42. SPV as a tuning knob of the Rashba spin-orbit coupling of a 2D electron gas at the surface of Bi_2Se_3. (a) ARPES dispersion at negative time delay (before pump arrival), at time zero (with pump and probe fully overlapped), and at 8 ps delay after the excitation. The differential spectra (obtained by subtracting the spectrum acquired at −0.5 ps) are also shown for the zero and positive delays. An observable time-dependent energy shifts of the QWSs at the Brillouin zone center is induced by the emergence of SPV. (b) Transient evolution of the Rashba spin-orbit coupling strength α_R in the first QWS as extracted by fitting momentum (orange) and energy (green) splitting of Rashba subbands at several time delays. Adapted from Michiardi et al., 2022.

In Bi_2Te_2Se the shift of μ due to the SPV reaches a quasistatic value of ~100 meV after 100 ps and subsequently relaxes on a long timescale far exceeding 4 μs (Neupane et al., 2015). The same timescale characterizes the SPV observed at both room and low temperature for the $x = 0.55$ compound of the $Bi_{1-x}Sb_xTe_3$ series (Sánchez-Barriga, Battiato et al., 2017; Sumida et al., 2017). In both cases this long-lasting SPV is linked to the much longer relaxation lifetime of the Dirac surface states with respect to the bulk bands, as both phenomena are affected by the different diffusion rates of hot carriers in the surface and bulk bands in the case of a truly bulk-insulating TI. In this respect, Papalazarou et al. (2018) discussed the role of surface defects rather than laser-induced band bending in creating charge carrier separation after reporting a temperature-dependent change of the sign of the SPV in Bi_2Te_2Se. According to this interpretation, special defects on the cleaved surface (such as donor-type vacancies) may change the charge density in the topmost layers, leading to a near-surface electrostatic potential that confines photo-excited holes into the bulk. The observed SPV would then be induced by impurity states lying within the bulk energy gap.

Recently a few TR-ARPES studies on the emergence of SPV have addressed the possibility of optically generating spin-polarized currents on the surface of a TI, owing to the helical texture of the topological surface state. Such an avenue is promising in the context of potential spintronics applications, where active control of the electrons' degree of freedom is required. Ciocys et al. (2022) and Michiardi et al. (2022) demonstrated how light-induced SPV and charge redistribution can be utilized to manipulate the intrinsic material's spin properties. Michiardi et al. (2022) in particular analyzed the spectroscopic response to optical pumping of the Rashba-split quantum well states (QWSs) generated at the surface of Bi_2Se_3 via a deposition of alkali atoms. As a typical fingerprint of the Rashba effect, these states consist of spin-polarized electronic bands that are offset in momentum and whose splitting is directly related to the strength of the Rashba spin-orbit coupling in the system α_R. Upon near-IR excitation, a transient modification of the QWSs' binding energy was observed on a picosecond timescale, whereas the topological surface state did not exhibit any significant change, as shown

in Fig. 42(a). This distinctive long-lasting response of the QWSs translates into a transient decrease of the splitting in both energy and momentum of the Rashba subbands and, consequently, of the intrinsic spin-orbit coupling strength α_R. The latter was found to decrease by as much as 15% over hundreds of picoseconds [Fig. 42(b)]. Michiardi et al. (2022) ascribed the observed phenomena to a pump-induced SPV: following the optical excitation, excess negative charge accumulates at the surface, softening the original downward band bending, which in turn significantly affects the dispersion of the QWSs [similar to what has been observed in thin epitaxial Pb films on Si(111) (Rettig, Kirchmann, and Bovensiepen, 2012)] while shifting the more surface-localized topological surface state in a more rigid fashion.

Another recent TR-ARPES study on α-GeTe(111) showed an ultrafast enhancement of the Rashba coupling mediated by SPV in tandem with ion displacement, deduced by tracking the transient energy shift of the bulk bands; see Sec. V.B (Kremer et al., 2022). The emergence of SPV prompts the excitation of displacive coherent phonons, thus ultimately controlling the ferroelectric properties of the α-GeTe(111) system. These results attest to the potential of the TR-ARPES technique not only to test and characterize the SPV effect in quantum materials but also to exploit this phenomenon to optically manipulate their physical properties, including the spin character, for future optically controlled spintronics devices.

C. Summary and outlook

Research conducted over the past decade has provided a strong description of the signatures of SPV in the context of TR-ARPES, and we believe that dynamic SPV effects are now well characterized and understood. Design and analysis of TR-ARPES measurements require a thoughtful consideration of SPV effects as they can be an important factor in understanding TR-ARPES data. Moreover, SPV also represents an opportunity to expand our optical control approaches to quantum materials, as recent TR-ARPES experiments have demonstrated the possibility of exploiting it as a means to transiently manipulate the electronic and magnetic properties

of topological insulators and Rashba-split systems. Ongoing technical improvements to the laser sources and ARPES systems will enable detection of smaller SPV effects, enabling this methodology to evolve into a fine-tuning knob supporting novel technological applications.

VII. SPIN TEXTURES AND THEIR DYNAMICS

Electron spin and its interactions with other degrees of freedom (such as spin-orbit coupling) often play a significant role in determining a material's electronic structure, from topological insulators (Cao *et al.*, 2013; Zhu *et al.*, 2013) to high-temperature superconductors (Gotlieb *et al.*, 2018). Experimentally accessing these interactions is essential for reaching a deeper understanding of the physical properties of quantum materials, as well as to advance the growing field of spintronics technology. The development and inclusion of spin polarimeters (either Mott or very-low-energy electron diffraction scattering detectors) in conventional ARPES systems, in concert with the use of the optical selection rules of helical light to excite and probe spin-orbital entangled states (dichroism), have created the foundation to study the spin texture of the electronic bands directly in momentum space. Accessing the spin degree of freedom via ARPES is far from straightforward: for instance, spin-resolved ARPES has been challenged by the limited efficiency of spin polarimeters, and the link between the spin order and the dichroic signal is not at all direct. Nevertheless, interest in studying spin interactions has driven efforts to develop combined spin-resolved and dichroism-based time-resolved ARPES approaches able to access not only the spin character of the electronic bands but also the dynamical role played by the spin degree of freedom in the electronic relaxation processes following an optical excitation.

This section reviews how TR-ARPES has been adapted to gain insights into the spin degree of freedom of various quantum materials, beginning with the achievements of the spin-resolved TR-ARPES technique in Sec. VII.A, focusing on research into ferromagnetic materials and topologically protected systems. Next Sec. VII.B highlights how dynamical information about the spin may be obtained via analysis of the transient dichroic signal generated by utilizing different pump or probe polarizations. Finally, Sec. VII.C reviews how the capabilities of TR-ARPES can be instrumental in furthering our understanding of phases with spin-driven order in quantum materials.

A. Spin-resolved TR-ARPES

The advent of spin-resolved TR-ARPES (Cinchetti *et al.*, 2006; Melnikov *et al.*, 2008; Gotlieb *et al.*, 2013; Nie *et al.*, 2019; Fanciulli *et al.*, 2020; Fukushima *et al.*, 2023) has led to pioneering investigations of the transient evolution of the spin order of quantum materials upon light excitation. Despite significant advances in the efficiency of modern spin polarimeters, spin-resolved TR-ARPES remains a highly complex technique and requires long integration times. Consequently, most spin-resolved TR-ARPES studies have focused on extracting the transient spin dynamics for just one or at most a few momentum points. Section VII.A.1

shows how spin-resolved TR-ARPES has helped to investigate the physical mechanisms underlying the ultrafast demagnetization process in ferromagnetic metals, while Sec. VII.A.2 focuses on recent work on ultrafast spin dynamics in the surface resonant state and topological surface state of 3D topological insulators.

1. Ferromagnetic materials

Since it was first observed experimentally in nickel (Beaurepaire *et al.*, 1996), the light-induced ultrafast demagnetization of ferromagnets has interested the scientific community. Various proposals have been put forward for its underlying mechanism, from electron-magnon scattering (Carpene *et al.*, 2008) to spin-lattice Elliott-Yafet events (Koopmans *et al.*, 2010) and superdiffusive currents (Battiato, Carva, and Oppeneer, 2010). Most of the experimental efforts investigating ultrafast demagnetization processes in magnetic systems have historically relied on all-optical probes, such as magneto-optical Faraday and Kerr effects, second harmonic generation at the interface, and x-ray magnetic circular dichroism (Kirilyuk, Kimel, and Rasing, 2010). Although all-optical probes can easily retrieve demagnetization timescales and amplitudes, they lack the momentum resolution needed to track the evolution of the spin polarization of specific electronic states.

By combining time-resolved high-harmonic ARPES and magneto-optical probes, Tengdin *et al.* (2018) and You *et al.* (2018) showed that light-induced spin excitation in Ni actually occurs on a ~20 fs timescale, which is far faster than previously thought. By tracking the transient electronic temperature via fitting the ARPES spectra to a Fermi-Dirac distribution [Figs. 43(a) and 43(b)], they revealed a critical behavior associated with a critical laser fluence (F_c) that is needed to drive the electronic temperature above the Curie temperature. As displayed in the top panel of Fig. 43(c), as the laser fluence approaches F_c the energy gained by the electron bath is reduced due to the transfer of energy to the spin bath on ultrafast <20 fs timescales. A related critical behavior is highlighted by the bottom panel of Fig. 43(c), showing that the persisting collapse of the exchange splitting to longer timescales (>2 ps) [as extracted by the ARPES maps, Fig. 43(a)] occurs only for fluences above F_c. Therefore, while the spin bath can absorb a sufficient laser pump pulse via high-energy spin excitations to store the magnetic energy (and subsequently proceed through a magnetic phase transition), the demagnetization and collapse of the exchange splitting occur on much longer (~200 fs) timescales [see Fig. 43(d)] after the magnon population has equilibrated. These findings connect the light-induced out-of-equilibrium magnetic state to the equilibrium ferromagnetic-to-paramagnetic phase transition that occurs at the Curie temperature in Ni, showing that the electronic temperature alone dictates the magnetic response in this single-element material.

In another study, Eich *et al.* (2017) showed that the ultrafast quenching of the magnetization in another 3d ferromagnet, Co/Cu(001), cannot be explained by a reduction of the exchange splitting. Instead, they ascribed the observed ultrafast demagnetization process to efficient emission of magnons as the leading underlying mechanism. This emission of magnons would be associated with fluctuating spin-split
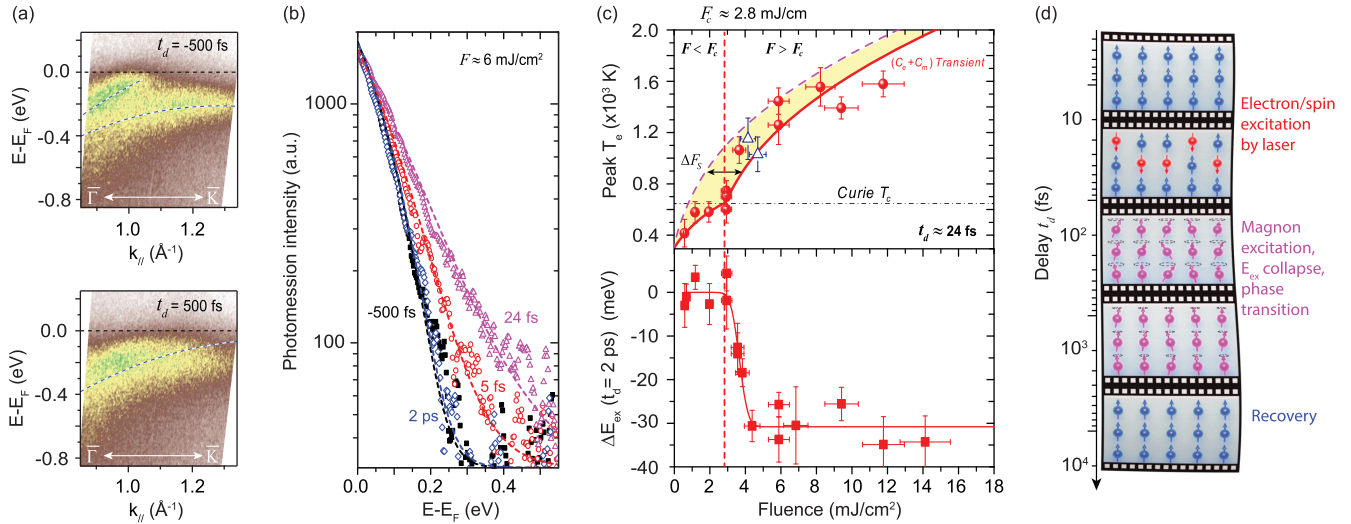
FIG. 43. Critical phenomena connecting the ultrafast demagnetization in ferromagnetic Ni to the equilibrium magnetic phase transition. (a) TR-ARPES spectra of Ni(111) along the $\Gamma - K$ direction before (-500 fs) and after (500 fs) laser excitation, highlighting the transient reduction of the exchange splitting ΔE_{ex}. (b) Momentum-integrated EDCs on a logarithmic scale at different pump-probe delays at ~ 6 mJ/cm^2 pump fluence. The electronic temperature, extracted by fitting momentum-integrated EDCs to a Fermi-Dirac distribution, reaches its maximum within ~ 24 fs after the optical excitation. (c) Top panel: maximum electronic temperature at 24 fs pump-probe delay as a function of the pump fluence. The yellow region highlights the energy transferred to the spin bath (ΔF_S) within ~ 20 fs. Bottom panel: ΔE_{ex} at 2 ps pump-probe delay as a function of the pump fluence. The two panels report a similar critical fluence $F_c \approx 2.8$ mJ/cm^2. (d) Schematic of the light-induced demagnetization process of Ni. Upon a femtosecond pump excitation, the transient electronic temperature approaches and can surpass the Curie temperature within 20 fs, which induces high-energy spin excitations, which store the magnetic energy. Demagnetization occurs later, in ~ 175 fs, driven by relaxation of nonequilibrium spins and the likely excitation of low-energy magnons. Full recovery of the spin system occurs within ~ 0.5–100 ps, depending on the laser fluence. Adapted from Tengdin et al., 2018.

electronic states, which result in a folding of states of different spins one on top of the other. Despite more TR-ARPES studies on $3d$ (Scholl et al., 1997; Rhie, Dürr, and Eberhardt, 2003; Schmidt et al., 2010; Weber et al., 2011; Fognini et al., 2014; Gort et al., 2018) and $4f$ ferromagnets (Lisowski et al., 2005; Carley et al., 2012; Frietsch et al., 2020), which have successfully probed the ultrafast dynamics of spin polarization or exchange splitting for a specific momentum upon light perturbation, further research is needed to completely unravel the microscopic mechanism and to reach a comprehensive description of the ultrafast demagnetization effect.

2. Topologically protected systems

Topological systems such as topological insulators or Weyl semimetals host topologically protected states with characteristic spin textures (Hasan and Kane, 2010; Cao et al., 2013; Zhu et al., 2013; Yan and Felser, 2017). The unique capabilities of spin-resolved TR-ARPES allow unoccupied spin-polarized states to be assessed and ultrafast carrier relaxation processes to be tracked with spin resolution. Cacho et al. (2015), followed by Jozwiak et al. (2016), employed spin-resolved TR-ARPES to map a topologically trivial spin-polarized surface resonance state (SRS) within the unoccupied bulk conduction band of the prototypical 3D topological insulator Bi$_2$Se$_3$. Figure 44(a) compares measured and calculated spin-resolved EDCs, hinting at the presence of the SRS ~ 0.4 eV above the Fermi level (Cacho et al., 2015). A direct visualization of the SRS spin polarization is given in

the spin-resolved TR-ARPES map of Fig. 44(b), which confirms the presence of the SRS, characterizes its dispersion, and also reveals that its spin polarization is the opposite of that of the TSS (Jozwiak et al., 2016). Subsequent spin-resolved TR-ARPES experimental studies have also verified the presence of additional SRSs in the unoccupied bulk band gaps of Bi$_2$Te$_3$ (Sánchez-Barriga et al., 2017). Spin-resolved TR-ARPES was recently employed to reveal the spin polarization of electrons bound into a spatially indirect topological exciton in Bi$_2$Te$_3$, as discussed in Sec. III.C and shown in Fig. 16(b).

Spin-resolved TR-ARPES can also characterize the transient evolution of the spin polarization of the light-injected electron population. Jozwiak et al. (2016) demonstrated that the spin polarization of the SRS does not evolve with time, ensuring that the spin-resolved spectrum of Fig. 44(b) directly reflects the intrinsic spin polarization of the SRS rather than a pump-induced selective occupation of those states. Indeed, if the transiently occupied states were spin unpolarized, such a population would tend to depolarize on a subpicosecond timescale (Hsieh et al., 2011), whereas the SRS in Bi$_2$Se$_3$ retains the same polarization during the entire relaxation process. However, note that the use of tailored optical excitation may transiently alter the polarization of carriers injected into a final state. As an emblematic example, Sánchez-Barriga et al. (2016) reported a ~ 1 ps decay time for the transient out-of-plane spin polarization of electrons excited into the topological surface state of p-doped Sb$_2$Te$_3$ upon circular near-IR excitation. They not only demonstrated

light control of the out-of-plane spin polarization of carriers photoinjected into the TSS, but the vanishing of the out-of-plane spin polarization on a picosecond timescale also hints at an inefficient depolarization mechanism via electron-phonon scattering.

Finally, a recent spin-resolved XUV-based TR-ARPES study addressed the spin polarization of the unoccupied states of the putative Weyl type-II semimetal WTe_2, in which Weyl points are predicted above the Fermi level (Fanciulli *et al.*, 2020). Although unable to clearly capture the presence of such Weyl points from the spin-polarized spectra, Fanciulli *et al.* (2020) reported a spin-selective bottleneck effect at 1 ps in the region above their expected energy. This observation points toward a reduction of the available scattering phase space due to a defined spin texture of the unoccupied states, thus supporting the topological nature of WTe_2.

B. Dichroic TR-ARPES

Although spin-resolved ARPES directly measures the spin degree of freedom by employing spin polarimeters, it confronts an intrinsic challenge of low efficiency due to the small spin-dependent scattering cross section. One way to partially work around this challenge relies on the fact that the photoemission process is essentially an optical transition between an initial and a final state, so the ARPES signal depends on the polarization of the incoming light via the matrix element term. Analyzing the difference in the photoemission signal acquired with different light polarizations (both linear and circular), also known as the dichroic signal, can provide insight into the symmetry of the initial state wave function. The polarization of the incoming light becomes a tunable parameter to selectively couple to electronic states of different total angular momentum (or *pseudospin*) quantum number. Although in the case of spin-orbit coupled systems the dichroic signal may resemble the underlying spin texture as an indirect consequence of optical selection rules related to the orbital angular momentum of electronic states, the connection between dichroism and spin order of the initial states is not straightforward, and its interpretation may be further complicated by the symmetry of the final photoemission states.

Since TR-ARPES employs two separate light pulses, it is necessary to distinguish the cases of dichroic signals produced by differently polarized pump pulses versus probe pulses. The latter is the transient counterpart of static dichroic ARPES (Wang and Gedik, 2013; Beaulieu *et al.*, 2020; Schüler *et al.*, 2020, 2022; Sobota, He, and Shen, 2021; Moser, 2023) and has been applied mainly to the study of topological insulators (Hedayat, Bugini *et al.*, 2021; Zhang *et al.*, 2021) and Rashba materials (Mauchain *et al.*, 2013; Zhang *et al.*, 2023). As mentioned, linear or circular probe dichroic photoemission signals can offer information on whether the initial or final photoemission states have a well-defined spin or orbital angular momentum. Therefore, when applied to materials with strong spin-orbit coupling or spin-momentum locking, circular probe TR-ARPES dichroism may offer a qualitative mapping of the underlying spin texture of unoccupied states and their related spin dynamics. However, a detailed interpretation of the TR-ARPES signal acquired with a dichroic probe is often a
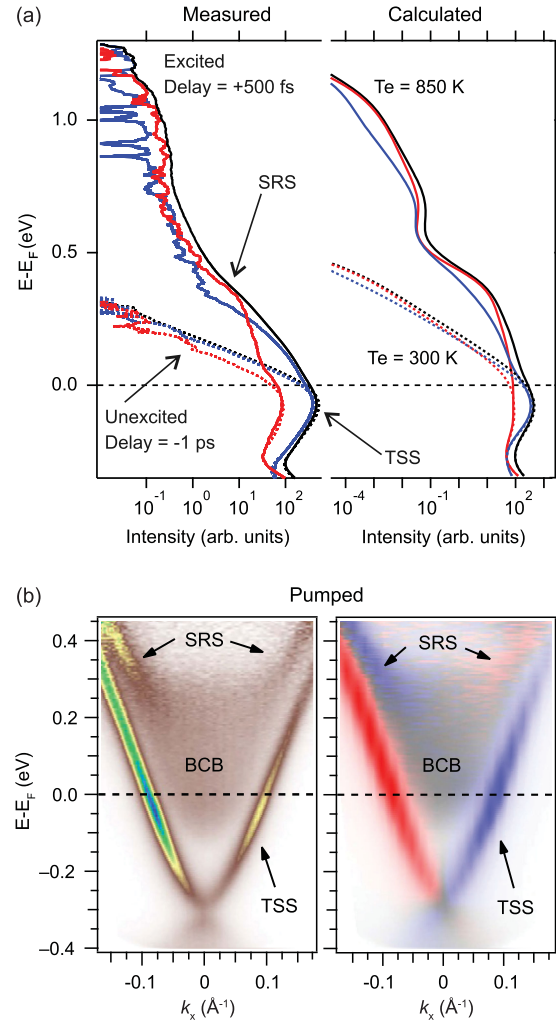

FIG. 44. Transient mapping of the spin-resolved surface resonance state (SRS) in Bi_2Se_3. (a) Measured and calculated spin-resolved EDCs along the $\Gamma - K$ direction close to the TSS. Dotted (continuous) lines indicate opposite spin-resolved photoemission intensities before (after) the optical excitation, while TSS and SRS are indicated by arrows. Adapted from Cacho *et al.*, 2015. (b) Spin-integrated and spin-resolved ARPES maps (left and right panels, respectively) along the $\Gamma - K$ direction at 0.7 ps pump-probe delay upon near-IR excitation. Adapted from Jozwiak *et al.*, 2016.

challenging undertaking (as is its equilibrium counterpart). Indeed, such a task requires the ability to unambiguously disentangle whether the evolution of the circular probe dichroic signal arises from transient changes of the spin or orbital contributions to the wave function of both the initial and final photoemission states. This also involves the evaluation of potential changes in the photoemission matrix elements (Boschini *et al.*, 2020a), which are not associated with any modifications of the spin polarization itself. For this reason, the following discussion focuses solely on TR-ARPES studies performed with dichroic pump excitation in which changes in the dichroism asymmetry can be directly related to the selective photoexcitation of polarized electrons.

TMDs exemplify the potential of the pump-dichroic TR-ARPES technique. As mentioned in Sec. III.A while
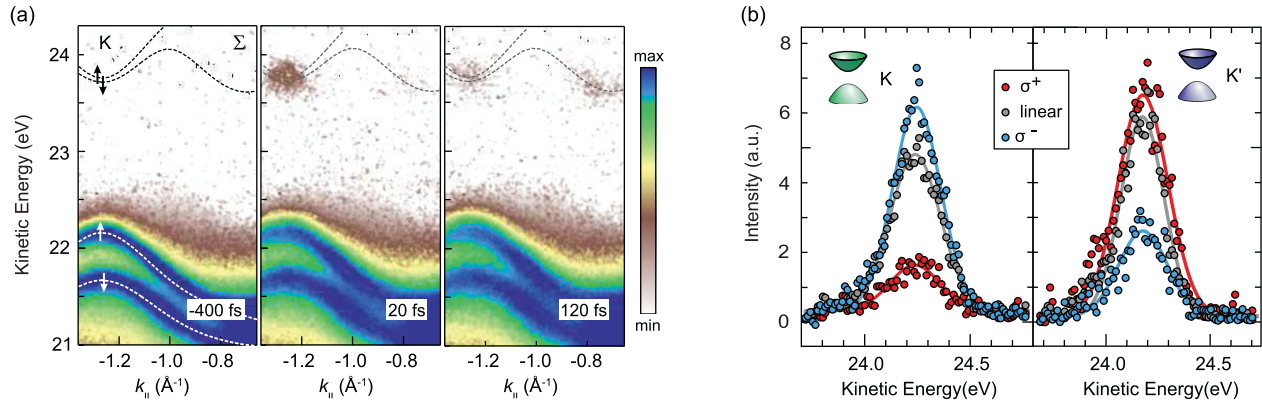
FIG. 45.   Selective population of the K or K' valley of $2H$-WSe$_2$ upon circularly polarized optical excitation. (a) TR-ARPES maps at various pump-probe delays acquired with linearly polarized pump pulses (logarithmic color scale). The dashed lines display the VB and CB dispersions obtained by DFT calculations for a bilayer compound, with the CB shifted 250 meV upward to match the experimental observations. (b) Energy distribution curves of the excited state signal at K and K' 15 fs after excitation with a linearly and a circularly polarized optical pump. Note the strong valley selectivity attainable by excitation with circularly polarized light. Adapted from Bertoni *et al.*, 2016.

discussing their unoccupied band structure, the two-atom basis and the breaking of inversion symmetry in TMDs lead to the inequivalence of two adjacent K points, commonly identified as the K and K' valleys. Of particular importance, electrons in the CB and the VB have different azimuthal quantum numbers (m): $m_{VB} = 0$ and $m_{CB} = \pm 1$ at K and K', respectively (Cao *et al.*, 2012). Therefore, right (left) circularly polarized light can promote only K (K') transitions, prompting the chiral optical selection rule of TMDs between two bands sharing the same spin. Pump-dichroic TR-ARPES has verified this selection rule on bulk $2H$-WSe$_2$ (Bertoni *et al.*, 2016), monolayer WS$_2$ (Ulstrup *et al.*, 2017; Beyer *et al.*, 2019; Kunin *et al.*, 2023), and bilayer MoS$_2$ (Volckaert *et al.*, 2019). Figure 45(b) displays the different photoemission signals acquired at K and K' upon pump pulses of different polarizations in bulk $2H$-WSe$_2$, thus demonstrating that circularly polarized optical excitations drive a layer-dependent valley-polarized population (Bertoni *et al.*, 2016). The pump-induced K and K' valley populations decay on a 100 fs timescale into the Σ valley (i.e., the global CB minimum), as shown in the TR-ARPES maps of Fig. 45(a). Moreover, by investigating singly oriented monolayer WS$_2$ on Ag(111), Beyer *et al.* (2019) reported a light-induced valley polarization of ~85% for the top of the VB and only ~55% for the bottom of the CB. This discrepancy of the valley polarization between the initial and final optical states was understood in terms of a difference in the efficiency of K and K' intervalley scattering for the CB and the VB (for the latter, the large spin-orbit split mitigates intervalley scattering events). These examples show how circular pump light may be utilized to prepare the excited state with a well-defined spin-valley polarization, thus enabling TR-ARPES to track scattering processes involving specific polarized carriers.

In addition to TMDs, 3D topological insulators were among the first systems to which pump-dichroic TR-ARPES was applied due to the characteristic spin texture of their topological surface state. Kuroda *et al.* (2017) investigated linear and circular photogalvanic effects due to polarization-variable mid-IR excitation on the topological surface state of Sb$_2$Te$_3$.

Relying on the selective population of electronic states with opposite pseudospins, Niesner *et al.* (2012) first reported the presence of a spin-polarized second surface state in the unoccupied band structure of Bi$_2$Se$_3$, and this observation was then confirmed via 6 eV two-photon photoemission (Sobota *et al.*, 2013, 2014b). Subsequent TR-ARPES studies with circular optical excitation showed a population asymmetry in this second surface state as a function of the different pump polarizations (Bugini *et al.*, 2017; Soifer *et al.*, 2019). The observed dichroic signal has been proposed to be related to an ultrafast spin-polarized surface current, although its intrinsic depolarization time is under 50 fs.

C. Spin-density-wave gaps

Even without the use of spin polarimeters or dichroic signals to extract spin textures and dynamics, TR-ARPES can provide insight into spin-ordered phases. In analogy with the approach used to track the charge-order spectral gap (see Sec. IV.A), light-induced modifications of electronic gaps mediated by spin-density waves (SDWs) may offer direct insight into the transient evolution of underlying spin orders (Rettig *et al.*, 2012; Nicholson *et al.*, 2016; Suzuki *et al.*, 2017; Boschini *et al.*, 2020b). Nicholson *et al.* (2016) demonstrated this concept by tracking the dynamics of the antiferromagnetic order parameter in Cr(110) and relating it to the transient evolution of the electronic temperature. They suggested that the photoexcited electrons form a quasiequilibrium state with spin order, thus allowing the use of thermodynamic concepts even on ultrafast timescales.

Along the same lines, Boschini *et al.* (2020b) tracked the transient filling of the SDW gap at the antiferromagnetic hot spot of the optimally doped Nd$_{2-x}$Ce$_x$CuO$_4$ (NCCO) electron-doped cuprate; see Fig. 46(a). Although optimally doped NCCO does not exhibit any long-range magnetic order, it is characterized by a short-range antiferromagnetic order with a spin-correlation length that decreases with temperature. For this reason, the SDW-mediated electronic gap at the antiferromagnetic hot spot is only partial, and it is often referred to as the pseudogap (PG) (Armitage *et al.*, 2001).
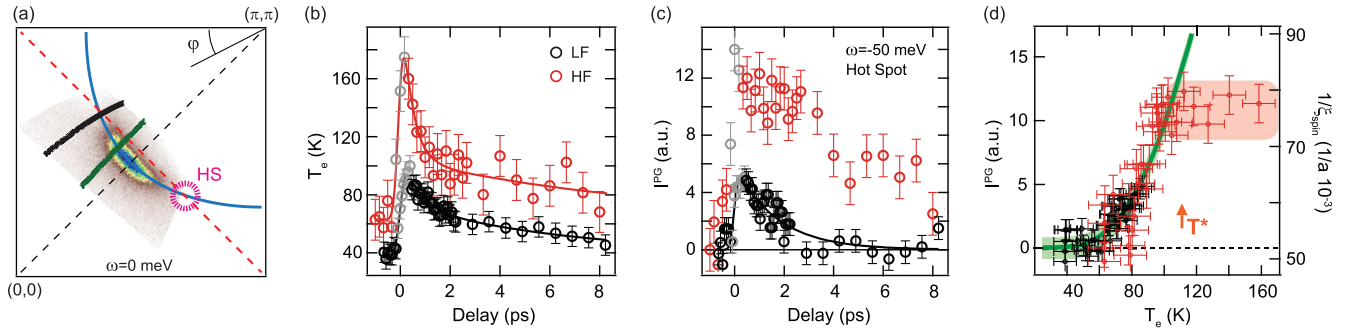
FIG. 46. Tracking the filling of the pseudogap driven by the shortening of the spin-correlation length in the optimally doped $Nd_{2-x}Ce_xCuO_4$ electron-doped cuprate. (a) Experimental Fermi surface measured with 6.2 eV at 10 K. The blue solid line is a tight-binding constant energy contour at $\omega = 0$ meV, the red dashed line marks the antiferromagnetic zone boundary, and the violet dotted circle indicates the hot-spot (HS) position. The green and black solid cuts mark the two momentum directions explored in the study: near node and HS. (b) Transient electronic temperature extracted by fitting the Fermi edge broadening along the near-nodal direction for two pump-fluence regimes: low fluence (LF) and high fluence (HF). The gray points indicate time delays for which a pure thermal fitting is not accurate. (c) Temporal evolution for both LF and HF of the photoemission intensity at the HS for $\omega = 50 \pm 10$ meV, which represents the evolution of the pseudogap. (d) Photoemission intensity at the HS for $\omega = 50 \pm 10$ meV as a function of the electronic temperature (the black and red circles for LF and HF, respectively). The green line and shadow represent the inverse of the spin-correlation length ξ_{spin} from neutron scattering studies. Saturation of the photoemission intensity at the HS (red shadow) marks the temperature T^* at which a complete filling of the PG is observed. Adapted from Boschini *et al.*, 2020b.

Boschini *et al.* (2020b) employed TR-ARPES to map the transient modifications of the PG spectral feature into an effective temperature evolution, revealing a filling rather than a closing of the PG with increasing temperature, as shown in Figs. 46(b)–46(d). This result recalls the case of the superconducting gap in hole-doped cuprates. Whereas in those systems the quenching of phase coherence drives the filling of the superconducting gap (see Sec. IV.D), in electron-doped NCCO the filling of the SDW gap is instead associated with the temperature evolution of the spin-correlation length [the green line and shadow in Fig. 46(d)]. The PG is completely filled at the crossover temperature T^*, for which the spectral broadening driven by a reduction in spin-correlation length overcomes the PG amplitude. Boschini *et al.* (2020b) provided direct evidence for the primary role of short-range antiferromagnetic correlations in determining the partial suppression of spectral weight at the hot spots in electron-doped cuprates and showcased the transient tracking of SDW gap amplitude or filling as a reliable approach to retrieve information about the long- and short-range spin orders.

D. Summary and outlook

In summary, extensive technical and analytical advances of the TR-ARPES technique over the past two decades have finally unlocked investigations of the spin degree of freedom directly in momentum space. This section reviewed how TR-ARPES has been adopted in different ways to gain such information, from the spin-resolved fashion to the analysis of transient dichroic signals and the tracking of spin-order-induced electronic gaps. While each of these approaches faces challenges and limitations (such as low detector efficiency and arduous data analysis), TR-ARPES has the potential to expand our understanding of the role of electronic spins in defining the properties of quantum materials far beyond what can be learned from equilibrium ARPES. Looking ahead, the advent of momentum microscopes

with two-dimensional spin filtering (Tusche, Krasyuk, and Kirschner, 2015; Kutnyakhov *et al.*, 2016) promises new insights into spin dynamics of quantum materials and spintronic devices.

VIII. CONCLUDING REMARKS

TR-ARPES has emerged as one of the most powerful tools for investigating dynamical properties of quantum materials, as exemplified by the scientific achievements presented in this review. Although TR-ARPES has relied primarily on optical excitation in the near-IR–visible spectral range at its early stages, it nonetheless has offered interesting insights into electron dynamics and light-induced manipulation of the electronic band structure with momentum resolution in disparate quantum materials, ranging from high-temperature superconductors (Perfetti *et al.*, 2007; Smallwood, Hinton *et al.*, 2012; Boschini *et al.*, 2018) to charge-ordered systems (Schmitt *et al.*, 2008; Rohwer *et al.*, 2011), as well as topological systems (Crepaldi *et al.*, 2012; Hajlaoui *et al.*, 2012; Sobota *et al.*, 2012; Wang *et al.*, 2012) and monolayer transition-metal dichalcogenides (Grubišić Čabo *et al.*, 2015). In recent years, advances in the generation of mid-IR–terahertz pulses and the use of momentum microscopes have enabled the observation of Floquet-Bloch states (Wang *et al.*, 2013; Ito *et al.*, 2023; Zhou *et al.*, 2023), terahertz-driven currents (Reimann *et al.*, 2018), and bright and dark excitons in micrometer-sized exfoliated transition-metal dichalcogenides (Madéo *et al.*, 2020; Dong *et al.*, 2021; Karni *et al.*, 2022; Schmitt *et al.*, 2022), thus inspiring development of next-generation TR-ARPES systems and advances in theoretical analysis of TR-ARPES data. Since this panoramic review has covered what the TR-ARPES technique has accomplished to date, we now offer a forward-looking view of what we believe will be the new frontiers of TR-ARPES in the coming years, focusing on five different ongoing or
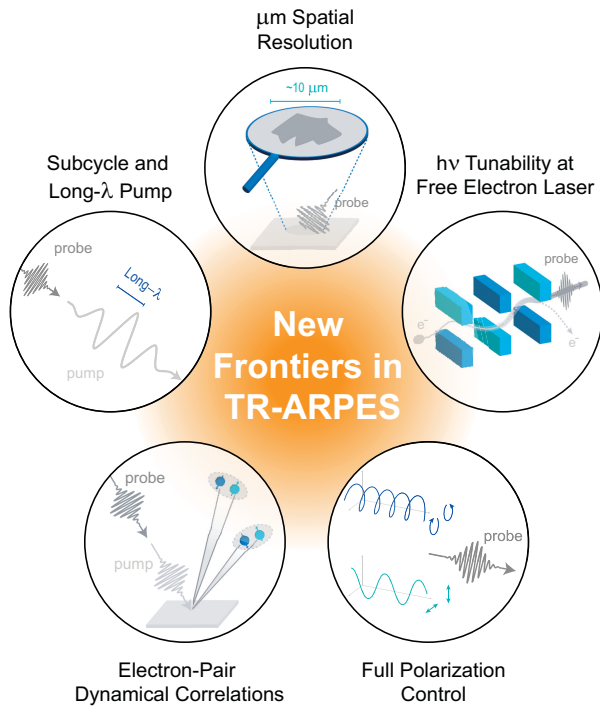
FIG. 47. Illustration of the forthcoming new frontiers of the TR-ARPES technique in the coming years.

anticipated advancements that we expect to mature over the next decade (summarized in Fig. 47).

Subcycle and long-wavelength-pump TR-ARPES. In recent years, advances in the generation of pump pulses in the mid-infrared-to-terahertz range have enabled electron dynamics to be tracked beyond the conventional near-infrared excitation scheme (Gierz *et al.*, 2013; Kuroda *et al.*, 2016, 2017; Chávez-Cervantes *et al.*, 2019), such as the observation of Floquet-Bloch states (Wang *et al.*, 2013; Mahmood *et al.*, 2016; Reutzel *et al.*, 2020; Aeschlimann *et al.*, 2021; Ito *et al.*, 2023), as well as the first terahertz-pump TR-ARPES work on topological insulators (Reimann *et al.*, 2018). Furthermore, the seminal papers of Reimann *et al.* (2018) and Ito *et al.* (2023) demonstrated the capability of tracking light-matter interaction processes with subcycle resolution, thus opening the way for subcycle TR-ARPES to explore highly out-of-equilibrium processes. We expect the TR-ARPES community to continue to advance tunable and intense long-wavelength pump sources (for example, $\lambda > 4\ \mu m - h\nu < 300$ meV) to coherently excite collective modes and drive the emergence of new phases of matter with no equilibrium counterpart. Ideally we contemplate TR-ARPES experiments where the pump excitation does not couple to the electronic bath at all but instead launches collective excitations, which in turn modify and renormalize the single-particle dispersion.

TR-ARPES with micrometer spatial resolution on exfoliated and stacked or twisted materials. The recent development of TR-ARPES systems with micrometer spatial resolution (via momentum microscopy) has demonstrated the capability of measuring electron and exciton dynamics in exfoliated samples and moiré heterostructures (Madéo *et al.*, 2020; Dong *et al.*, 2021; Karni *et al.*, 2022; Schmitt *et al.*, 2022). However, thus far momentum microscopes

cannot easily achieve sub-20-meV energy resolutions and are not well suited for measuring irregular or nonideal cleaved surfaces. For this reason, we envision the development of TR-ARPES systems with micrometer UV or XUV spot sizes, coupled to hemispherical or time-of-flight detectors operating at high repetition rates to mitigate space-charge effects (Dufresne *et al.*, 2023). These efforts should enable the investigation of ultrafast electron dynamics in twisted moiré structures (Topp *et al.*, 2019, 2021; Andrei *et al.*, 2021; Kennes *et al.*, 2021; Rodriguez-Vega, Vogl, and Fiete, 2021), and in general micrometer-sized samples, with high enough energy resolution to resolve light-induced changes of the low-energy electronic structure.

TR-ARPES at free-electron laser facilities and with a tunable $\Delta E \Delta \tau$ product. Free-electron lasers (FELs) are rapidly upgrading their operation to the kilohertz-to-mega-hertz range, thus enabling TR-ARPES studies that otherwise would have required unreasonably long acquisition times at sub-1-kHz repetition rates (Oloff *et al.*, 2016; Rossbach, Schneider, and Wurth, 2019; Kutnyakhov *et al.*, 2020). FEL facilities promise access to fully tunable probe pulses in the XUV-to-soft-x-ray photon-energy range, which would allow core-level photoemission studies to be performed (Pietzsch *et al.*, 2008; Hellmann *et al.*, 2010, 2012b; Dendzik *et al.*, 2020; Curcio *et al.*, 2021), as well as tracking light-induced changes in electronic structure throughout the entire 3D Brillouin zone (for example, by probing different k_z via a photon-energy-dependent scan), hence differentiating surface contributions to the photoemission intensity from bulk ones. When considering probe tunability, we expect FEL facilities and new in-house TR-ARPES systems to also enable control of the $\Delta E \Delta \tau$ product. Indeed, this review covered several experimental studies that employed diametrically opposed working parameters, such as tracking the super-conducting gap of cuprates (Parham *et al.*, 2017; Boschini *et al.*, 2018) thanks to high energy resolution, or tracking the out-of-equilibrium electron dynamics on sub-30-fs timescales (Rohde *et al.*, 2018; Tengdin *et al.*, 2018). The TR-ARPES community wants to continuously tune $\Delta E \Delta \tau$ (for instance, by adjusting the probe-pulse bandwidth and its compression) in an effort to reliably correlate ultrafast changes in the electronic distribution and photoemission intensity to changes in the underlying spectral function and orbital characters for all quantum materials. Alternative experimental strategies to overcome the Fourier uncertainty to achieve high-energy and temporal resolutions simultaneously could rely on the use of pairs of entangled photons (Gu *et al.*, 2023) or double-probe interferometric schemes (Randi, Fausti, and Eckstein, 2017).

TR-ARPES with full polarization control to explore orbital and spin textures. While tunable polarization of low-energy pump pulses is already widely available, full control of the probe-pulse polarization (linear and circular), especially in the XUV range, presents greater challenges. Advances in this area will likely enable studies on the symmetry of the orbital and spin degrees of freedom of transient states in magnetic and spin-orbit coupled systems (Beaulieu *et al.*, 2020; Schüler and Beaulieu, 2022), as well as full disentanglement of matrix element effects from the transient photoemission intensity (Boschini *et al.*, 2020a). XUV light sources that can access the entire 3D Brillouin zone with full polarization control are

already under construction (Comby *et al.*, 2022), and we expect this new experimental capability to not only facilitate and expand the current understanding of what we precisely measure in a TR-ARPES experiment but also allow the detection of transient states that have eluded us thus far.

Observation of dynamic electron correlations with momentum resolution. TR-ARPES, like ARPES, probes the one-electron-removal spectral function and infers underlying many-body correlations via analysis of the line shape and dispersion of spectral features. However, it would be desirable to directly access the dispersion relation and correlation strength of two or more entangled particles (for instance, a Cooper pair) with momentum resolution. To this end, extensions of the ARPES technique such as two-electron ARPES (2e-ARPES) (Berakdar, 1998; Mahmood *et al.*, 2022) or noise-correlation ARPES (Stahl and Eckstein, 2019) have been proposed. We anticipate that 2e-ARPES and noise-correlation ARPES (and other possible approaches that might go beyond the single-particle picture) will naturally be extended into the time domain, thus providing a comprehensive view of how light excitation may disrupt, enhance, or lock charge correlations among specific electronic states. Moreover, we foresee increasing interest in combining TR-ARPES with other complementary time-resolved techniques, such as ultrafast electron and x-ray diffraction (Elsaesser and Woerner, 2014; Gerber *et al.*, 2017; Filippetto *et al.*, 2022), time-resolved energy-integrated and inelastic x-ray scattering (Mitrano and Wang, 2020; Wandel *et al.*, 2022), and time-resolved electron energy-loss spectroscopy to link light-induced changes of the correlation strength between specific electronic states to those of the dynamic charge density response function.

In conclusion, as a final forward-looking consideration, while the work reviewed here has already established TR-ARPES as a mature technique and demonstrated its impact on various branches of physics and chemistry, further experimental and theoretical developments, augmented by a portfolio of complementary time-resolved techniques, strongly suggest that even more interesting times lie ahead.

REFERENCES

Aeschlimann, S., *et al.*, 2020, Sci. Adv. **6**, eaay0761.

Aeschlimann, S., *et al.*, 2021, Nano Lett. **21**, 5028.

Alencar, T. V., M. G. Silva, L. M. Malard, and A. M. de Paula, 2014, Nano Lett. **14**, 5621.

Allen, P. B., 1987, Phys. Rev. Lett. **59**, 1460.

Andreatta, F., *et al.*, 2019, Phys. Rev. B **99**, 165421.

Andrei, E. Y., D. K. Efetov, P. Jarillo-Herrero, A. H. MacDonald, K. F. Mak, T. Senthil, E. Tutuc, A. Yazdani, and A. F. Young, 2021, Nat. Rev. Mater. **6**, 201.

Anisimov, S., B. Kapeliovich, and T. Perel'Man, 1974, Zh. Eksp. Teor. Fiz. **66**, 776, http://jetp.ras.ru/cgi-bin/e/index/e/39/2/p375?a=list.

Armitage, N. P., *et al.*, 2001, Phys. Rev. Lett. **87**, 147003.

Ashcroft, N. W., and N. D. Mermin, 1976, *Solid State Physics* (Holt, Rinehart and Winston, New York).

Azoury, D., *et al.*, 2023, Proc. Natl. Acad. Sci. U.S.A. **120**, e2308588120.

Baldini, E., *et al.*, 2020, Proc. Natl. Acad. Sci. U.S.A. **117**, 6409.

Baldini, E., *et al.*, 2023, Proc. Natl. Acad. Sci. U.S.A. 120, e2221688120.

Bandrauk, A. D., and M. L. Sink, 1981, J. Chem. Phys. **74**, 1110.

Bao, C., H. Zhong, F. Wang, T. Lin, H. Zhang, Z. Sun, W. Duan, and S. Zhou, 2023, Phys. Rev. B **107**, L121103.

Bao, C., H. Zhong, S. Zhou, R. Feng, Y. Wang, and S. Zhou, 2022, Rev. Sci. Instrum. **93**, 013902.

Bao, C., *et al.*, 2022, Nano Lett. **22**, 1138.

Bartoli, A., G. Ferrini, L. Fini, G. Gabetta, F. Parmigiani, and F. Arecchi, 1997, Phys. Rev. B **56**, 1107.

Basov, D., R. Averitt, and D. Hsieh, 2017, Nat. Mater. **16**, 1077.

Battiato, M., K. Carva, and P. M. Oppeneer, 2010, Phys. Rev. Lett. **105**, 027203.

Battiato, M., J. Minár, W. Wang, W. Ndiaye, M. Richter, O. Heckmann, J.-M. Mariot, F. Parmigiani, K. Hricovíni, and C. Cacho, 2018, Phys. Rev. Lett. **121**, 077205.

Beaulieu, S., *et al.*, 2020, Phys. Rev. Lett. **125**, 216404.

Beaulieu, S., *et al.*, 2021, Sci. Adv. **7**, eabd9275.

Beaurepaire, E., J.-C. Merle, A. Daunois, and J.-Y. Bigot, 1996, Phys. Rev. Lett. **76**, 4250.

Berakdar, J., 1998, Phys. Rev. B **58**, 9808.

Bertoni, R., *et al.*, 2016, Phys. Rev. Lett. **117**, 277201.

Beyazit, Y., J. Beckord, P. Zhou, J. Meyburg, F. Kühne, D. Diesing, M. Ligges, and U. Bovensiepen, 2020, Phys. Rev. Lett. **125**, 076803.

Beyazit, Y., F. Kühne, D. Diesing, P. Zhou, J. Jayabalan, B. Sothmann, and U. Bovensiepen, 2023, Phys. Rev. B **107**, 085412.

Beyer, H., *et al.*, 2019, Phys. Rev. Lett. **123**, 236802.

Biswas, D., *et al.*, 2021, Nano Lett. **21**, 1968.

Bonaccorso, F., Z. Sun, T. Hasan, and A. Ferrari, 2010, Nat. Photonics **4**, 611.

Borisenko, S., *et al.*, 2022, Nat. Commun. **13**, 4132.

Boschini, F., H. Hedayat, C. Dallera, P. Farinello, C. Manzoni, A. Magrez, H. Berger, G. Cerullo, and E. Carpene, 2014, Rev. Sci. Instrum. **85**, 123903.

Boschini, F., *et al.*, 2018, Nat. Mater. **17**, 416.

Boschini, F., *et al.*, 2020a, New J. Phys. **22**, 023031.

Boschini, F., *et al.*, 2020b, npj Quantum Mater. **5**, 6.

Bostwick, A., T. Ohta, T. Seyller, K. Horn, and E. Rotenberg, 2007, Nat. Phys. **3**, 36.

Bovensiepen, U., 2007, J. Phys. Condens. Matter **19**, 083201.

Braun, J., R. Rausch, M. Potthoff, J. Minár, and H. Ebert, 2015, Phys. Rev. B **91**, 035119.

Brorson, S., J. Fujimoto, and E. Ippen, 1987, Phys. Rev. Lett. **59**, 1962.

Brorson, S., A. Kazeroonian, J. Moodera, D. Face, T. Cheng, E. Ippen, M. Dresselhaus, and G. Dresselhaus, 1990, Phys. Rev. Lett. **64**, 2172.

Bugini, D., F. Boschini, H. Hedayat, H. Yi, C. Chen, X. Zhou, C. Manzoni, C. Dallera, G. Cerullo, and E. Carpene, 2017, J. Phys. Condens. Matter **29**, 30LT01.

Buss, J. H., *et al.*, 2019, Rev. Sci. Instrum. **90**, 023105.

Cacho, C., *et al.*, 2015, Phys. Rev. Lett. **114**, 097401.

Cao, T., *et al.*, 2012, Nat. Commun. **3**, 887.

Cao, Y., V. Fatemi, S. Fang, K. Watanabe, T. Taniguchi, E. Kaxiras, and P. Jarillo-Herrero, 2018, Nature (London) **556**, 43.

Cao, Y., *et al.*, 2013, Nat. Phys. **9**, 499.

Cao, Y., *et al.*, 2018, Nature (London) **556**, 80.

Caputo, M., L. Khalil, E. Papalazarou, N. Nilforoushan, L. Perfetti, A. Taleb-Ibrahimi, Q. Gibson, R. J. Cava, and M. Marsi, 2018, Phys. Rev. B **97**, 115115.

Carley, R., K. Döbrich, B. Frietsch, C. Gahl, M. Teichmann, O. Schwarzkopf, P. Wernet, and M. Weinelt, 2012, Phys. Rev. Lett. **109**, 057401.

Carpene, E., 2006, Phys. Rev. B **74**, 024301.

Carpene, E., E. Mancini, C. Dallera, M. Brenna, E. Puppin, and S. De Silvestri, 2008, Phys. Rev. B **78**, 174422.

Carpene, E., E. Mancini, C. Dallera, G. Ghiringhelli, C. Manzoni, G. Cerullo, and S. De Silvestri, 2009, Rev. Sci. Instrum. **80**, 055101.

Cavalleri, A., 2018, Contemp. Phys. **59**, 31.

Caviglia, A., S. Gariglio, N. Reyren, D. Jaccard, T. Schneider, M. Gabay, S. Thiel, G. Hammerl, J. Mannhart, and J.-M. Triscone, 2008, Nature (London) **456**, 624.

Chávez-Cervantes, M., R. Krause, S. Aeschlimann, and I. Gierz, 2018, Phys. Rev. B **97**, 201401.

Chávez-Cervantes, M., G. Topp, S. Aeschlimann, R. Krause, S. Sato, M. Sentef, and I. Gierz, 2019, Phys. Rev. Lett. **123**, 036405.

Chen, Z., J. Sjakste, J. Dong, A. Taleb-Ibrahimi, J.-P. Rueff, A. Shukla, J. Peretti, E. Papalazarou, M. Marsi, and L. Perfetti, 2020, Proc. Natl. Acad. Sci. U.S.A. **117**, 21962.

Chen, Z., *et al.*, 2018, Phys. Rev. B **97**, 241201.

Chiang, C.-T., A. Blättermann, M. Huth, J. Kirschner, and W. Widdra, 2012, Appl. Phys. Lett. **101**, 071116.

Christiansen, D., M. Selig, E. Malic, R. Ernstorfer, and A. Knorr, 2019, Phys. Rev. B **100**, 205401.

Cilento, F., A. Crepaldi, G. Manzoni, A. Sterzi, M. Zacchigna, P. Bugnon, H. Berger, and F. Parmigiani, 2016, J. Electron Spectrosc. Relat. Phenom. **207**, 7.

Cilento, F., *et al.*, 2018, Sci. Adv. **4**, eaar1998.

Cinchetti, M., M. S. Albaneda, D. Hoffmann, T. Roth, J.-P. Wüstenberg, M. Krauß, O. Andreyev, H. Schneider, M. Bauer, and M. Aeschlimann, 2006, Phys. Rev. Lett. **97**, 177201.

Ciocys, S., T. Morimoto, J. Moore, and A. Lanzara, 2019, J. Stat. Mech. 104008.

Ciocys, S., T. Morimoto, R. Mori, K. Gotlieb, Z. Hussain, J. G. Analytis, J. E. Moore, and A. Lanzara, 2020, npj Quantum Mater. **5**, 16.

Ciocys, S. T., and A. Lanzara, 2023, Commun. Mater. **4**, 48.

Ciocys, S. T., N. Maksimovic, J. G. Analytis, and A. Lanzara, 2022, npj Quantum Mater. **7**, 79.

Comby, A., D. Rajak, D. Descamps, S. Petit, V. Blanchet, Y. Mairesse, J. Gaudin, and S. Beaulieu, 2022, J. Opt. **24**, 084003.

Comin, R., and A. Damascelli, 2016, Annu. Rev. Condens. Matter Phys. **7**, 369.

Corder, C., P. Zhao, J. Bakalis, X. Li, M. D. Kershis, A. R. Muraca, M. G. White, and T. K. Allison, 2018, Struct. Dyn. **5**, 054301.

Cortés, R., L. Rettig, Y. Yoshida, H. Eisaki, M. Wolf, and U. Bovensiepen, 2011, Phys. Rev. Lett. **107**, 097002.

Crepaldi, A., M. Puppin, D. Gosálbez-Martínez, L. Moreschini, F. Cilento, H. Berger, O. Yazyev, M. Chergui, and M. Grioni, 2022, JPhys Mater. **5**, 044006.

Crepaldi, A., B. Ressel, F. Cilento, M. Zacchigna, C. Grazioli, H. Berger, P. Bugnon, K. Kern, M. Grioni, and F. Parmigiani, 2012, Phys. Rev. B **86**, 205133.

Crepaldi, A., *et al.*, 2013, Phys. Rev. B **88**, 121404.

Crepaldi, A., *et al.*, 2017, Phys. Rev. B **96**, 241408.

Cui, X., C. Wang, A. Argondizzo, S. Garrett-Roe, B. Gumhalter, and H. Petek, 2014, Nat. Phys. **10**, 505.

Curcio, D., *et al.*, 2021, Phys. Rev. B **104**, L161104.

Dakovski, G., Y. Li, T. Durakiewicz, and G. Rodriguez, 2010, Rev. Sci. Instrum. **81**, 073108.

Dakovski, G. L., T. Durakiewicz, J.-X. Zhu, P. S. Riseborough, G. Gu, S. M. Gilbertson, A. Taylor, and G. Rodriguez, 2015, Struct. Dyn. **2**, 054501.

Damascelli, A., 2004, Phys. Scr. **T109**, 61.

Damascelli, A., G. Gabetta, A. Lumachi, L. Fini, and F. Parmigiani, 1996, Phys. Rev. B **54**, 6031.

Damascelli, A., Z. Hussain, and Z.-X. Shen, 2003, Rev. Mod. Phys. **75**, 473.

Day, R. P., B. Zwartsenberg, I. S. Elfimov, and A. Damascelli, 2019, npj Quantum Mater. **4**, 54.

De Giovannini, U., H. Hübener, S. A. Sato, and A. Rubio, 2020, Phys. Rev. Lett. **125**, 136401.

De Giovannini, U., S. A. Sato, H. Hübener, and A. Rubio, 2022, J. Electron Spectrosc. Relat. Phenom. **254**, 147152.

Deinert, J.-C., D. Wegkamp, M. Meyer, C. Richter, M. Wolf, and J. Stähler, 2014, Phys. Rev. Lett. **113**, 057602.

de la Torre, A., D. M. Kennes, M. Claassen, S. Gerber, J. W. McIver, and M. A. Sentef, 2021, Rev. Mod. Phys. **93**, 041002.

Del Fatti, N., C. Voisin, M. Achermann, S. Tzortzakis, D. Christofilos, and F. Vallée, 2000, Phys. Rev. B **61**, 16956.

Dendzik, M., *et al.*, 2020, Phys. Rev. Lett. **125**, 096401.

Deng, Y., Y. Yu, M. Z. Shi, Z. Guo, Z. Xu, J. Wang, X. H. Chen, and Y. Zhang, 2020, Science **367**, 895.

Dhar, L., J. A. Rogers, and K. A. Nelson, 1994, Chem. Rev. **94**, 157.

Disa, A. S., T. F. Nova, and A. Cavalleri, 2021, Nat. Phys. **17**, 1087.

Dong, J., et al., 2023a, 2D Mater. **10**, 045001.

Dong, J., et al., 2023b, Phys. Rev. B **108**, 155145.

Dong, S., et al., 2021, Nat. Sci. **1**, e10010.

Dong, S., et al., 2023, Nat. Commun. **14**, 5057.

Duan, S., W. Xia, C. Huang, S. Wang, L. Gu, H. Liu, D. Xiang, D. Qian, Y. Guo, and W. Zhang, 2023, Phys. Rev. Lett. **130**, 226501.

Duan, S., et al., 2021, Nature (London) **595**, 239.

Dufresne, S. K. Y., et al., 2023, arXiv:2309.04524.

Duvel, M., et al., 2022, Nano Lett. **22**, 4897.

Eckstein, M., 2021, J. Electron Spectrosc. Relat. Phenom. **253**, 147108.

Eich, S., et al., 2014, J. Electron Spectrosc. Relat. Phenom. **195**, 231.

Eich, S., et al., 2017, Sci. Adv. **3**, e1602094.

Elsaesser, T., and M. Woerner, 2014, J. Chem. Phys. **140**, 020901.

Emery, V., and S. Kivelson, 1995, Nature (London) **374**, 434.

Faisal, F., and J. Kamiński, 1997, Phys. Rev. A **56**, 748.

Fanciulli, M., et al., 2020, Phys. Rev. Res. **2**, 013261.

Fanfarillo, L., et al., 2021, J. Electron Spectrosc. Relat. Phenom. **250**, 147090.

Faure, J., J. Mauchain, E. Papalazarou, W. Yan, J. Pinon, M. Marsi, and L. Perfetti, 2012, Rev. Sci. Instrum. **83**, 043109.

Fausti, D., R. Tobey, N. Dean, S. Kaiser, A. Dienst, M. C. Hoffmann, S. Pyon, T. Takayama, H. Takagi, and A. Cavalleri, 2011, Science **331**, 189.

Fero, A., C. Smallwood, G. Affeldt, and A. Lanzara, 2014, J. Electron Spectrosc. Relat. Phenom. **195**, 237.

Ferrini, G., A. Viggiani, D. Sertore, P. Michelato, and F. Parmigiani, 1999, Phys. Rev. B **60**, 8383.

Filippetto, D., P. Musumeci, R. Li, B. J. Siwick, M. Otto, M. Centurion, and J. Nunes, 2022, Rev. Mod. Phys. **94**, 045004.

Fognini, A., et al., 2014, Appl. Phys. Lett. **104**, 032402.

Först, M., C. Manzoni, S. Kaiser, Y. Tomioka, Y. Tokura, R. Merlin, and A. Cavalleri, 2011, Nat. Phys. **7**, 854.

Freericks, J., and A. F. Kemper, 2021, J. Electron Spectrosc. Relat. Phenom. **251**, 147104.

Freericks, J., H. Krishnamurthy, Y. Ge, A. Liu, and T. Pruschke, 2009, Phys. Status Solidi (b) **246**, 948.

Freericks, J., H. Krishnamurthy, and T. Pruschke, 2009, Phys. Rev. Lett. **102**, 136401.

Freericks, J. K., and H. Krishnamurthy, 2016, in Photonics, Vol. 3 (Multidisciplinary Digital Publishing Institute, Basel), p. 58.

Freutel, S., et al., 2019, Phys. Rev. B **99**, 081116.

Freyse, F., M. Battiato, L. Yashina, and J. Sánchez-Barriga, 2018, Phys. Rev. B **98**, 115132.

Frietsch, B., R. Carley, K. Döbrich, C. Gahl, M. Teichmann, O. Schwarzkopf, P. Wernet, and M. Weinelt, 2013, Rev. Sci. Instrum. **84**, 075106.

Frietsch, B., et al., 2020, Sci. Adv. **6**, eabb1601.

Frigge, T., et al., 2017, Nature (London) **544**, 207.

Fu, L., C. L. Kane, and E. J. Mele, 2007, Phys. Rev. Lett. **98**, 106803.

Fukushima, Y., et al., 2023, arXiv:2303.17816.

Garrett, G. A., T. Albrecht, J. Whitaker, and R. Merlin, 1996, Phys. Rev. Lett. **77**, 3661.

Gatti, G., et al., 2020, Phys. Rev. Lett. **125**, 076401.

Gauthier, A., J. A. Sobota, N. Gauthier, K.-J. Xu, H. Pfau, C. R. Rotundu, Z.-X. Shen, and P. S. Kirchmann, 2020, J. Appl. Phys. **128**, 093101.

Gauthier, N., J. A. Sobota, H. Pfau, A. Gauthier, H. Soifer, M. D. Bachmann, I. R. Fisher, Z.-X. Shen, and P. S. Kirchmann, 2021, Rev. Sci. Instrum. **92**, 123907.

Gedik, N., M. Langner, J. Orenstein, S. Ono, Y. Abe, and Y. Ando, 2005, Phys. Rev. Lett. **95**, 117005.

Gedik, N., and I. Vishik, 2017, Nat. Phys. **13**, 1029.

Gerber, S., et al., 2017, Science **357**, 71.

Giannetti, C., M. Capone, D. Fausti, M. Fabrizio, F. Parmigiani, and D. Mihailovic, 2016, Adv. Phys. **65**, 58.

Gierster, L., S. Vempati, and J. Stähler, 2021, Nat. Commun. **12**, 978.

Gierz, I., 2017, J. Electron Spectrosc. Relat. Phenom. **219**, 53.

Gierz, I., J. Henk, H. Höchst, C. R. Ast, and K. Kern, 2011, Phys. Rev. B **83**, 121408.

Gierz, I., M. Mitrano, J. C. Petersen, C. Cacho, I. E. Turcu, E. Springate, A. Stöhr, A. Köhler, U. Starke, and A. Cavalleri, 2015, J. Phys. Condens. Matter **27**, 164204.

Gierz, I., J. C. Petersen, M. Mitrano, C. Cacho, I. E. Turcu, E. Springate, A. Stöhr, A. Köhler, U. Starke, and A. Cavalleri, 2013, Nat. Mater. **12**, 1119.

Gierz, I., et al., 2015a, Phys. Rev. Lett. **115**, 086803.

Gierz, I., et al., 2015b, Phys. Rev. Lett. **114**, 125503.

Giustino, F., 2017, Rev. Mod. Phys. **89**, 015003.

Golež, D., et al., 2022, Phys. Rev. B **106**, L121106.

Golias, E., and J. Sánchez-Barriga, 2016, Phys. Rev. B **94**, 161113.

Gort, R., et al., 2018, Phys. Rev. Lett. **121**, 087206.

Gotlieb, K., Z. Hussain, A. Bostwick, A. Lanzara, and C. Jozwiak, 2013, Rev. Sci. Instrum. **84**, 093904.

Gotlieb, K., C.-Y. Lin, M. Serbyn, W. Zhang, C. L. Smallwood, C. Jozwiak, H. Eisaki, Z. Hussain, A. Vishwanath, and A. Lanzara, 2018, Science **362**, 1271.

Graf, J., C. Jozwiak, C. L. Smallwood, H. Eisaki, R. A. Kaindl, D.-H. Lee, and A. Lanzara, 2011, Nat. Phys. **7**, 805.

Grimwall, G., 1980, The Electron-Phonon Interaction in Metals (North-Holland, Amsterdam).

Grubišić Čabo, A., et al., 2015, Nano Lett. **15**, 5883.

Gu, B., S. Sun, F. Chen, and S. Mukamel, 2023, Proc. Natl. Acad. Sci. U.S.A. **120**, e2300541120.

Guo, Q., et al., 2022, Struct. Dyn. **9**, 024304.

Haight, R., and D. Peale, 1994, Rev. Sci. Instrum. **65**, 1853.

Hajlaoui, M., et al., 2012, Nano Lett. **12**, 3532.

Hajlaoui, M., et al., 2014, Nat. Commun. **5**, 3003.

Hao, Z., J. Dadap, K. Knox, M. Yilmaz, N. Zaki, P. Johnson, and R. Osgood, 2010, Phys. Rev. Lett. **105**, 017602.

Hasan, M. Z., and C. L. Kane, 2010, Rev. Mod. Phys. **82**, 3045.

Hatch, R. C., M. Bianchi, D. Guan, S. Bao, J. Mi, B. B. Iversen, L. Nilsson, L. Hornekær, and P. Hofmann, 2011, Phys. Rev. B **83**, 241303.

Heber, M., N. Wind, D. Kutnyakhov, F. Pressacco, and K. Rossnagel, 2022, Rev. Sci. Instrum. **93**, 083905.

Hedayat, H., D. Bugini, H. Yi, C. Chen, X. Zhou, G. Cerullo, C. Dallera, and E. Carpene, 2018, Appl. Sci. **8**, 694.

Hedayat, H., D. Bugini, H. Yi, C. Chen, X. Zhou, G. Cerullo, C. Dallera, and E. Carpene, 2021, Sci. Rep. **11**, 4924.

Hedayat, H., A. Ceraso, G. Soavi, S. Akhavan, A. Cadore, C. Dallera, G. Cerullo, A. C. Ferrari, and E. Carpene, 2021, 2D Mater. **8**, 025020.

Hedayat, H., et al., 2019, Phys. Rev. Res. **1**, 023029.

Hein, P., S. Jauernik, H. Erk, L. Yang, Y. Qi, Y. Sun, C. Felser, and M. Bauer, 2020, Nat. Commun. **11**, 2613.

Hein, P., A. Stange, K. Hanff, L. Yang, G. Rohde, K. Rossnagel, and M. Bauer, 2016, Phys. Rev. B **94**, 205406.

Hellmann, S., K. Rossnagel, M. Marczynski-Bühlow, and L. Kipp, 2009, Phys. Rev. B **79**, 035402.

Hellmann, S., et al., 2010, Phys. Rev. Lett. **105**, 187401.

Hellmann, S., et al., 2012a, Nat. Commun. **3**, 1069.

Hellmann, S., *et al.*, 2012b, New J. Phys. **14**, 013062.

Heyl, C., J. Güdde, A. L'Huillier, and U. Höfer, 2012, J. Phys. B **45**, 074020.

Hofer, U., I. Shumay, C. Reuß, U. Thomann, W. Wallauer, and T. Fauster, 1997, Science **277**, 1480.

Hsieh, D., F. Mahmood, J. McIver, D. Gardner, Y. Lee, and N. Gedik, 2011, Phys. Rev. Lett. **107**, 077401.

Hu, W., S. Kaiser, D. Nicoletti, C. R. Hunt, I. Gierz, M. C. Hoffmann, M. Le Tacon, T. Loew, B. Keimer, and A. Cavalleri, 2014, Nat. Mater. **13**, 705.

Huang, C., S. Duan, and W. Zhang, 2022, Quantum Front. **1**, 15.

Huang, Y., *et al.*, 2023, Phys. Rev. X **13**, 041050.

Huber, M., Y. Lin, N. Dale, R. Sailus, S. Tongay, R. A. Kaindl, and A. Lanzara, 2022, J. Phys. Chem. Solids **168**, 110740.

Hwang, C., W. Zhang, K. Kurashima, R. Kaindl, T. Adachi, Y. Koike, and A. Lanzara, 2019, Europhys. Lett. **126**, 57001.

Ishida, Y., T. Otsu, T. Shimada, M. Okawa, Y. Kobayashi, F. Iga, T. Takabatake, and S. Shin, 2015, Sci. Rep. **5**, 8160.

Ishida, Y., T. Saitoh, T. Mochiku, T. Nakane, K. Hirata, and S. Shin, 2016, Sci. Rep. **6**, 18747.

Ishida, Y., T. Togashi, K. Yamamoto, M. Tanaka, T. Taniuchi, T. Kiss, M. Nakajima, T. Suemoto, and S. Shin, 2011, Sci. Rep. **1**, 64.

Ishizaka, K., *et al.*, 2011, Phys. Rev. B **83**, 081104.

Ito, S., *et al.*, 2023, Nature (London) **616**, 696.

Jansen, G., *et al.*, 2020, New J. Phys. **22**, 063012.

Jérome, D., T. Rice, and W. Kohn, 1967, Phys. Rev. **158**, 462.

Johannsen, J. C., *et al.*, 2013, Phys. Rev. Lett. **111**, 027403.

Johannsen, J. C., *et al.*, 2015, Nano Lett. **15**, 326.

Johnson, P., *et al.*, 2001, Phys. Rev. Lett. **87**, 177007.

Jozwiak, C., J. A. Sobota, K. Gotlieb, A. F. Kemper, C. R. Rotundu, R. J. Birgeneau, Z. Hussain, D.-H. Lee, Z.-X. Shen, and A. Lanzara, 2016, Nat. Commun. **7**, 13143.

Kabanov, V., J. Demsar, B. Podobnik, and D. Mihailovic, 1999, Phys. Rev. B **59**, 1497.

Kaganov, M., E. Lifshitz, and L. Tanatarov, 1957, Sov. Phys. JETP **4**, 173, http://www.jetp.ras.ru/cgi-bin/e/index/e/4/2/p173?a=list.

Kanasaki, J., H. Tanimura, and K. Tanimura, 2014, Phys. Rev. Lett. **113**, 237401.

Karni, O., *et al.*, 2022, Nature (London) **603**, 247.

Keimer, B., and J. Moore, 2017, Nat. Phys. **13**, 1045.

Kemper, A., O. Abdurazakov, and J. Freericks, 2018, Phys. Rev. X **8**, 041009.

Kemper, A., M. Sentef, B. Moritz, J. Freericks, and T. Devereaux, 2014, Phys. Rev. B **90**, 075126.

Kemper, A., M. Sentef, B. Moritz, C. Kao, Z. Shen, J. Freericks, and T. Devereaux, 2013, Phys. Rev. B **87**, 235139.

Kemper, A., M. A. Sentef, B. Moritz, T. Devereaux, and J. Freericks, 2017, Ann. Phys. (Berlin) **529**, 1600235.

Kennes, D. M., M. Claassen, L. Xian, A. Georges, A. J. Millis, J. Hone, C. R. Dean, D. Basov, A. N. Pasupathy, and A. Rubio, 2021, Nat. Phys. **17**, 155.

Keunecke, M., *et al.*, 2020, Rev. Sci. Instrum. **91**, 063905.

Khalil, L., *et al.*, 2019, J. Appl. Phys. **125**, 025103.

Kirilyuk, A., A. V. Kimel, and T. Rasing, 2010, Rev. Mod. Phys. **82**, 2731.

Kogar, A., *et al.*, 2017, Science **358**, 1314.

Konstantinova, T., *et al.*, 2018, Sci. Adv. **4**, eaap7427.

Koopmans, B., G. Malinowski, F. Dalla Longa, D. Steiauf, M. Fähnle, T. Roth, M. Cinchetti, and M. Aeschlimann, 2010, Nat. Mater. **9**, 259.

Kratzer, P., L. Rettig, I. Y. Sklyadneva, E. V. Chulkov, and U. Bovensiepen, 2022, Phys. Rev. Res. **4**, 033218.

Kremer, G., M. Rumo, C. Yue, A. Pulkkinen, C. Nicholson, T. Jaouen, F. von Rohr, P. Werner, and C. Monney, 2021, Phys. Rev. B **104**, 035125.

Kremer, G., *et al.*, 2022, Nat. Commun. **13**, 6396.

Krömker, B., M. Escher, D. Funnemann, D. Hartung, H. Engelhard, and J. Kirschner, 2008, Rev. Sci. Instrum. **79**, 053702.

Kronik, L., and Y. Shapira, 1999, Surf. Sci. Rep. **37**, 1.

Kühne, F., Y. Beyazit, B. Sothmann, J. Jayabalan, D. Diesing, P. Zhou, and U. Bovensiepen, 2022, Phys. Rev. Res. **4**, 033239.

Kunin, A., *et al.*, 2023, Phys. Rev. Lett. **130**, 046202.

Kurleto, R., and J. Fink, 2021, J. Electron Spectrosc. Relat. Phenom. **253**, 147127.

Kuroda, K., J. Reimann, J. Güdde, and U. Höfer, 2016, Phys. Rev. Lett. **116**, 076801.

Kuroda, K., J. Reimann, K. Kokh, O. Tereshchenko, A. Kimura, J. Güdde, and U. Höfer, 2017, Phys. Rev. B **95**, 081103.

Kutnyakhov, D., *et al.*, 2016, Sci. Rep. **6**, 29394.

Kutnyakhov, D., *et al.*, 2020, Rev. Sci. Instrum. **91**, 013109.

Lantz, G., *et al.*, 2017, Nat. Commun. **8**, 13917.

Lanzara, A., *et al.*, 2001, Nature (London) **412**, 510.

Lee, C., *et al.*, 2020, Rev. Sci. Instrum. **91**, 043102.

Lee, W., Y. Lin, L.-S. Lu, W.-C. Chueh, M. Liu, X. Li, W.-H. Chang, R. A. Kaindl, and C.-K. Shih, 2021, Nano Lett. **21**, 7363.

Lee, W., *et al.*, 2023, Nat. Phys. **19**, 950.

Li, F., and G. A. Sawatzky, 2018, Phys. Rev. Lett. **120**, 237001.

Li, H., X. Zhou, S. Parham, T. J. Reber, H. Berger, G. B. Arnold, and D. S. Dessau, 2018, Nat. Commun. **9**, 26.

Li, H., *et al.*, 2019, Phys. Rev. X **9**, 041039.

Li, J., Y. Li, S. Du, Z. Wang, B.-L. Gu, S.-C. Zhang, K. He, W. Duan, and Y. Xu, 2019, Sci. Adv. **5**, eaaw5685.

Li, X., T. Qiu, J. Zhang, E. Baldini, J. Lu, A. M. Rappe, and K. A. Nelson, 2019, Science **364**, 1079.

Ligges, M., *et al.*, 2018, Phys. Rev. Lett. **120**, 166401.

Lin, Y., Y.-h. Chan, W. Lee, L.-S. Lu, Z. Li, W.-H. Chang, C.-K. Shih, R. A. Kaindl, S. G. Louie, and A. Lanzara, 2022, Phys. Rev. B **106**, L081117.

Lisowski, M., P. Loukakos, A. Melnikov, I. Radu, L. Ungureanu, M. Wolf, and U. Bovensiepen, 2005, Phys. Rev. Lett. **95**, 137402.

Liu, B., M. Först, M. Fechner, D. Nicoletti, J. Porras, T. Loew, B. Keimer, and A. Cavalleri, 2020, Phys. Rev. X **10**, 011053.

Liu, F., M. E. Ziffer, K. R. Hansen, J. Wang, and X. Zhu, 2019, Phys. Rev. Lett. **122**, 246803.

Liu, Y., L. Zhang, M. Brinkley, G. Bian, T. Miller, and T.-C. Chiang, 2010, Phys. Rev. Lett. **105**, 136804.

Lu, D., I. M. Vishik, M. Yi, Y. Chen, R. G. Moore, and Z.-X. Shen, 2012, Annu. Rev. Condens. Matter Phys. **3**, 129.

Lüth, H., 2013, *Surfaces and Interfaces of Solid Materials* (Springer Science+Business Media, New York).

Lv, B., T. Qian, and H. Ding, 2019, Nat. Rev. Phys. **1**, 609.

Madéo, J., *et al.*, 2020, Science **370**, 1199.

Mahan, G. D., 2000, *Many-Particle Physics* (Springer Science+Business Media, New York).

Mahmood, F., C.-K. Chan, Z. Alpichshev, D. Gardner, Y. Lee, P. A. Lee, and N. Gedik, 2016, Nat. Phys. **12**, 306.

Mahmood, F., T. Devereaux, P. Abbamonte, and D. K. Morr, 2022, Phys. Rev. B **105**, 064515.

Majchrzak, P., Yu. Zhang, A. Kuibarov, R. Chapman, A. Wyatt, E. Springate, S. Borisenko, B. Büchner, P. Hofmann, and C. E. Sanders, 2023, arXiv:2309.11535.

Majchrzak, P., *et al.*, 2021a, Phys. Rev. B **103**, L241108.

Majchrzak, P., *et al.*, 2021b, J. Electron Spectrosc. Relat. Phenom. **250**, 147093.

Majchrzak, P., *et al.*, 2023, Nano Lett. **23**, 414.

Mak, K. F., K. He, J. Shan, and T. F. Heinz, 2012, Nat. Nanotechnol. **7**, 494.

Maklar, J., *et al.*, 2021, Nat. Commun. **12**, 2499.

Maklar, J., *et al.*, 2022a, Phys. Rev. Lett. **128**, 026406.

Maklar, J., *et al.*, 2022b, Nano Lett. **22**, 5420.

Maklar, J., *et al.*, 2023, Sci. Adv. **9**, eadi4661.

Man, M. K., *et al.*, 2021, Sci. Adv. **7**, eabg0192.

Manzoni, G., *et al.*, 2015, Phys. Rev. Lett. **115**, 207402.

Marini, A., E. Perfetto, and G. Stefanucci, 2022, J. Electron Spectrosc. Relat. Phenom. **257**, 147189.

Marsi, M., M. Couprie, L. Nahon, D. Garzella, T. Hara, R. Bakker, M. Billardon, A. Delboulbe, G. Indlekofer, and A. Taleb-Ibrahimi, 1997, Appl. Phys. Lett. **70**, 895.

Marsi, M., *et al.*, 2000, Phys. Rev. B **61**, R5070.

Mathias, S., L. Miaja-Avila, M. Murnane, H. Kapteyn, M. Aeschlimann, and M. Bauer, 2007, Rev. Sci. Instrum. **78**, 083105.

Mathias, S., *et al.*, 2016, Nat. Commun. **7**, 12902.

Mauchain, J., *et al.*, 2013, Phys. Rev. Lett. **111**, 126603.

McIver, J. W., B. Schulte, F.-U. Stein, T. Matsuyama, G. Jotzu, G. Meier, and A. Cavalleri, 2020, Nat. Phys. **16**, 38.

Melnikov, A., H. Prima-Garcia, M. Lisowski, T. Gießel, R. Weber, R. Schmidt, C. Gahl, N. Bulgakova, U. Bovensiepen, and M. Weinelt, 2008, Phys. Rev. Lett. **100**, 107202.

Michiardi, M., *et al.*, 2022, Nat. Commun. **13**, 3096.

Miller, T. L., C. L. Smallwood, W. Zhang, H. Eisaki, J. Orenstein, and A. Lanzara, 2015, Phys. Rev. B **92**, 144506.

Miller, T. L., W. Zhang, H. Eisaki, and A. Lanzara, 2017, Phys. Rev. Lett. **118**, 097001.

Miller, T. L., W. Zhang, J. Ma, H. Eisaki, J. E. Moore, and A. Lanzara, 2018, Phys. Rev. B **97**, 134517.

Mills, A., *et al.*, 2019, Rev. Sci. Instrum. **90**, 083001.

Mitrano, M., and Y. Wang, 2020, Commun. Phys. **3**, 184.

Mitrano, M., *et al.*, 2016, Nature (London) **530**, 461.

Mönch, W., 2013, *Semiconductor Surfaces and Interfaces*, Vol. 26 (Springer Science+Business Media, New York).

Monney, C., *et al.*, 2016, Phys. Rev. B **94**, 165165.

Mor, S., M. Herzog, C. Monney, and J. Stähler, 2022, Prog. Surf. Sci. **97**, 100679.

Mor, S., *et al.*, 2017, Phys. Rev. Lett. **119**, 086401.

Mori, R., S. Ciocys, K. Takasan, P. Ai, K. Currier, T. Morimoto, J. E. Moore, and A. Lanzara, 2023, Nature (London) **614**, 249.

Morrison, V. R., R. P. Chatelain, K. L. Tiwari, A. Hendaoui, A. Bruhács, M. Chaker, and B. J. Siwick, 2014, Science **346**, 445.

Moser, S., 2017, J. Electron Spectrosc. Relat. Phenom. **214**, 29.

Moser, S., 2023, J. Electron Spectrosc. Relat. Phenom. **262**, 147278.

Mueller, B., and B. Rethfeld, 2013, Phys. Rev. B **87**, 035139.

Na, M., 2022, Ph.D. thesis (University of British Columbia).

Na, M., A. K. Mills, and D. J. Jones, 2023, Phys. Rep. **1036**, 1.

Na, M., *et al.*, 2019, Science **366**, 1231.

Na, M., *et al.*, 2020, Phys. Rev. B **102**, 184307.

Neef, A., *et al.*, 2023, Nature (London) **616**, 275.

Neufeld, O., W. Mao, H. Hübener, N. Tancogne-Dejean, S. A. Sato, U. De Giovannini, and A. Rubio, 2022, Phys. Rev. Res. **4**, 033101.

Neupane, M., *et al.*, 2015, Phys. Rev. Lett. **115**, 116801.

Nevola, D., H. X. Li, J.-Q. Yan, R. Moore, H.-N. Lee, H. Miao, and P. D. Johnson, 2020, Phys. Rev. Lett. **125**, 117205.

Nevola, D., N. Zaki, J. M. Tranquada, W.-G. Yin, G. D. Gu, Q. Li, and P. D. Johnson, 2023, Phys. Rev. X **13**, 011001.

Nicholson, C., C. Monney, R. Carley, B. Frietsch, J. Bowlan, M. Weinelt, and M. Wolf, 2016, Phys. Rev. Lett. **117**, 136801.

Nicholson, C. W., A. Lücke, W. G. Schmidt, M. Puppin, L. Rettig, R. Ernstorfer, and M. Wolf, 2018, Science **362**, 821.

Nicholson, C. W., M. Puppin, A. Lücke, U. Gerstmann, M. Krenz, W. Schmidt, L. Rettig, R. Ernstorfer, and M. Wolf, 2019, Phys. Rev. B **99**, 155107.

Nie, Z., *et al.*, 2019, Appl. Sci. **9**, 370.

Niesner, D., *et al.*, 2012, Phys. Rev. B **86**, 205403.

Nilforoushan, N., *et al.*, 2020, Phys. Rev. Res. **2**, 043397.

Oka, T., and H. Aoki, 2009, Phys. Rev. B **79**, 081406.

Oka, T., and S. Kitamura, 2019, Annu. Rev. Condens. Matter Phys. **10**, 387.

Okazaki, K., *et al.*, 2018a, Nat. Commun. **9**, 4322.

Okazaki, K., *et al.*, 2018b, Phys. Rev. B **97**, 121107.

Oloff, L.-P., *et al.*, 2016, Sci. Rep. **6**, 35087.

Otrokov, M. M., *et al.*, 2019, Nature (London) **576**, 416.

Pan, Z.-H., A. Fedorov, D. Gardner, Y. S. Lee, S. Chu, and T. Valla, 2012, Phys. Rev. Lett. **108**, 187001.

Papalazarou, E., *et al.*, 2012, Phys. Rev. Lett. **108**, 256808.

Papalazarou, E., *et al.*, 2018, Phys. Rev. Mater. **2**, 104202.

Parham, S., H. Li, T. Nummy, J. Waugh, X. Zhou, J. Griffith, J. Schneeloch, R. Zhong, G. Gu, and D. Dessau, 2017, Phys. Rev. X **7**, 041013.

Passlack, S., S. Mathias, O. Andreyev, D. Mittnacht, M. Aeschlimann, and M. Bauer, 2006, J. Appl. Phys. **100**, 024912.

Peli, S., D. Puntel, D. Kopic, B. Sockol, F. Parmigiani, and F. Cilento, 2020, J. Electron Spectrosc. Relat. Phenom. **243**, 146978.

Perfetti, L., P. Loukakos, M. Lisowski, U. Bovensiepen, H. Berger, S. Biermann, P. Cornaglia, A. Georges, and M. Wolf, 2006, Phys. Rev. Lett. **97**, 067402.

Perfetti, L., P. Loukakos, M. Lisowski, U. Bovensiepen, H. Eisaki, and M. Wolf, 2007, Phys. Rev. Lett. **99**, 197001.

Perfetti, L., P. A. Loukakos, M. Lisowski, U. Bovensiepen, M. Wolf, H. Berger, S. Biermann, and A. Georges, 2008, New J. Phys. **10**, 053019.

Perfetto, E., S. Bianchi, and G. Stefanucci, 2020, Phys. Rev. B **101**, 041201.

Perfetto, E., D. Sangalli, A. Marini, and G. Stefanucci, 2016, Phys. Rev. B **94**, 245303.

Perfetto, E., D. Sangalli, A. Marini, and G. Stefanucci, 2019, Phys. Rev. Mater. **3**, 124601.

Petek, H., and S. Ogawa, 1997, Prog. Surf. Sci. **56**, 239.

Petek, H., M. J. Weida, H. Nagano, and S. Ogawa, 2000, Science **288**, 1402.

Petersen, J. C., *et al.*, 2011, Phys. Rev. Lett. **107**, 177402.

Pietzsch, A., *et al.*, 2008, New J. Phys. **10**, 033004.

Piovera, C., Z. Zhang, M. d'Astuto, A. Taleb-Ibrahimi, E. Papalazarou, M. Marsi, Z. Li, H. Raffy, and L. Perfetti, 2015, Phys. Rev. B **91**, 224509.

Plötzing, M., R. Adam, C. Weier, L. Plucinski, S. Eich, S. Emmerich, M. Rollinger, M. Aeschlimann, S. Mathias, and C. Schneider, 2016, Rev. Sci. Instrum. **87**, 043903.

Poletto, L., and F. Frassetto, 2010, Appl. Opt. **49**, 5465.

Pomarico, E., *et al.*, 2017, Phys. Rev. B **95**, 024304.

Ponzoni, S., F. Paßlack, M. Stupar, D. M. Janas, G. Zamborlini, and M. Cinchetti, 2023, Adv. Phys. Res. **2**, 2200016.

Puppin, M., *et al.*, 2019, Rev. Sci. Instrum. **90**, 023104.

Puppin, M., *et al.*, 2022, Phys. Rev. B **105**, 075417.

Rameau, J., *et al.*, 2014, Phys. Rev. B **89**, 115115.

Rameau, J., *et al.*, 2016, Nat. Commun. **7**, 13761.

Randi, F., D. Fausti, and M. Eckstein, 2017, Phys. Rev. B **95**, 115132.

Razzoli, E., *et al.*, 2023, arXiv:2312.05378.

Rechtsman, M. C., J. M. Zeuner, Y. Plotnik, Y. Lumer, D. Podolsky, F. Dreisow, S. Nolte, M. Segev, and A. Szameit, 2013, Nature (London) **496**, 196.

Reimann, J., J. Güdde, K. Kuroda, E. V. Chulkov, and U. Höfer, 2014, Phys. Rev. B **90**, 081106.

Reimann, J., *et al.*, 2018, Nature (London) **562**, 396.

Ren, Q., T. Suzuki, T. Kanai, J. Itatani, S. Shin, and K. Okazaki, 2023, Appl. Phys. Lett. **122**, 221902.

Rettig, L., J.-H. Chu, I. Fisher, U. Bovensiepen, and M. Wolf, 2014, Faraday Discuss. **171**, 299.

Rettig, L., R. Cortés, J.-H. Chu, I. Fisher, F. Schmitt, R. Moore, Z.-X. Shen, P. Kirchmann, M. Wolf, and U. Bovensiepen, 2016, Nat. Commun. **7**, 10459.

Rettig, L., R. Cortés, S. Thirupathaiah, P. Gegenwart, H. Jeevan, M. Wolf, J. Fink, and U. Bovensiepen, 2012, Phys. Rev. Lett. **108**, 097002.

Rettig, L., P. S. Kirchmann, and U. Bovensiepen, 2012, New J. Phys. **14**, 023047.

Reutzel, M., A. Li, Z. Wang, and H. Petek, 2020, Nat. Commun. **11**, 2230.

Rhie, H.-S., H. Dürr, and W. Eberhardt, 2003, Phys. Rev. Lett. **90**, 247201.

Rini, M., R. Tobey, N. Dean, J. Itatani, Y. Tomioka, Y. Tokura, R. W. Schoenlein, and A. Cavalleri, 2007, Nature (London) **449**, 72.

Rodriguez-Vega, M., M. Vogl, and G. A. Fiete, 2021, Ann. Phys. (N.Y.) **435**, 168434.

Rohde, G., A. Hendel, A. Stange, K. Hanff, L.-P. Oloff, L. Yang, K. Rossnagel, and M. Bauer, 2016, Rev. Sci. Instrum. **87**, 103102.

Rohde, G., T. Rohwer, A. Stange, C. Sohrt, K. Hanff, L. Yang, L. Kipp, K. Rossnagel, and M. Bauer, 2014, J. Electron Spectrosc. Relat. Phenom. **195**, 244.

Rohde, G., A. Stange, A. Müller, M. Behrendt, L.-P. Oloff, K. Hanff, T. Albert, P. Hein, K. Rossnagel, and M. Bauer, 2018, Phys. Rev. Lett. **121**, 256401.

Rohwer, T., *et al.*, 2011, Nature (London) **471**, 490.

Rossbach, J., J. R. Schneider, and W. Wurth, 2019, Phys. Rep. **808**, 1.

Rudner, M. S., and N. H. Lindner, 2020, Nat. Rev. Phys. **2**, 229.

Rustagi, A., and A. F. Kemper, 2018, Phys. Rev. B **97**, 235310.

Saathoff, G., L. Miaja-Avila, M. Aeschlimann, M. Murnane, and H. Kapteyn, 2008, Phys. Rev. A **77**, 022903.

Saha, T., and D. Golež, G. De Ninno, J. Mravlje, Y. Murakami, B. Ressel, M. Stupar, and P. R. Ribič, 2021, Phys. Rev. B **103**, 144304.

Sakamoto, S., N. Gauthier, P. S. Kirchmann, J. A. Sobota, and Z.-X. Shen, 2022, Phys. Rev. B **105**, L161107.

Sánchez-Barriga, J., M. Battiato, E. Golias, A. Varykhalov, L. Yashina, O. Kornilov, and O. Rader, 2017, Appl. Phys. Lett. **110**, 141605.

Sánchez-Barriga, J., E. Golias, A. Varykhalov, J. Braun, L. Yashina, R. Schumann, J. Minár, H. Ebert, O. Kornilov, and O. Rader, 2016, Phys. Rev. B **93**, 155426.

Sánchez-Barriga, J., *et al.*, 2017, Phys. Rev. B **95**, 125405.

Sayers, C., *et al.*, 2020, Phys. Rev. B **102**, 161105.

Sayers, C., *et al.*, 2023, Phys. Rev. Lett. **130**, 156401.

Scheuch, M., T. Kampfrath, M. Wolf, K. Von Volkmann, C. Frischkorn, and L. Perfetti, 2011, Appl. Phys. Lett. **99**, 211908.

Schmidt, A., M. Pickel, M. Donath, P. Buczek, A. Ernst, V. Zhukov, P. Echenique, L. M. Sandratskii, E. Chulkov, and M. Weinelt, 2010, Phys. Rev. Lett. **105**, 197401.

Schmitt, D., *et al.*, 2022, Nature (London) **608**, 499.

Schmitt, F., P. S. Kirchmann, U. Bovensiepen, R. Moore, J. Chu, D. Lu, L. Rettig, M. Wolf, I. Fisher, and Z. Shen, 2011, New J. Phys. **13**, 063022.

Schmitt, F., *et al.*, 2008, Science **321**, 1649.

Scholl, A., L. Baumgarten, R. Jacquemin, and W. Eberhardt, 1997, Phys. Rev. Lett. **79**, 5146.

Schönhense, G., K. Medjanik, and H.-J. Elmers, 2015, J. Electron Spectrosc. Relat. Phenom. **200**, 94.

Schroder, D. K., 2001, Meas. Sci. Technol. **12**, R16.

Schüler, M., and S. Beaulieu, 2022, Commun. Phys. **5**, 164.

Schüler, M., U. De Giovannini, H. Hübener, A. Rubio, M. A. Sentef, T. P. Devereaux, and P. Werner, 2020, Phys. Rev. X **10**, 041013.

Schüler, M., T. Pincelli, S. Dong, T. P. Devereaux, M. Wolf, L. Rettig, R. Ernstorfer, and S. Beaulieu, 2022, Phys. Rev. X **12**, 011019.

Schüler, M., and M. A. Sentef, 2021, J. Electron Spectrosc. Relat. Phenom. **253**, 147121.

Schwarz, L., B. Fauseweh, and D. Manske, 2020, Phys. Rev. B **101**, 224510.

Sentef, M., A. F. Kemper, B. Moritz, J. K. Freericks, Z.-X. Shen, and T. P. Devereaux, 2013, Phys. Rev. X **3**, 041033.

Shen, Z.-X., *et al.*, 1993, Phys. Rev. Lett. **70**, 1553.

Shi, X., *et al.*, 2019, Sci. Adv. **5**, eaav4449.

Shokeen, V., *et al.*, 2023, arXiv:2306.10637.

Sie, E. J., T. Rohwer, C. Lee, and N. Gedik, 2019, Nat. Commun. **10**, 3535.

Sie, E. J., *et al.*, 2019, Nature (London) **565**, 61.

Sjakste, J., K. Tanimura, G. Barbarino, L. Perfetti, and N. Vast, 2018, J. Phys. Condens. Matter **30**, 353001.

Sjakste, J., N. Vast, G. Barbarino, M. Calandra, F. Mauri, J. Kanasaki, H. Tanimura, and K. Tanimura, 2018, Phys. Rev. B **97**, 064302.

Smallwood, C. L., J. P. Hinton, C. Jozwiak, W. Zhang, J. D. Koralek, H. Eisaki, D.-H. Lee, J. Orenstein, and A. Lanzara, 2012, Science **336**, 1137.

Smallwood, C. L., C. Jozwiak, W. Zhang, and A. Lanzara, 2012, Rev. Sci. Instrum. **83**, 123904.

Smallwood, C. L., R. A. Kaindl, and A. Lanzara, 2016, Europhys. Lett. **115**, 27001.

Smallwood, C. L., T. L. Miller, W. Zhang, R. A. Kaindl, and A. Lanzara, 2016, Phys. Rev. B **93**, 235107.

Smallwood, C. L., W. Zhang, T. L. Miller, C. Jozwiak, H. Eisaki, D.-H. Lee, and A. Lanzara, 2014, Phys. Rev. B **89**, 115126.

Smallwood, C. L., *et al.*, 2015, Phys. Rev. B **92**, 161102.

Sobota, J. A., Y. He, and Z.-X. Shen, 2021, Rev. Mod. Phys. **93**, 025006.

Sobota, J. A., S. Yang, J. G. Analytis, Y. Chen, I. R. Fisher, P. S. Kirchmann, and Z.-X. Shen, 2012, Phys. Rev. Lett. **108**, 117403.

Sobota, J. A., S.-L. Yang, D. Leuenberger, A. F. Kemper, J. G. Analytis, I. R. Fisher, P. S. Kirchmann, T. P. Devereaux, and Z.-X. Shen, 2014a, Phys. Rev. Lett. **113**, 157401.

Sobota, J. A., S.-L. Yang, D. Leuenberger, A. F. Kemper, J. G. Analytis, I. R. Fisher, P. S. Kirchmann, T. P. Devereaux, and Z.-X. Shen, 2014b, J. Electron Spectrosc. Relat. Phenom. **195**, 249.

Sobota, J. A., *et al.*, 2013, Phys. Rev. Lett. **111**, 136802.

Sobota, J. A., *et al.*, 2023, Phys. Rev. B **107**, 014305.

Sohrt, C., A. Stange, M. Bauer, and K. Rossnagel, 2014, Faraday Discuss. **171**, 243.

Soifer, H., *et al.*, 2019, Phys. Rev. Lett. **122**, 167401.

Soluyanov, A. A., D. Gresch, Z. Wang, Q. Wu, M. Troyer, X. Dai, and B. A. Bernevig, 2015, Nature (London) **527**, 495.

Someya, T., *et al.*, 2017, Phys. Rev. B **95**, 165303.

Stahl, C., and M. Eckstein, 2019, Phys. Rev. B **99**, 241111.

Stahl, Q., M. Kusch, F. Heinsch, G. Garbarino, N. Kretzschmar, K. Hanff, K. Rossnagel, J. Geck, and T. Ritschel, 2020, Nat. Commun. 11, 1247.

Stange, A., C. Sohrt, L. Yang, G. Rohde, K. Janssen, P. Hein, L.-P. Oloff, K. Hanff, K. Rossnagel, and M. Bauer, 2015, Phys. Rev. B 92, 184303.

Stern, M. J., L. P. R. de Cotret, M. R. Otto, R. P. Chatelain, J.-P. Boisvert, M. Sutton, and B. J. Siwick, 2018, Phys. Rev. B 97, 165416.

Sterzi, A., A. Crepaldi, F. Cilento, G. Manzoni, E. Frantzeskakis, M. Zacchigna, E. Van Heumen, Y. Huang, M. Golden, and F. Parmigiani, 2016, Phys. Rev. B 94, 081111.

Sterzi, A., G. Manzoni, L. Sbuelz, F. Cilento, M. Zacchigna, P. Bugnon, A. Magrez, H. Berger, A. Crepaldi, and F. Parmigiani, 2017, Phys. Rev. B 95, 115431.

Stojchevska, L., I. Vaskivskyi, T. Mertelj, P. Kusar, D. Svetin, S. Brazovskii, and D. Mihailovic, 2014, Science 344, 177.

Sumida, K., Y. Ishida, T. Yoshikawa, J. Chen, M. Nurmamat, K. Kokh, O. Tereshchenko, S. Shin, and A. Kimura, 2019, Phys. Rev. B 99, 085302.

Sumida, K., et al., 2017, Sci. Rep. 7, 14080.

Suzuki, H., et al., 2017, Phys. Rev. B 95, 165112.

Suzuki, T., S. Shin, and K. Okazaki, 2021, J. Electron Spectrosc. Relat. Phenom. 251, 147105.

Suzuki, T., et al., 2021, Phys. Rev. B 103, L121105.

Tanaka, S.-i., 2012, J. Electron Spectrosc. Relat. Phenom. 185, 152.

Tancogne-Dejean, N., M. A. Sentef, and A. Rubio, 2018, Phys. Rev. Lett. 121, 097402.

Tang, T., H. Wang, S. Duan, Y. Yang, C. Huang, Y. Guo, D. Qian, and W. Zhang, 2020, Phys. Rev. B 101, 235148.

Tanimura, H., J. Kanasaki, and K. Tanimura, 2015, Phys. Rev. B 91, 045201.

Tanimura, H., J. Kanasaki, K. Tanimura, J. Sjakste, N. Vast, M. Calandra, and F. Mauri, 2016, Phys. Rev. B 93, 161203.

Tanimura, H., K. Tanimura, and J. Kanasaki, 2021, Phys. Rev. B 104, 245201.

Tanimura, H., K. Tanimura, and P. Van Loosdrecht, 2019, Phys. Rev. B 100, 115204.

Tao, J., and J.-X. Zhu, 2010, Phys. Rev. B 81, 224506.

Tengdin, P., et al., 2018, Sci. Adv. 4, eaap9744.

Tielrooij, K., J. Song, S. A. Jensen, A. Centeno, A. Pesquera, A. Z. Elorza, M. Bonn, L. Levitov, and F. Koppens, 2013, Nat. Phys. 9, 248.

Topp, G. E., C. J. Eckhardt, D. M. Kennes, M. A. Sentef, and P. Törmä, 2021, Phys. Rev. B 104, 064306.

Topp, G. E., G. Jotzu, J. W. McIver, L. Xian, A. Rubio, and M. A. Sentef, 2019, Phys. Rev. Res. 1, 023031.

Tusche, C., A. Krasyuk, and J. Kirschner, 2015, Ultramicroscopy 159, 520.

Tusche, C., et al., 2016, Appl. Phys. Lett. 108, 261602.

Ulstrup, S., J. C. Johannsen, M. Grioni, and P. Hofmann, 2014, Rev. Sci. Instrum. 85, 013907.

Ulstrup, S., et al., 2014, Phys. Rev. Lett. 112, 257401.

Ulstrup, S., et al., 2015a, J. Electron Spectrosc. Relat. Phenom. 200, 340.

Ulstrup, S., et al., 2015b, J. Phys. Condens. Matter 27, 164206.

Ulstrup, S., et al., 2016, ACS Nano 10, 6315.

Ulstrup, S., et al., 2017, Phys. Rev. B 95, 041405.

Valla, T., A. Fedorov, P. Johnson, and S. Hulbert, 1999, Phys. Rev. Lett. 83, 2085.

Volckaert, K., B. K. Choi, H. J. Kim, D. Biswas, D. Puntel, S. Peli, F. Parmigiani, F. Cilento, Y. J. Chang, and S. Ulstrup, 2023, Phys. Rev. Mater. 7, L041001.

Volckaert, K., et al., 2019, Phys. Rev. B 100, 241406.

Wakisaka, Y., et al., 2012, J. Supercond. Novel Magn. 25, 1231.

Wallauer, R., P. Marauhn, J. Reimann, S. Zoerb, F. Kraus, J. Güdde, M. Rohlfing, and U. Höfer, 2020, Phys. Rev. B 102, 125417.

Wallauer, R., J. Reimann, N. Armbrust, J. Güdde, and U. Höfer, 2016, Appl. Phys. Lett. 109, 162102.

Wallauer, R., et al., 2021, Nano Lett. 21, 5867.

Wandel, S., et al., 2022, Science 376, 860.

Wang, G., A. Chernikov, M. M. Glazov, T. F. Heinz, X. Marie, T. Amand, and B. Urbaszek, 2018, Rev. Mod. Phys. 90, 021001.

Wang, Y., and N. Gedik, 2013, Phys. Status Solidi RRL 7, 64.

Wang, Y., D. Hsieh, E. Sie, H. Steinberg, D. Gardner, Y. Lee, P. Jarillo-Herrero, and N. Gedik, 2012, Phys. Rev. Lett. 109, 127401.

Wang, Y., H. Steinberg, P. Jarillo-Herrero, and N. Gedik, 2013, Science 342, 453.

Wang, Y., W. Yao, Z. Xin, T. Han, Z. Wang, L. Chen, C. Cai, Y. Li, and Y. Zhang, 2020, Nat. Commun. 11, 4215.

Weber, A., F. Pressacco, S. Guenther, E. Mancini, P. M. Oppeneer, and C. Back, 2011, Phys. Rev. B 84, 132412.

Wegkamp, D., and J. Stähler, 2015, Prog. Surf. Sci. 90, 464.

Wegkamp, D., et al., 2014, Phys. Rev. Lett. 113, 216401.

Weinelt, M., M. Kutschera, T. Fauster, and M. Rohlfing, 2004, Phys. Rev. Lett. 92, 126801.

Weinelt, M., M. Kutschera, R. Schmidt, C. Orth, T. Fauster, and M. Rohlfing, 2005, Appl. Phys. A 80, 995.

Werdehausen, D., T. Takayama, M. Höppner, G. Albrecht, A. W. Rost, Y. Lu, D. Manske, H. Takagi, and S. Kaiser, 2018, Sci. Adv. 4, eaap8652.

Widdra, W., et al., 2003, Surf. Sci. 543, 87.

Xian, R. P., et al., 2020, Sci. Data 7, 442.

Xu, T., T. Morimoto, A. Lanzara, and J. E. Moore, 2019, Phys. Rev. B 99, 035117.

Xu, T., et al., 2019, Phys. Rev. B 99, 094308.

Yan, B., and C. Felser, 2017, Annu. Rev. Condens. Matter Phys. 8, 337.

Yang, J.-A., S. Parham, D. Dessau, and D. Reznik, 2017, Sci. Rep. 7, 40876.

Yang, L., G. Rohde, Y. Chen, W. Shi, Z. Liu, F. Chen, Y. Chen, K. Rossnagel, and M. Bauer, 2021, J. Electron Spectrosc. Relat. Phenom. 250, 147085.

Yang, L., et al., 2014, Phys. Rev. Lett. 112, 207001.

Yang, S.-L., J. Sobota, Y. He, D. Leuenberger, H. Soifer, H. Eisaki, P. Kirchmann, and Z.-X. Shen, 2019, Phys. Rev. Lett. 122, 176403.

Yang, S.-L., J. A. Sobota, P. S. Kirchmann, and Z.-X. Shen, 2014, Appl. Phys. A 116, 85.

Yang, S.-L., J. A. Sobota, D. Leuenberger, Y. He, M. Hashimoto, D. Lu, H. Eisaki, P. S. Kirchmann, and Z.-X. Shen, 2015, Phys. Rev. Lett. 114, 247001.

Yang, S.-L., et al., 2017, Phys. Rev. B 96, 245112.

Yang, Y., T. Tang, S. Duan, C. Zhou, D. Hao, and W. Zhang, 2019, Rev. Sci. Instrum. 90, 063905.

Yang, Y., et al., 2022, Phys. Rev. Lett. 128, 246401.

Yoshikawa, T., Y. Ishida, K. Sumida, J. Chen, K. A. Kokh, O. E. Tereshchenko, S. Shin, and A. Kimura, 2018, Appl. Phys. Lett. 112, 192104.

Yoshikawa, T., et al., 2019, Phys. Rev. B 100, 165311.

You, W., et al., 2018, Phys. Rev. Lett. 121, 077204.

Zeiger, H., J. Vidal, T. Cheng, E. Ippen, G. Dresselhaus, and M. Dresselhaus, 1992, Phys. Rev. B 45, 768.

Zeng, H., J. Dai, W. Yao, D. Xiao, and X. Cui, 2012, Nat. Nanotechnol. **7**, 490.

Zhang, H., C. Bao, M. Schüler, S. Zhou, Q. Li, L. Luo, W. Yao, Z. Wang, T. P. Devereaux, and S. Zhou, 2022, Natl. Sci. Rev. **9**, nwab175.

Zhang, H., T. Pincelli, C. Jozwiak, T. Kondo, R. Ernstorfer, T. Sato, and S. Zhou, 2022, Nat. Rev. Methods Primers **2**, 54.

Zhang, J., J. Caillaux, Z. Chen, M. Konczykowski, A. Hruban, A. Wołoś, A. Materna, L. Perfetti, E. Papalazarou, and M. Marsi, 2021, J. Electron Spectrosc. Relat. Phenom. **253**, 147125.

Zhang, J., Z. Chen, J. Caillaux, Y. Klein, A. Gauzzi, A. Bendounan, A. Taleb-Ibrahimi, L. Perfetti, E. Papalazarou, and M. Marsi, 2023, Eur. Phys. J. Special Topics **232**, 2205.

Zhang, W., T. Miller, C. L. Smallwood, Y. Yoshida, H. Eisaki, R. Kaindl, D.-H. Lee, and A. Lanzara, 2016, Sci. Rep. **6**, 29100.

Zhang, W., C. L. Smallwood, C. Jozwiak, T. L. Miller, Y. Yoshida, H. Eisaki, D.-H. Lee, and A. Lanzara, 2013, Phys. Rev. B **88**, 245132.

Zhang, W., et al., 2014, Nat. Commun. **5**, 4959.

Zhang, X., Q. Liu, J.-W. Luo, A. J. Freeman, and A. Zunger, 2014, Nat. Phys. **10**, 387.

Zhang, Y., et al., 2022, Struct. Dyn. **9**, 014501.

Zhang, Z., C. Piovera, E. Papalazarou, M. Marsi, M. d'Astuto, C. van der Beek, A. Taleb-Ibrahimi, and L. Perfetti, 2017, Phys. Rev. B **96**, 064510.

Zhong, H., C. Bao, H. Wang, J. Li, Z. Yin, Y. Xu, W. Duan, T.-L. Xia, and S. Zhou, 2021, Nano Lett. **21**, 6080.

Zhou, S., et al., 2023, Nature (London) **614**, 75.

Zhou, Y., and M.-W. Wu, 2011, Phys. Rev. B **83**, 245436.

Zhu, J., C. Lee, F. Mahmood, T. Suzuki, S. Fang, N. Gedik, and J. G. Checkelsky, 2022, Phys. Rev. B **106**, 115105.

Zhu, S., et al., 2015, Sci. Rep. **5**, 13213.

Zhu, X., Y. Cao, J. Zhang, E. Plummer, and J. Guo, 2015, Proc. Natl. Acad. Sci. U.S.A. **112**, 2367.

Zhu, Z.-H., C. Veenstra, G. Levy, A. Ubaldini, P. Syers, N. Butch, J. Paglione, M. Haverkort, I. Elfimov, and A. Damascelli, 2013, Phys. Rev. Lett. **110**, 216401.

Zong, A., 2021, *Emergent States in Photoinduced Charge-Density-Wave Transitions* (Springer International Publishing, Cham, Switzerland), pp. 1–36.

Zong, A., et al., 2019a, Phys. Rev. Lett. **123**, 097601.

Zong, A., et al., 2019b, Nat. Phys. **15**, 27.

Zonno, M., F. Boschini, and A. Damascelli, 2021, J. Electron Spectrosc. Relat. Phenom. **251**, 147091.

Zonno, M., et al., 2021, Phys. Rev. B **103**, 155109.